THEORETICAL INVESTIGATIONS OF INELASTIC PROCESSES IN SLOW TO FAST ION-ATOM COLLISIONS

by

TECK GHEE LEE

B.S., Queen's University Of Belfast, UK, 1994
M.S., University of Malaya, Malaysia, 1996

A DISSERTATION
submitted in partial fulfillment of the
requirements for the degree
DOCTOR OF PHILOSOPHY

Department of Physics
College of Arts and Sciences
KANSAS STATE UNIVERSITY
Manhattan, Kansas

2003

Approved By:

Major Professor
Chii-Dong Lin

ABSTRACT

Within the close-coupling formalism, we have studied the inelastic processes of a variety of ion-atom collision systems in a wide range of impact energies. Semiclassical approximation has been used for intermediate- to high-energy collisions. As for the low-energy collisions, quantum mechanical approach is applied.

We have performed an extensive semiclassical two-electron two-center atomic orbital close-coupling (TCAOCC2e) calculation to study the single ionization cross sections in $\bar{p}$ + He($1s^2$) collisions. The stabilities of the ionization probability and cross sections are examined with respect to the choice of the basis sets. Below 40 keV, our cross sections are slightly higher than the Force Impulse Method. They disagree with the existing experimental data, and therefore we conclude that a new measurement is needed.

A combination of the Eikonal approximation and a one-electron TCAOCC was utilized to study the state-selective differential charge transfer cross sections for Na^+ + Rb(5s,5p) at E = 2, 5 and 7 keV. The theoretical results are in good agreement when compared to the recent measurements obtained with Rb targets cooled in a magnetic optical trap (MOTRIMS). Despite the fine resolution offered by MOTRIMS, the experimental angular differential cross sections do not exhibit the oscillatory structure shown in the theory.

Using the Hyperspherical method, we searched for bound rotational states of helium trimer by solving the Schrödinger equation in the adiabatic representation. From the resulting repulsive potential curves for non-zero angular momenta, we showed that there are no bound rotational states in any of the isotopes of the He trimer.

A conjoint technique of Hyperspherical Coordinate, Smooth Variable Discretization (SVD) and $\mathcal{R}$-matrix propagation methods was used to study the slow 20 eV – 2 keV H^+ + D(1s) collisions. This quantum mechanical approach is free from ambiguities associated with the conventional Born-Oppenheimer (BO) method. We showed that the cross sections for excitation and charge transfer to 2p states are essentially identical over the whole energy range and stay relatively independent of energy from 2 keV down to 150 eV. Below 150 keV, the cross sections decrease precipitously with decreasing energy. The rapid drop of cross sections was explained with the aid of hyperspherical potential curves.

Publication List

1. B.B. Dhal, Lokesh C. Tribedi, U. Tiwari, P.N. Tandon, T. G. Lee, C.D. Lin and L. Guly'as.
   J. Phys. B: At. Mol. Opt. Phys. **33**, 1069-1079 (2000)
   Strong double K-K transfer channel in near symmetric collision of Si^+ + Ar at intermediate velocity range.

2. T. G. Lee, H. C. Tseng and C. D. Lin.
   Phys. Rev. A **61**, 062713 (2000).
   Evaluation of antiproton impact ionization of He atoms below 40 keV.

3. B.B. Dhal, Lokesh C. Tribedi, U. Tiwari, P.N. Tandon, T. G. Lee, C.D. Lin and L. Guly'as.
   Phys. Rev. A **62**, 022714 (2000)
   Single K-K electron transfer and K-ionization cross sections in collisions of highly charged C,O,F,S,Cl ions with Ar and Kr.

4. T. G. Lee, B. D. Esry, B. Gou and C. D. Lin.
   J. Phys. B: At. Mol. Opt. Phys. **34**, L203 (2001)
   Helium trimer has no bound rotational excited states.

5. T. G. Lee, H. Nguyen, X. Flechard, B. D. DePaola and C. D. Lin.
   Phys. Rev. A **62**, 042701 (2002)
   Differential charge-transfer cross sections for Na^+ with Rb collisions at low energies.

6. M. Zamkov, E. P. Benis, P. Richard, T. G. Lee and T. J. M. Zouros.
   Phys. Rev. A **62**, 042714 (2002)
   Triple Electron Capture in fast 0.5-1 Mev/u C^{6+} on Ar collisions.

7. T.G. Lee, H.C. Tseng and C.D. Lin.
   (unpublished) (2002)
   Transfer ionization and single capture in 0.5-2.5 MeV/u $F^{8+/9+}$ + He($1s^2$) collisions.

8. T. J. M. Zouros, E. P. Benis, A. D. Gonzalez, T. G. Lee, P. Richard and T. W. Gorczyca.
   Proceedings of the Application of Accelerators in Research and Industry, Nov 12-16 (2002), Denton, TX, USA.
   Resonant (RTE) and Non Resonant (NTE) Transfer Excitation in 4MeV B4+ collisions with H_2, He and Ar studied by zero-degree Auger projectile electron spectroscopy

9. M. Zamkov, E. P. Benis, P. Richard, T. G. Lee and T. J. M. Zouros.
   Nuclear Inst. and Methods in Physics Research, B. **205**, 522 (2003)
   Absolute measurements and calculation of triple electron capture cross sections in fast 0.5-1.1 MeV/u C^{6+} on Ar collisions.

10. M. Zamkov, E. P. Benis, C. D. Lin, T. G. Lee, T. Morishita, P. Richard and T. J. M. Zouros.
    Phys. Rev. A **67**, 050703(R) (2003)
    Experimental observation and theoretical calculations of triply excited $2s2p^2\ {}^2S^e$ ${}^{2,4}P^e$, ${}^2D^e$, and $2p^3\ {}^2P^o$,${}^2D^o$ states of fluorine.

11. Anh-Thu Le, M. Hesse, T. G. Lee and C.D. Lin.
    J. Phys. B: At. Mol. Opt. Phys. **36**, 3281 (2003)
    Hyperspherical close coupling calculations for charge transfer cross sections in Si^{4+}+H(D) and Be^{4+}+H collisions at low energies.

12. T.G. Lee, Ann-Thu Le and C.D. Lin.
    J. Phys. B: At. Mol. Opt. Phys. (accepted)
    Charge transfer and excitation in slow 20 eV – 2 keV H^++D(1s) collisions.

Contents

Publication List 4

Table of Contents i

List of Figures iv

List of Tables vi

Acknowledgments vii

1 Introduction **1**

1.1 General Motivation 1

1.2 Basic Features of Ion-Atom Collisions 4

1.3 Theoretical Problems in the Low Energy Region 7

2 Semi-Classical Representation **11**

2.1 Coordinate Frames and Schrödinger Equation 12

2.2 Impact-Parameter Close-Coupling Model 14

2.2.1 Choice of Basis Sets 18

2.2.2 Close-Coupling Equation and Matrix Elements 18

2.2.3 Cross Sections 20

3 Quantum-Mechanical Representation **23**

3.1 Jacobi and Hyperspherical Coordinates 23

3.2 Hyperradial Form of Schrödinger Equation 26
3.3 Adiabatic Hyperspherical Approximation 28
3.4 Channel Function and Matrix Elements 29
3.4.1 Channel Function in Space-Fixed Frame (SF) 29
3.4.2 Channel Function in Body-Fixed Frame (BF) 30
3.4.3 Coupling Matrix Elements in Body-Fixed Frame 32
3.5 Solution of Coupled Hyperradial Equations 34
3.5.1 The Slow/Smooth Variable Discretization (SVD) Method and $\mathcal{R}$-matrix Propagation 35
3.5.2 Matching Scheme and Cross Section 38
3.5.3 Numerical Procedures 41

4 Applications to Ion-Atom Collisions 46
4.1 Part I: Semi-Classical Approach 47
4.2 Part I: Semi-Classical Approach 54
4.3 Part II: Quantum Mechanical Approach 63
4.4 Part II: Quantum Mechanical Approach 72

5 Summary and Concluding Remarks 85

A Independent Electron Model 87

B DVR Basis and Matrices 89

C TCAOCC Program 91
C.1 Explanation of variables 92
C.2 Input 94
C.3 Output 96

C.4 Differential cross section (dcs.f) and input parameters 97

D HSCC Program **99**

D.1 Code-names and explanation of input variables 99

List of Figures

2.1 Schematic diagram of the relative coordinates for collision system A + (B+e) 13

3.1 Definition of 3 sets of Jacobi coordinates 24

3.2 Body-fixed frame. The three particles lie on the x'-z' plane with the z'-axis along the line connecting particles A and B 31

3.3 Locations of singularities in $\phi - \theta$ plane. 41

4.1 Paper I

1. Single ionization cross sections for antiproton collisions with He 48
2. $bP(b)$ vs b for ionization of $\bar{p}$-He collisions at 20 keV 50
3. Same as Fig 2. but for E = 50 and 4 keV, respectively 51
4. Total ionization cross sections for $\bar{p}$-H 52
5. Excitation cross sections to 1s2s ($^1S^e$) and 1s2p ($^1P^o$) states for $\bar{p}$-He 52

4.2 Paper II

1. Simplified schematic diagram of experimental setup 55
2. Relative capture cross section vs Q-value for collision energy of 7keV 56
3. Energy level diagram of ^{87}Rb and ^{23}Na atoms 59
4. Adiabatic potential curves for RbNa$^+$ 59

5. sinθ $\times$ DCS vs scattering angle θ for Rb(5s)-Na(3s,3p) from 7 to 2 keV 59

6. sinθ $\times$ DCS vs $\theta \times E$ for Rb(5s)-Na(3p) from 7 to 2 keV 60

7. sinθ $\times$ DCS vs θ and $bP(b)$ vs b for Rb(5s)-Na($3p_{0,\pm1}$) from 7 to 2 keV 60

8. Same as Fig. 5 but for Rb(5p)-Na(4s) and Rb(5p)-Na(4s), respectively 61

9. Same as Fig. 6 but for Rb(5p)-Na(3p) 61

4.3 Paper III

1. Lowest adiabatic hyperspherical potential curves for $^4He_3$ for J^π symmetry 66

2. Lowest adiabatic hyperspherical potential curves for $^4He_2{}^3He$ for J^π symmetry . . . 67

3. Hyperspherical potential curves for $^4He_3$ without permutational symmetry 68

4. Contour plots of different rotational-component of channel functions 69

4.4 Paper IV

1. Adiabatic hyperspherical potential curves for HD^+ 80

2. Comparison of HSCC calculations with experimental and semiclassical results . . . 81

3. Adiabatic hyperspherical potential curves for $2p_\sigma$ and $2p_\pi$ 82

4. Same as Fig. 2 but for electron capture to H(1s) 82

5. $bP(b)$ vs b for capture H(2p) and excitation D(2p) from E = 0.05 to 1 keV . . . 83

6. Electron capture probabilities as a function of b for E = 0.05 and 1 keV 83

List of Tables

4.1 Paper I

1. Comparison of the two sets of eigenenergies (a.u.) of He singlet states 49

2. Comparison of calculated ionization probabilities from two different sets of basis . 50

4.2 Paper II

1. Calculated bound-states energies of Na in comparison with experimental data . . . 57

2. Calculated bound-states energies of Rb in comparison with experimental data . . . 57

3. Integral charge transfer cross sections from ground state Rb(5s) to final states . . . 58

4. Integral charge transfer cross sections from ground state Rb(5p) to final states . . . 60

4.3 Paper III

1. Weights of the I components of $^4He_3$ 70

ACKNOWLEDGMENTS

I would like to express my sincere gratitude to my major advisor, Professor Chii-Dong Lin, for this continual and careful guidance, advice and help throughout the course of this study at Kansas State University. I would also like to thank Brett Esry, Toru Morishita, Emil Sidky, H.C. Tseng, Xio Ming Tong, C.N. Liu, Ann-Thu Le, Michel Hesse and Zeng Xiu Zhao for their helpful discussions and useful suggestions. Further grateful acknowledgments are due to the *J.R. Macdonald Laboratory* experimental groups of Professor Pat Richard, Professor Lew Cocke and Professor Brett DePaola.

I wish to thank my thesis committee members: Professor Pat Richard, Professor Lew Cocke, Professor Brett DePaola and Professor Robert Burckel for reviewing this dissertation.

Last but not the least, I am definitely indebted to my beloved wife, Pek-Yee, for her unconditional love, encouragement and taking over most of the house keeping, which make this work possible. My special thanks also go to my family at home for believing in me, especially my late grandfather, *Mr. Lee Beng Toh*, who constantly supported and encouraged me to pursue my dream.

This work was supported in part by the Chemical Sciences, Geosciences and Biosciences Division, Office of Basic Sciences, Office of Science, U.S. Department of Energy.

Teck Ghee Lee

June 11, 2003
KSU, Manhattan, KS

Chapter 1

Introduction

1.1 General Motivation

The standard Big Bang model has been very successful in describing the abundance of the elements and cosmic background radiation measurements. However, many astrophysicists are still curious about how the galaxies and clusters are formed. Most of the information about the environment of the early Universe comes to us from the radiation emitted from atoms and molecules in the terrestrial inter-stellar media. An understanding of the relevant atomic and molecular processes is therefore required to correctly interpret this radiation. For decades an intense amount of experimental, as well as theoretical activities has been devoted to the collisions between singly and multiply charged ions and atoms. The study of inelastic processes in ion-atom collisions is crucial not only for the understanding of the basic mechanism of the underlying reactions, but also for understanding the dynamic behavior and the physical properties of both astrophysical and controlled-thermonuclear-fusion Tokamak plasma. For instance, in astrophysics, hydrogen-line emissions play a very important role in the interpretation and analysis of proton-aurora; in particular Balmer-α and Balmer-β serve as proton-aurora sensors. Cross sections and rate coefficients for reactions involving excitation and charge transfer of atoms in collisions with ionic or atomic species are required to interpret such observations [1]. On Earth, we have the man-made fusion plasma. The decay of the ionic states formed by electron capture can be used for plasma diagnostics. As an example, the density profiles of the hydrogen formed in the Tokamak plasma can be determined by observing the formation of $Ar^{16+}(1s, nlm)$

via electron capture from atomic hydrogen [2]. Mass production of these data is very impractical experimentally compared to the theoretical studies which are more cost effective. Furthermore, experiments may be difficult to perform at collision energies below 1 keV/amu, and theoretical calculations can provide meaningful guidance to the experimenters' expectations.

For theorists, the understanding of the underlying mechanisms in ion-atom collisions relies on solving either the time-dependent or time-independent Schrödinger equations. In principle, one would like to be able to solve these equations exactly but it is computationally impractical if not impossible since the simplest collision system involves three particles, namely two ions and an electron, where six independent variables are needed to describe the relative motion of the collision system in the center-of-mass frame. Therefore, various theoretical models were developed to mitigate these difficulties. Historically, the theoretical tool box used to study heavy particle atomic collisions was divided into two broad categories: (i) close-coupling (CC) methods based on an expansion of the wave function in terms of a set of atomic or molecular orbital basis functions chosen to describe the electronic coordinates of the colliding atomic systems, and (ii) perturbative methods such as the truncated Born series.

For *high/intermediate*-energy collisions, the electronic motion is much slower than the nuclear motion, thus is treated quantum-mechanically. However, the motion of the two heavy nuclei can be approximated by a straight-line trajectory, which is also known as a semi-classical impact-parameter approximation. As for *low*-energy collisions, both electronic and nuclear motions are treated quantum-mechanically since the straight-line trajectory approximation is no longer valid. In this dissertation, we employed a quantum-mechanical hyperspherical close-coupling approach to treat the low-energy ion-atom collisions. The terms "high" and "low" are quite ambiguous in this context and have often been misunderstood, leaving the boundary of validity vague. This issue will be clarified in the next section. In the semi-classical close-coupling (CC) approximation, we solve the time-dependent Schrödinger equation by expanding the total wave functions in terms of atomic or molecular orbital functions with the appropriate plane-wave electron translational factors (ETF's). On the other hand, in our quantum-mechanical approach, we solve the time-independent Schrödinger equation by using a combination of B-Splines [3, 4], a discrete variable representation (DVR) method [5, 6] and a $\mathcal{R}$-matrix propagation scheme [7]. The accuracy of the close-coupling method is utterly dependent on the choice of the

basis sets used. It has been shown in the course of many decades that the CC method is quite successful in predicting the cross sections and other physical quantities for dominant inelastic processes in ion-atom collisions.

The application of the large-scale close-coupling calculation has become a routine practice to the theoretical atomic and molecular physics community because of the availability of the desktop supercomputers. On the other hand, owing to the modern accelerators, ion sources, ion-traps, and advanced electronics, a high-level of sophistication in the current measurements of inelastic processes has been made possible [8]. Specifically, it is possible to experimentally observe the final electronic state with specific quantum states nlm designation resulting from electron capture or excitation in an ion-atom collision using methods such as energy gain and energy loss spectroscopy and photon emission spectroscopy. Moreover, a so-called "complete experiment" can be performed with the possibility to obtain the differential information in low-energy ion-atom collisions using coincident measurement [9] with a combination of cooling and trapping techniques such as Cold-target Recoil Ion Momentum Spectroscopy (COLTRIMS) and Magneto Optically Trapped-target Recoil Ion Momentum Spectroscopy (MOTRIMS). For many years, the theoretical and experimental advances have kept pace with one another, enabling close interactions that allowed the theorists and experimenters to obtain good insight into the underlying dynamics in ion-atom collisions. Although the agreement between the theoretical and experimental results has improved, there are still questions that remain to be answered and the physical mechanisms needs to be explained; particularly as measurement techniques become more refined and sophisticated, and consequently the experimental features are more precise and more challenging to a theoretical description.

The scope of this dissertation is to understand the dynamics of the electron transition processes by means of the "quantitatively reliable" close-coupling treatment in slow-to-fast ion-atom collisions. The theoretical results are usually compared with the best experimental data available to date. This dissertation is organized as follows. In the remaining sections of this chapter, we provide a brief description of the basic features of ion-atom collisions and an outline of theoretical problems in the low-energy region. Chapters 2 and 3 describe the underlying semiclassical and quantum theories of the present work, respectively. The application of these methods is given in Chapter 4 based on a number of publications; it is divided into two categories: semi-classical and quantum-mechanical methods. Finally, a summary and concluding remarks are given in Chapter 5. References

are provided at the end of each chapter and publication.

1.2 Basic Features of Ion-Atom Collisions

The contexts of "high" and "low" in ion-atom collision depend critically on the impact velocity v_o of the incident ion relative to the velocity v_e of the valence electron during the collision. The ratio of the projectile velocity, v_o, to that of the orbital electron of interest in the target, v_e, provides some guidance in categorizing low- and high-energy collisions. In high-energy ($v_o/v_e \geq 2$) heavy particle collisions, ionization generally is the dominant channel, followed by target excitation processes. However, in low- to intermediate-energy heavy particle collisions, it is not possible to single out a dominant channel in general, because often many inelastic channels strongly couple with one another. A reasonable theoretical description of the collision system, in principle, needs to account for all of the important channels of comparable magnitudes in probabilities. Without the simultaneous inclusion of all these channels, the accurate determination of transition probabilities is impossible. This is where a non-perturbative scheme like the close-coupling method is indispensable.

At low collision energies ($v_o/v_e \leq 1$), charge transfer is the dominant process. A general characteristic of charge transfer, which partially arises from the sensitivity of the magnitude of the cross section to the energy defect ΔE between the initial and final states of the collision system, is that many reactions lead selectively to one, or to a small number, of final states. This effect is known as *state-selective* charge transfer. Take the case of $He^{2+} + H(1s) \rightarrow He^{+}(nl) + H^{+}$ as an example. At low energies ($E_L \leq 15$ keV/amu) the dominant process is that leading to the n=2 level of He^{+}. This is a *resonant reaction* since the ΔE=0. On the other hand, if the impact energy increases, the final $He^{+}(nl)$ states with $n \neq 2$ gradually become relatively more important and the reaction becomes less state-selective. In general, the energy-dependent charge transfer cross section has a peak near the matching velocity ($v_o = v_e$) because of the large overlap of the electron cloud between the projectile and target. Furthermore, in this energy domain charge transfer primarily takes place at large impact parameters. However, as the collision energies depart from the matching velocity region, a close collision becomes increasingly important in the inelastic collision.

The state selectivity of a collision system can also be explained in terms of a transient molecular picture. For low-energy ion-atom collisions, the relative motion of the two heavy ions is very slow compared to the electronic motion and hence the electron is able to adiabatically adjust its motion to the slow varying field of the projectile ion. In this case, one solves the time-dependent close-coupling equations in terms of a set of basis functions constructed from adiabatic molecular orbitals (MO). In this adiabatic approximation the quasi-molecule formed by the electron moving in the field of two nuclei is described by a set of adiabatic potential energy curves. The avoided crossings appearing in the potential curves are used as a guide to understand the dynamics of the electron in the collision system. Electronic transitions leading to capture, excitation and ionization all depend on the local breakdown of the adiabatic approximation. Although the MO method has for decades had many successes in predicting the cross sections of inelastic processes, the method itself has problems [10, 11] which will be discussed in the next section.

The MO expansion method is most suitable for the low-energy ion-atom collisions, while atomic orbitals (AO) expansion on each colliding center tends to be more appropriate for describing the intermediate-energy collisions, since the adiabatic condition no longer holds. The two-center atomic orbital close-coupling (TCAOCC) method can also be used in the *low-energy* ($1 \sim 10$ keV/amu) region, under the condition that the united orbital suggested by the correlation diagram of the collision system be included in the expansion. Pseudo-states can be included in the TCAOCC method to simulate a molecular-like orbital at united-atom limit and represent the continuum states at large internuclear separation. At higher energies where the ionization process dominates over the charge exchange and excitation processes, pseudo-continuum states become relatively important. They were included in both of the projectile- and target-center in the traditional TCAOCC method, leading to an obvious division of "capture to continuum" and "direct ionization" processes.

For intermediate-velocity collisions, the flux entering the charge transfer channel is small; excitation and ionization are the dominant processes. In 1990, Ermoleav [12] demonstrated that it is reasonable to use an asymmetric TCAOCC by assuming the trial wave function can be approximated by a large set of basis functions on the target-center and a smaller set on the projectile-center. A modification of this method known as "one and a half centered expansion (OHCE)" was introduced by Reading *et al* [13]. It turns out that the asymmetric TCAOCC is much more stable numerically in the evaluation of the excitation and ionization cross sections [14] than the symmetric one, in which both projectile

and target centers pseudo-states are used in the expansion. The asymmetric TCAOCC can also be applied at low energies, if a large set of basis functions is used in the projectile-center and a small set in the target-center [14] within the two-center expansion method. At higher impact energies, a truncated single-center expansion (SCE) is often used. The advantages of SCE are: (i) the interaction matrix elements depend only on the internuclear separation and have only to be computed once, independently of incident velocity, (ii) the matrix elements are Hermitian and hence the coupled differential equations can be solved efficiently with an approximation method, and (iii) the evaluation of cross sections is variational in the sense that the accuracy can be uniformly improved by increasing the number of basis functions. Although, an untruncated single-center expansion is formally "complete", it is difficult to represent charge exchange channels in terms of any finite number of target basis functions. Nevertheless, electron-excitation and electron-removal cross sections can be calculated accurately with a sufficiently large number of bound and pseudo-states on the target.

The two-center atomic-orbital expansion close-coupling method was initiated by Bates and McCarroll [15] in 1958. Since then the method has been extensively studied and used in slow to fast ion-atom collisions and the successes of this method for describing the inelastic processes are recorded in the monograph by Bransden and McDowell [16]. With the advent of faster computers, larger and larger basis sets have been employed in order to achieve converged cross sections. Since an untruncated single-center expansion is formally "complete", a simultaneous inclusion of two sufficiently large basis sets on both centers in the TCAOCC method can gradually become "over-complete" particularly for small internuclear separations, leading to pronounced spurious oscillatory structures in calculated excitation cross sections [17, 18, 19]. Furthermore, the over-completeness of the TCAOCC method can overestimate the magnitude of the ionization cross sections. Through a series of careful studies, Kuang and Lin [14] have demonstrated that reliable cross sections can be achieved by using the asymmetric TCAOCC method with a large number of basis states on the target and limited number of bound states on the projectile.

However, it is not unusual to observe oscillatory structures in integrated cross sections of ion-atom collision especially at low-energy region where an electron can hop back and forth between the target and projectile centers. Most importantly, the oscillatory structures in the cross sections are independent of the choice of basis sets included in the calculation. For collisions at intermediate-energy or high-energy, the interaction time

between the two colliding heavy nuclei is short, and the electron has no time to move between the target and the projectile. Therefore, charge transfer and excitation cross sections are expected to vary smoothly with respect to the collision energies. Since oscillations are not possible in the high-energy collisions, the resulting oscillations are artifacts of the simultaneous inclusion of pseudo-states and will depend on the choice of basis sets.

1.3 Theoretical Problems in the Low Energy Region

In slow ($v_o/v_e \ll 1$) ion-atom collisions, both electron and nuclear motions are normally treated quantum-mechanically. As mentioned earlier, the molecular orbital expansion method also known as adiabatic Born-Oppenheimer or Perturbed Stationary State (BO/PSS) approximation is more suitable for describing the low energy ion-atom collision. However, this method possesses severe intrinsic problems in that: (i) the system scattering wave function expanded in terms of adiabatic molecular orbitals does not satisfy the correct asymptotic boundary condition, which specifies that in the separated-atom limit the bound electron is moving either with the projectile or with the target, (ii) the non-adiabatic coupling matrix possesses non-zero value at infinite internuclear separation, and (iii) the calculated cross sections are not Galilean invariant.

The translational motion of electron was not accounted for in the conventional PSS model originally proposed by Massey and Smith in 1933. Later, the importance of electron translational factors (ETF's) was first recognized by Bates and McCarroll [15] in 1958, in order to meet the asymptotic boundary conditions in the reaction channels represented by the basis functions. The ETF's were first introduced into the semiclassical treatment of ion-atom collisions at high energies where internuclear motion is treated classically. In the semiclassical model, within the separated atom limit, each molecular orbital is reduced to a well defined atomic orbital which is moving with each atomic center with a definite velocity, and plane wave translational factors can be associated with each of these orbitals. The choice of ETF's for molecular orbitals at finite internuclear separation is however not well defined. Nevertheless, various forms of ETF's have been proposed and applied in the past decades for the actual PSS calculations (MO-ETF's models) at the very least they impose the correct asymptotic behavior for the wave functions and restore the Galilean invariance of the calculated cross sections. Failure to include the proper ETF's in the

basis function leads to the corresponding coupled differential equations being not Galilean invariant, and spurious asymptotic couplings resulting in inaccurate cross sections. The controversy of how to choose the proper ETF's remains as an issue. Although problems associated with the PSS model are well known, the remedies are limited. Methods based on the so-called reaction coordinates [20] were proposed to overcome these problems in the actual calculations; however, these methods are rather complicated to use. The hyperspherical close-coupling method, is therefore developed and implemented to surmount these deficiencies in slow ion-atom collisions.

Bibliography

[1] S. Lepp, P.C. Stancil and A. Dalgarno, J. Phys. B. (*TopicalReview*) **35**, R57 (2002).

[2] J.E. Rice, E.S. Marmar, J.L. Terry, E. Källne and J. Källne, Phys. Rev. Lett. **56**, 50 (1982).

[3] C. de Boor, *A Practical Guide to Splines* (Springer, New York, 1978).

[4] J. Sapirstein and W.R. Johnson, J. Phys. B. (*TopicalReview*) **29**, 5213 (1996).

[5] O.I. Tolstikhin, S. Watanabe and M. Matsuzawa, J. Phys. B **29**, L389 (1996).

[6] J.C. Light and R.B. Walker, J. Chem. Phys. **65**, 4272 (1978)

[7] K.L. Baluja, P.G. Burke and L.A. Morgan, Comput. Phys. Commun. **27**, 299 (1982)

[8] C.L. Cocke, *Review of fundamental processes and applications of Atoms and Ions*, edited by C.D. Lin (**Singapore: World Scientific**), pg 111 (1993).

[9] J. Ullrich, R. Moshammer, R. Dörner, O. Jagutzki, V. Mergel, H. Schmidt-Böcking and L. Spielberger, J. Phys. B **30**, 2917 (1997)

[10] J.B. Delos, Rev. Mod. Phys. **53**, 287 (1981)

[11] M. Kimura and N.F. Lane, *Advances in Atomic, Molecular, and Optical Physics* **26**, 79 (1989)

[12] A.M. Ermoleav, J. Phys. B **23**, L45 (1990)

[13] J.F. Reading, A.L. Ford and R.L Becker, J. Phys. B **14**, 1995 (1981)

[14] Jiyun Kuang and C.D. Lin, J. Phys. B **29**, 1207 (1996)

[15] D.R. Bates and R. McCarroll, Proc. Roy. Soc. Lond. **A245**, 175 (1958)

[16] B.H. Bransden and M.R.C McDowell, *Charge Exchange and the Theory of Ion-Atom Collision*, (Oxford: Claredon) (1992)

[17] R. Shakeshaft, Phys. Rev. A. **18**, 1930 (1978)

[18] W. Fritsch, R. Shingal and C.D. Lin, Phys. Rev. A. **44**, 5686 (1991)

[19] H.A Slim and A.M. Ermoleav, J. Phys. B **27**, L203 (1994)

[20] H. Croft and A.S. Dickinson, J. Phys. B **29**, 57 (1996)

Chapter 2

Semi-Classical Representation

The detailed account of the semiclassical theory of ion-atom collision processes can be found in the monograph by Bransden and McDowell (1992) [1] and the review paper by Fritsch and Lin [2]. In this chapter we shall provide only a short account of the framework of the semiclassical close-coupling theory which is essentially identical to Kuang [3]. To focus our attention on the salient features of the theory, we first consider the simplest collision system of an ion A^{Z+} and atom B with one active electron. Apart from the radiative processes, the end products of the collision may be of the following types:

$$
\begin{aligned}
A^{Z+} + B &\longrightarrow A^{Z+} + B && \text{(elastic)} \\
&\longrightarrow A^{Z+} + B^{*} && \text{(direct excitation)} \\
&\longrightarrow A^{(Z+1)+} + B^{+} && \text{(charge transfer)} \\
&\longrightarrow A^{(Z+1)*} + B^{+} && \text{(transfer excitation)} \\
&\longrightarrow A^{Z+} + B^{+} + e^{-}. && \text{(ionization)}
\end{aligned}
$$

To describe the collision processes of the many electrons system within the one-electron model, the interaction of the active electron with the ions centered on A and B can be approximated by effective model potentials V_A and V_B. A perfect example is the collisions between inert bare ions or alkali ions and alkali atoms, which is characterized by having a single valence electron outside a closed shell of core electrons. For the systems

which involve more than one electron transition, for instance, double electron capture (DC), transfer ionization (TI) and double ionization (DI) processes, the two-electron close-coupling approximation can be used [2]. However, an extensively large basis sets have to be considered on both collision centers in order to account for the continuum states; thus making this approach numerically and computationally challenging and undesirable. For these reasons, many people prefer to treat the multielectron system approximately by using the so-called independent particle model (IPM). This IPM has been quite successful in the application of the collision systems involving an ion and two-electron atoms such as He, H^- and etc. The semi-classical transition probabilities of two electron processes can be carried out through statistical consideration (see Appendix A). However, in principle, it is possible to extend the close-coupling formalism to few-electron systems. Atomic units are used throughout the chapter.

2.1 Coordinate Frames and Schrödinger Equation

Two coordinate frames are usually considered in a scattering calculation. One is the space-fixed frame, in which the direction of the incident ion beam is taken as the Z-axis, the quantization axis. The other one is the body-fixed frame. For the body-fixed frame, the frame of reference is fixed with respect to the internuclear axis of the two heavy nuclei, which is taken to be the quantization axis. In the space-fixed frame formulation, atomic orbital (AO) expansion is usually used. While in the body-fixed frame, the molecular orbital (MO) expansion which is also known as the Born-Oppenheimer approach is employed.

In the laboratory frame, the target atom B is initially at rest while the projectile A is moving in a direction parallel to the incident ion beam Z-axis with an initial velocity of $\mathbf{v}_i$, and the center of mass (CM) of A and B moves with the constant velocity $\mathbf{v}_c = \mathbf{v}_i M_A/(M_A+M_B)$. However, it is more convenient to describe the dynamics of the collision in the center of mass (CM) frame where the CM is at rest. In the CM frame the relative motion of A and B can be considered as an equivalent single-particle with a reduced mass of two heavy nuclei $\mu = M_A M_B/(M_A + M_B)$ moving in an external field $W(\mathbf{R})$. Consider a binary collision between an ion A and an atom B with one active electron, where the

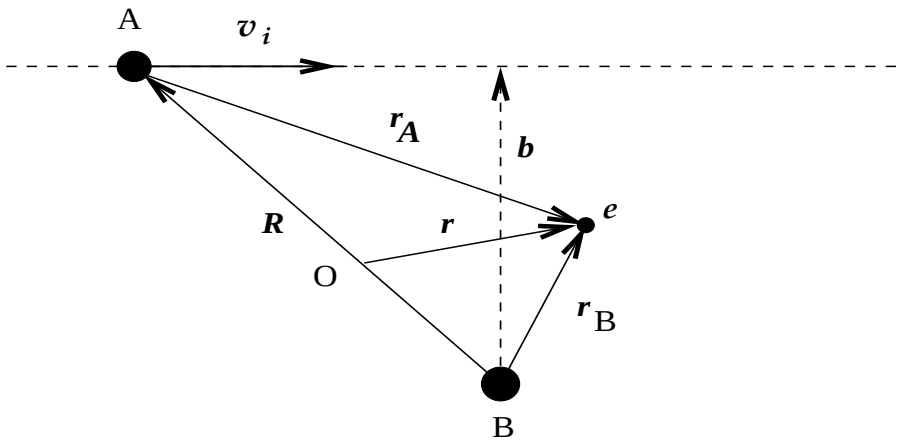

Figure 2.1: Schematic diagram of the relative coordinates for collision system A + (B+e)

origin O is at the CM of projectile A and target B as illustrated in Fig. 2.1. We define two position vectors $(\mathbf{R}, \mathbf{r})$: $\mathbf{R}$ is internuclear separation of A and B, while the relative position vector of electron with respect to O is denoted by $\mathbf{r}$. The relative positions of A and B with respect to O can be written as $-q_A\mathbf{R}$ and $q_B\mathbf{R}$. Thus, the position vectors $(\mathbf{r}_A, \mathbf{r}_B)$ of the electron with respect to A and B can be expressed as $\mathbf{r}_A = \mathbf{r} + q_A\mathbf{R}$ and $\mathbf{r}_A = \mathbf{r} - q_B\mathbf{R}$, where $q_A = \mu/M_A$ and $q_B = 1 - q_A$. The kinetic energy operator is separable and the time-independent Schrödinger equation for the three-body system can be expressed as

$$H\Psi(\mathbf{R}, \mathbf{r}) = (T_{\mathbf{r}} + T_{\mathbf{R}} + V_A + V_B + V_{AB})\Psi(\mathbf{R}, \mathbf{r}) \tag{2.1}$$

$$= E\Psi(\mathbf{R}, \mathbf{r}) \tag{2.2}$$

where E is the total energy of the system in the CM frame. In the $(\mathbf{R}, \mathbf{r})$ coordinate set, the electronic and internuclear kinetic operators can be written as

$$T_{\mathbf{r}} + T_{\mathbf{R}} = -\frac{1}{2m}\nabla^2_{\mathbf{r}} - \frac{1}{2\mu}\nabla^2_{\mathbf{R}} \tag{2.3}$$

where

$$m = \frac{m_e(M_A + M_B)}{m_e + M_A + M_B},\ \mu = \frac{M_A M_B}{M_A + M_B}. \tag{2.4}$$

and $m_e = 1$ a.u., M_A and M_B denote the masses of particles A and B. V_A and V_B represent the interaction between the electron and the ion cores A and B, respectively; while V_{AB} is the interaction between the two cores. For a Coulombic interaction V_A, V_B and V_{AB} are

$$V_A = \frac{-Z_A}{r_A},\ V_B = \frac{-Z_B}{r_B},\ V_{AB} = \frac{Z_A Z_B}{R}. \tag{2.5}$$

For a complex interaction, effective model potentials can be used to represent V_A, V_B and V_{AB}. Specifically, the model potentials used in the present work are in the form of

$$V(r) = \frac{-Z_1}{r} + \frac{(Z_2 + Z_3 r)exp(-Z_4 r)}{r} \tag{2.6}$$

where the parameters Z_i ($i = 1,\ldots, 4$) are determined, so that the energy levels of interest can be well represented by the eigenvalues obtained from diagonalizing the Hamiltonian of an atom A or B .

2.2 Impact-Parameter Close-Coupling Model

In an *energetic* ion-atom collisions ($E_L \geq$ 1keV/amu), the de Broglie wavelength $\lambda = 2\pi/\mu v_o$ associated with the motion of the two heavy nuclei is very small ($\sim 10^{-3}$ a.u.) compared with the size of the interaction region. It is reasonable to assume that the average interaction potential $W(R)$ between the atoms is varying smoothly and only changes slowly over distances of the order of 1 Bohr radius. It follows that if $\lambda < 1$, the relative motion of the nuclei can be well described by a localized wave packet, and the center of which will follow a classical trajectory in the potential $W(R)$. However, the heavy-masses condition is not enough to justify the use of the classic scattering theory. It also requires that the uncertainty $\Delta\theta$ in the scattering angle θ of the nuclei to be small as compared to the scattering angle itself. This is to say $\theta >> 1/L$, where $L = \mu b v$ is the angular

momentum of the relative motion of the nuclei. Once these conditions are fulfilled, the semiclassical scattering theory becomes applicable in ion-atom collisions. The Schrödinger equation (2.2) can then be written as

$$\left(-\frac{1}{2\mu}\nabla^2_{\mathbf{R}} + W(R) + H_e\right)\Psi(\mathbf{R},\mathbf{r}) = E\Psi(\mathbf{R},\mathbf{r}) \tag{2.7}$$

where H_e is the electronic Hamiltonian defined by

$$H_e = -\frac{1}{2}\nabla^2_{\mathbf{r}} + V_A(r_A) + V_B(r_B) + (V_{AB}(R) - W(R)) \tag{2.8}$$

The relative motion of the heavy particles is now described by a wave function $F(\mathbf{R})$ which satisfies the stationary-state Schrödinger equation

$$\left(-\frac{1}{2\mu}\nabla^2_{\mathbf{R}} + W(R)\right)F(\mathbf{R}) = EF(\mathbf{R}) \tag{2.9}$$

Note that $E = E_B + \mu v_o^2/2 \approx \mu v_o^2/2$, where E_B is the electronic binding energy of the atom in the initial state. By setting $F(\mathbf{R}) = exp(iS(\mathbf{R}))$, then eqn. (2.9) becomes

$$-i\nabla^2_{\mathbf{R}}S(\mathbf{R}) + [\nabla_{\mathbf{R}}S(\mathbf{R})]^2 = 2\mu(E - W(R)) \tag{2.10}$$

where

$$S(\mathbf{R}) = \int^R \sqrt{2\mu(E - W(R'))dR'}$$

is the *eikonal* function. Under the semi-classical approximation, $E >> W(R)$; thus $|\nabla_{\mathbf{R}}S(\mathbf{R})|^2 >> |\nabla^2_{\mathbf{R}}S(\mathbf{R})|$. Therefore, the first term in eqn. (2.10) can be neglected. The eikonal function $S(\mathbf{R})$ satisfies the Hamilton-Jacobi equation

$$[\nabla_{\mathbf{R}}S(\mathbf{R})]^2 = 2\mu(E - W(R)) \tag{2.11}$$

which defines all the possible classical trajectories in the potential $W(R)$ with energy E. From this equation, it is obvious that we can define the local classical momentum to be $\mathbf{p} = \nabla_{\mathbf{R}}S(\mathbf{R})$. For a given energy E and a two-dimensional impact parameter $\mathbf{b}$, we define $\mathbf{R}(\mathbf{b},t)$ to be a classical trajectory as a function of time t. For sufficiently high energy scattering, the classical trajectory can be considered as a straight line, $\mathbf{R} = \mathbf{b} + \dot{\mathbf{R}}(t)t$, travelled at a constant velocity $\dot{\mathbf{R}}(t) = \mathbf{v_o}$.

By substituting the wave function describing the relative motion of the electron with respect to the two ions

$$\Psi(\mathbf{R},\mathbf{r}) = F(\mathbf{R})\psi(\mathbf{R},\mathbf{r}) = exp(iS(\mathbf{R}))\psi(\mathbf{R},\mathbf{r}) \tag{2.12}$$

into eqn. (2.7) and making use of eqn. (2.9), we obtain

$$\left(H_e(\mathbf{r},t) - \frac{1}{2\mu}\nabla^2_{\mathbf{R}} - \frac{i}{\mu}\nabla_{\mathbf{R}}S(\mathbf{R})\cdot\nabla_{\mathbf{R}}\right)\psi(\mathbf{R},\mathbf{r}) = 0 \tag{2.13}$$

When the classical trajectory is applicable, the variation of the field $W(R)$ is very small compared to the atomic distance, and hence the $\mathbf{S}(\mathbf{R})$ and ψ will be slowly varying functions of $\mathbf{R}$. It follows that we can neglect the terms involving $\nabla^2_{\mathbf{R}}$ and by setting $\nabla_{\mathbf{R}}S(\mathbf{R}) = \mathbf{p} = \mu\dot{\mathbf{R}}$ eqn. (2.13) reduces to

$$\left(H_e(\mathbf{r},t) - i\dot{\mathbf{R}}\cdot\nabla_{\mathbf{R}}\right)\psi(\mathbf{R}(t),\mathbf{r}) = \left(H_e(\mathbf{r},t) - i\frac{\partial}{\partial t}|_{\mathbf{r}}\right)\psi(\mathbf{r},t) = 0 \tag{2.14}$$

Note that the $\frac{\partial}{\partial t}$ operation is carried by keeping $\mathbf{r}$ fixed in the space-fixed frame. Equation (2.14) is known as the semi-classical impact-parameter time-dependent Schrödinger equation for the electron in a time-dependent potential. The potential terms in H_e depend on $\mathbf{R}$ and $(V_{AB} - W(R))$, and can be removed by a phase-transformation

$$\psi(\mathbf{r},t) = \tilde{\psi}(\mathbf{r},t)exp(-i\int^t [V_{AB}(R') - W(R')dt']) \tag{2.15}$$

where $\mathbf{R}' = \mathbf{R}(\mathbf{b},t')$. Hence, the transition probability $\lim_{t\to\infty}|\langle f|\Psi\rangle|^2$ for populating state $|f\rangle$ is independent of $(V_{AB} - W(R))$. It can be shown that the transition probability is unchanged by this phase-transformation. However, this is not the case for a differential cross section. One cannot ignore this phase contribution from V_{AB} when calculating the differential cross section since the transition amplitude depends on the phase. One can solve the time-dependent equation (2.14) by first ignoring the potential terms and then by transforming the solution back to the original form through the phase-transformation.

Even with the present supercomputers, the time-dependent Schrödinger equation (2.14) involving four variables is still difficult to solve by using direct numerical integration. Therefore, an approximate solution based on the expansion of the time-dependent wave function in terms of appropriate basis functions with correct asymptotic behavior,

$$\psi(\mathbf{r},t) = \sum_i a_i(t)\phi_i^A(\mathbf{r},t) + \sum_j b_j(t)\phi_j^B(\mathbf{r},t) + + \sum_k c_k(t)\phi_k^C(\mathbf{r},t) \tag{2.16}$$

is adopted. Notice that the basis functions have been separated into three sets, namely for the asymptotic elastic+direct excitation $A + (Be)$, charge transfer $(Ae) + B$, as well as ionization channels, $A + B + e$, respectively. Although we do not know how to specify the continuum states of the electron e in the potential fields of the two heavy ions, it is

pivotal to distinguish the set of continuum states $\{\phi_k^C(\mathbf{r},t)\}$ from the two bound states $\{\phi_i^A(\mathbf{r},t)\}$ and $\{\phi_j^B(\mathbf{r},t)\}$ on centers A and B, respectively. With increasing collision energy, the ionization channels become increasingly more important, and continuum states have to be included in the basis. Due to the two-center nature of the continuum states in the ion-atom collision, it is still a very demanding task to construct the continuum wave functions of a diatomic molecule, even in an asymptotic region. It is crucial to have a good representation of the continuum states especially in the intermediate energy region. Here the approximate representation known as *pseudo-continuum* wave functions were employed by diagonalizing the above atomic Hamiltonian. These pseudo states with positive energies have the same form as the bound states. In this way, one can obtain two sets of continuum states. However, as pointed out by Kuang and Lin [4], by simultaneously including two sets of pseudo-continuum states on both centers of two-center atomic orbital close-coupling (TCAOCC) calculations, the resulting energy-dependent cross sections will exhibit an oscillatory structure.

In the typical two-center atomic orbital expansion, the asymptotic forms of the basis functions $\phi_j^A(\mathbf{r},t)$ and $\phi_j^B(\mathbf{r},t)$ centered on both atoms ($X \equiv A, B$) can be written as

$$\phi_j^X(\mathbf{r},t) = \phi_j^X(\mathbf{r}_X) exp[-i\epsilon_j^X t - iq_X \mathbf{v}\cdot\mathbf{r} - i\frac{q_X^2}{2}v^2 t] \tag{2.17}$$

where $\phi_j^A(\mathbf{r}_A)$ and $\phi_j^B(\mathbf{r}_B)$ are their internal wave functions, respectively. The index j denotes the collective set of quantum numbers nlm. Again, we can expand $\phi_j^A(\mathbf{r}_A)$ and $\phi_j^B(\mathbf{r}_B)$ in terms of some primitive basis functions like Slater, Gaussian or even Sturmian functions, which are used to diagonalize the atomic Hamiltonian $H_X = -\frac{1}{2}\nabla^2 + V_X(r_X)$, like

$$\langle \phi_j^X | H_X | \phi_k^X \rangle = \epsilon_j^X \delta_{jk};\ X = A, B \tag{2.18}$$

The velocity-dependent terms in eqn. (2.17) are known as *electronic translational factors* (ETF's) which represent the momentum and kinetic energy of the electron as it rides on nucleus A or B. It was first proposed by Bates and McCarroll [5] in 1958 to satisfy the asymptotic boundary conditions in the reaction channels represented by the basis functions. The consequence of ETF's is to guarantee Galilean invariance under the coordinate transformation of a frame with the origin at O to frames with origins at any places. Failure to include this phase factor in the basis function may provoke a non-vanishing interaction in the separated atom limit, and the resulting cross sections will no longer be Galilean invariant.

2.2.1 Choice of Basis Sets

Before we proceed to the close-coupling equation, we need to carefully choose the type of basis functions that we want to use in the calculation. In the atomic orbital expansion approach, there exist several choices of atomic orbitals [2] which are simple and flexible. It turns out that the specific choice of basis functions that we utilize can govern the efficiency of computing the overlaps and coupling matrices, and how easily a set of linearly independent functions can be generated automatically. It turns out that the most widely used basis functions are the Slater-type (STO) or the Gaussian-type (GTO) orbitals.

In our TCAOCC method [3], the atomic orbitals are expanded in terms of special type of STO known as even-tempered basis functions [6]

$$\phi_{nlm}(\mathbf{r}) = \sum_k C_{nk} N_l(\xi_k) e^{-\xi_k r} \tilde{Y}_{lm}(\mathbf{r}) \tag{2.19}$$

where $\tilde{Y}_{lm}(\mathbf{r})$ consists of a spherical harmonic multiplied by r^l; $N_l(\xi_k)$ is a normalization constant and the orbital exponents ξ_k are taken to form a geometric sequence

$$\xi_k = \alpha\beta^k \qquad (k = 1, 2, \cdots, N) \tag{2.20}$$

Two parameters, α and β, can be determined by energy minimization. The advantages associated with using these basis functions are as following. First, there are only two parameters α and β that need to be adjusted to perform the energy optimization. Second, a large basis set can be easily generated, and eventually a complete set can be achieved in the limit if $\alpha \to 0$, $\beta \to 1$, $\beta^N \to \infty$ as $N \to \infty$. Third, an even-tempered basis set on a single center cannot become linearly dependent with respect to the increasing number of basis functions if $\beta > 1$. Finally, the most important one is the matrix elements required for the TCAOCC method with plane-wave electronic translational factors can be evaluated very efficiently since the evaluation needs only one dimensional integration and the integrand comprises only known elementary functions.

2.2.2 Close-Coupling Equation and Matrix Elements

By inserting the atomic orbital expansion into the time-dependent Schrödinger Equation (2.14), we obtain the close-coupling equation

$$i\mathbf{S}(t)\dot{\mathbf{A}}(t) = \mathbf{G}(t)\mathbf{A}(t), \tag{2.21}$$

where the unknown coefficients $\mathbf{A}(t) = \{a_i(t), b_j(t), c_k(t)\}$ are to be determined. Here $\mathbf{S}(t)$ corresponds to the overlaps between the atomic states, while $\mathbf{G}(t)$ is the interaction matrix containing the coupling between states on the two centers and between states on the same center. Symbolically, they are in the form of

$$S_{jk}(t) = \langle \phi_j | \phi_k \rangle, \; G_{jk}(t) = \langle \phi_j | (H - i\frac{\partial}{\partial t}|_{\mathbf{r}}) | \phi_k \rangle. \tag{2.22}$$

The coupling matrix $\mathbf{G}(t)$ itself is non-Hermitian, but from the relation $\mathbf{G}(t) - \dot{\mathbf{G}}^\dagger(t) = i\dot{\mathbf{S}}$, it follows that the overlap of the wave functions is unitary (i.e., $\langle \psi | \psi \rangle = 1$) at any given time t, must be required. The form of the matrix elements of $\mathbf{S}(t)$ and $\mathbf{G}(t)$ depends on whether they involve eigenstates from the same center or from a different centers. The explicit forms of the matrix elements can be written as follows

$$\begin{aligned}
S_{jk}^{AA} &= S_{jk}^{BB} = \delta_{jk} \\
S_{jk}^{AB} &= e^{i\Delta t} \; \langle \phi_j^A(\mathbf{r}) | e^{i\mathbf{v}\cdot\mathbf{r}} | \phi_k^B(\mathbf{r} - \mathbf{R}) \rangle_{\mathbf{r}} \\
S_{kj}^{BA} &= [S_{jk}^{AB}]^* \\
G_{jk}^{AA} &= e^{i(\epsilon_j^A - \epsilon_k^A)t} \langle \phi_j^{A*}(\mathbf{r}) | V_B(|\mathbf{r} - \mathbf{R}|) | \phi_k^A(\mathbf{r}) \rangle_{\mathbf{r}} \\
G_{jk}^{BB} &= e^{i(\epsilon_j^B - \epsilon_k^B)t} \langle \phi_j^B(\mathbf{r}) | V_B(|\mathbf{r} + \mathbf{R}|) | \phi_k^B(\mathbf{r}) \rangle_{\mathbf{r}} \\
G_{jk}^{AB} &= e^{i\Delta t} \langle \phi_j^A(\mathbf{r}) | e^{i\mathbf{v}\cdot\mathbf{r}} (H_e - \epsilon_k^B) | \phi_k^B(\mathbf{r} - \mathbf{R}) \rangle_{\mathbf{r}} \\
G_{jk}^{AB} &= e^{-i\Delta t} \langle \phi_k^B(\mathbf{r} - \mathbf{R}) | e^{-i\mathbf{v}\cdot\mathbf{r}} (H_e - \epsilon_j^A) | \phi_k^A(\mathbf{r}) \rangle_{\mathbf{r}}
\end{aligned}$$

where the indices A and B indicate the center of the given state, $\triangle = (\epsilon_j^A - \epsilon_k^B) + \upsilon^2/2$ and $H_e = -\frac{1}{2}\nabla_{\mathbf{r}}^2 + V_A(r) + V_B(|\mathbf{r} - \mathbf{R}|)$. Note that $(H_e - \epsilon_j^A)\phi_j^A(\mathbf{r}) \neq V_B(|\mathbf{r} - \mathbf{R}|)\phi_j^A(\mathbf{r})$ since $\phi_j^A(\mathbf{r})$ is not the exact eigenfunction of the internal atomic Hamiltonian H_A and the same argument applies to $G_{jk}^{AB}(t)$. The detailed numerical computation of these matrices associated with the even tempered basis functions can be found in Kuang [3].

The close-coupling equation for transition amplitudes is solved by using a standard 4-th Order Runge-Kutta integration scheme with adaptive step-size. This procedure gives a better performance compared to the fixed step-size one, but the matrices $\mathbf{S}$ and $\mathbf{G}$ must be pre-calculated at any time t. Here we shall not go into the details of the numerical difficulties, since the resolution of the numerical bottlenecks for integrating the coupled differential equation also can be found in Kuang [3].

2.2.3 Cross Sections

Since the time-dependent Schrödinger Equation (2.14) depends implicitly on the impact parameter, we denote the coefficients $\mathbf{A}_j(t)$ as $\mathbf{A}_j(\mathbf{b}, t)$. If the initial state is i, the initial condition for the standard time-integration procedure can be specified by

$$\lim_{t \to -\infty} A_j(\mathbf{b}, t) = \delta_{ji}. \tag{2.23}$$

Since the overlap matrix elements vanish at $t \to \infty$, the probability amplitude for transition from state $|\phi_i\rangle$ to final state $|\phi_f\rangle$ is

$$A_{fi}(\mathbf{b}) = \lim_{t \to \infty} \langle \phi_f | \psi \rangle = A_f(\mathbf{b}, t \to \infty) \tag{2.24}$$

The cross section σ_{fi} for the corresponding transition is obtained by integrating the transition probability over all impact parameters b

$$\sigma_{nlm} = 2\pi \int_{b_{min}}^{+\infty} b db |A_{fi}(b, t \to +\infty)|^2. \tag{2.25}$$

One can also calculate the corresponding angular differential cross section [**?**] by

$$\frac{d\sigma_{fi}}{d\theta} = 2\pi sin\theta |\alpha_{fi}|^2 \tag{2.26}$$

where

$$\alpha_{fi}(\theta) = \gamma \int_0^{+\infty} bF(b) db J_{|m_f - m_i|}(2b\mu v_o sin\frac{\theta}{2}) \tag{2.27}$$

$$F(b) = A_{fi}(b, +\infty) e^{2\frac{i}{v_o} Z_T Z_P \ln b} \tag{2.28}$$

with $\gamma = \mu\nu(-i)^{|m_f - m_i|+1}$, μ the reduced mass, v_o the relative collision velocity and m_f (m_i) the magnetic quantum number of the final (initial) state. The symbol $J_{\Delta m}(2b\mu v_o sin\frac{\theta}{2})$ denotes a Bessel function of the first kind. The additional phase $e^{2\frac{i}{v_o} Z_T Z_P \ln b}$ is the eikonal phase due to the Coulomb repulsion between the two nuclei and Z_T (Z_P) is the effective charge of the target (projectile) that defines the Coulomb trajectory of the two colliding nuclei. Since charge transfer occurs far outside the core of both atomic ions, an effective charge of one was used for each.

The numerical evaluation of the diffraction integral (2.27) should be done with care since it involves rapidly oscillating integrands. We divide the range of impact parameters

into small sectors, and within each sector the integrand is expressed as $F(b)exp(i\omega \ln b)$. The evaluation of the integral over the sector is done by substituting $x = \ln b$ and rewriting the integral in the form of

$$\int_{x_n}^{x_{n+1}} (a_1 x^2 + a_2 x + a_3) exp(iwx) dx, \tag{2.29}$$

where we have fitted the function $F(b)$ within the sector by a quadratic function. The integration over this sector can then be performed analytically. For a converged result, it is essential to ensure that within each sector the function $F(b)$ is well-behaved with respect to $x = \ln b$. The accuracy of this algorithm can be checked by varying the size of the sectors or by using another algorithm like the Simpson rule. We further checked that the total cross sections obtained from integrating DCS over scattering angles and from integrating electron capture probabilities over impact parameters are identical.

Bibliography

[1] B.H. Bransden and M.R.C McDowell, *Charge Exchange and the Theory of Ion-Atom Collision*, (Oxford: Clarendon) (1992).

[2] Wolfgang Fritsch and C.D. Lin, Phys. Rep., **202**, 1 (1991)

[3] Jiyun Kuang, *Ph.D Thesis*, Kansas State University (1996)

[4] Jiyun Kuang and C.D. Lin, J. Phys. B **29**, 1207 (1996)

[5] D.R. Bates and R. McCarroll, Proc. Roy. Soc **A245**, 175 (1958)

[6] C.M. Reeves, J. Chem. Phys. **39**, 1 (1963)

Chapter 3

Quantum-Mechanical Representation

This chapter is devoted to the compilation of various theoretical methods and computational techniques used in the hyperspherical coordinate approach for treating ion-atom collisions at low energies. The detailed theory of the hyperspherical coordinate approach for atomic and other Coulombic three-body systems has been reviewed by Lin [1]. Here we shall only recapitulate the essential formulae in this *Adiabatic Hyperspherical R-matrix Close-Coupling* (HSCC) approximation which has been developed and is considered to represent the physical picture as simply and intuitively as the conventional Born-Oppenheimer (BO) approach. Recently, this method has been used to study the charge transfer reaction in He^{2+} + H collisions at low energies [2] and other slow ion-atom collision systems [3, 4] as well.

3.1 Jacobi and Hyperspherical Coordinates

For low-energy ion-atom collisions, charge transfer and direct excitation are the dominant processes. As in the previous chapter, let us consider a simple ABe three body ion-atom collision system in the center of mass frame. We define three configurations (α, β, γ) of internal Jacobi coordinates, as illustrated in Fig. (3.1). Using atomic units, we designate

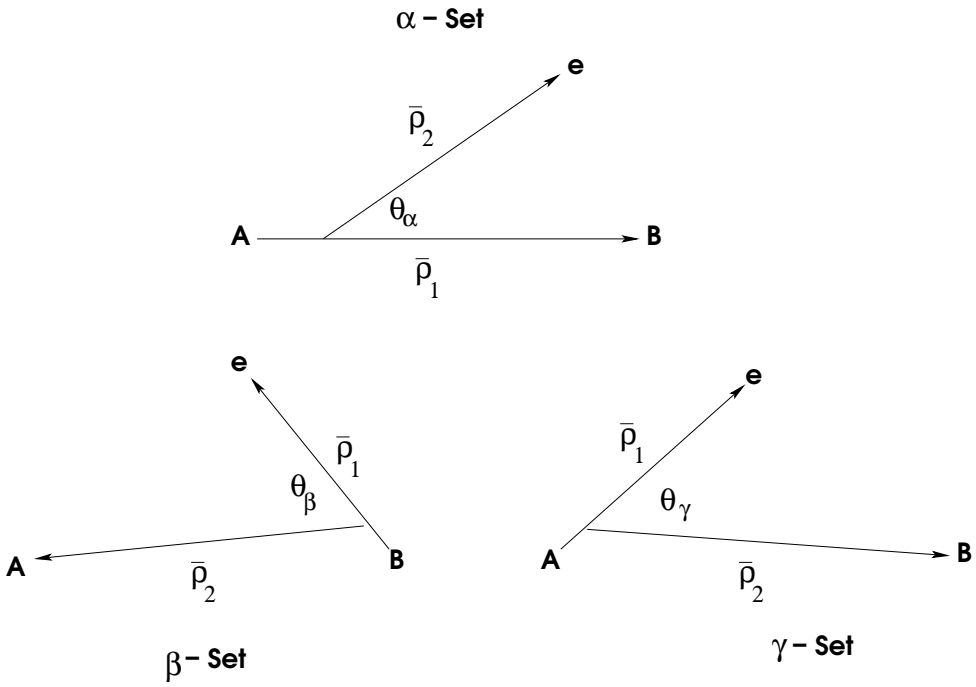

Figure 3.1: Definition of 3 sets of Jacobi coordinates

the mass of each of the three particles by m_A, m_B, and m_e, respectively. In the α-set, the Jacobi coordinate $\vec{\xi_1}^{\alpha} = \sqrt{\frac{\mu_1}{\mu}}\vec{\rho_1}$ defines the vector from ion A to ion B, with reduced mass μ_1; and the second vector $\vec{\xi_2}^{\alpha} = \sqrt{\frac{\mu_2}{\mu}}\vec{\rho_2}$ from the center-of-mass of the molecular ion to the electron. Clearly, one also can define another two sets of coordinate systems in Fig. (3.1). The β-set coordinates consist of the first Jacobi vector from ion B to the electron, and the second Jacobi vector is from the center of mass of (B+e$^-$) to ion A. This set is used to describe the scattering of the ion A with atom B. Similarly, for the γ-set, Jacobi coordinates can be defined to describe B and the (A+e$^-$) system.

The advantage of utilizing Jacobi coordinates is that they separate the motion of the center-of-mass (CM) and the relative internal motion of the three particles, and all essential physical features appear in the CM reference frame. Furthermore, the two internal vectors in Jacobi coordinates are separated from each other in the kinetic energy operator, thus making the mathematical and numerical calculations simpler to handle.

The three Jacobi coordinate sets are not independent since they are related by kinematic rotation. In principle, any one of these three sets is appropriate to describe the internal motion of the three particles. However, for numerical computation efficiency, the effectiveness of each set is very different depending on the various configurations. For example, the so-called *dissociated configuration* where ion A is far away from the (B+e$^-$) system, the internal motion of the system consists of two almost independent movements: the relative motion between ion B and electron e$^-$ and the motion between the (B+e$^-$) pair and ion A. Clearly, the β-set will be much more appropriate for this configuration than the other two, since its $\vec{\rho_1}$, and $\vec{\rho_2}$ vectors are just connecting B and e$^-$, (B+e$^-$) and A, respectively. On the other hand, if ion B is far away from A and e$^-$, then the γ-set is more suitable. Another configuration with electron e$^-$ far away from A and B is virtually impossible except for the three-body breakup, because of the Coulomb repulsion between the two positively charged ions. If the distances between the three particles are comparable with each other, the α-set is a natural choice since it provides an intermediate connection on equal footing with the two dissociation configurations.

In the hyperspherical coordinate method, we replace the independent particle radial variables $\vec{\rho_1}$ and $\vec{\rho_2}$ by the mass-weighted hyperradius R and hyperangle ϕ defined by

$$R^2 = \xi_1^2 + \xi_2^2 \tag{3.1}$$

$$tan\phi = \sqrt{\frac{\mu_2}{\mu_1}}\frac{\rho_2}{\rho_1} \tag{3.2}$$

and

$$cos\theta = \frac{\vec{\rho_1} \cdot \vec{\rho_2}}{\rho_1 \rho_2} \tag{3.3}$$

In these expressions, μ is an arbitrary scaling factor. For the α-set, the reduced masses μ_1 and μ_2 associated with the Jacobi coordinates $\vec{\rho_1}$ and $\vec{\rho_2}$ are

$$\frac{1}{\mu_1} = \frac{1}{m_A} + \frac{1}{m_B}; \ \frac{1}{\mu_2} = \frac{1}{m_A + m_B} + \frac{1}{m_e} \tag{3.4}$$

From the definitions of the coordinates, ϕ and θ measure the radial and angular correlations, respectively; while the hyperradius R specifies the size of the three-body system. The range of ϕ is from 0 to $\pi/2$ and θ ranges from 0 to π.

For each Jacobi coordinate system, a set of new mass-weighted hyperspherical coordinate similar to eqns. (3.1) and (3.2) can be defined. A special notable feature of the

hyperspherical coordinates is that the hyperradius, R, is completely symmetric under permutations of these particles. In the following we will express the equations using the α-set configuration. When quantities are expressed in β- or γ-set coordinates, superscripts of β or γ will be used. In the α-set coordinates the formulation of the hyperspherical close-coupling method is very similar to the Perturbed Stationary State (PSS) model [5]. We will choose μ to be the reduced mass of the two heavy nuclei. The hyperradius R then becomes very close to the internuclear distance. From eqn. (3.1), the difference is of the order of $\sqrt{\mu_2/\mu_1}$, which is roughly the square root of the mass of the electron over the reduced mass of the two heavy particles.

The introduction of Jacobi and hyperspherical coordinates is essential in the treatment of the three-body systems. It provides a unified means for further analysis of the physical system.

3.2 Hyperradial Form of Schrödinger Equation

The hyperspherical coordinate method was devised to numerically solve the multidimensional Schrödinger equation for a few-body system and explicitly constructing the wave function by exploiting the so-called *adiabatic expansion*. The Schrödinger equation for a general three-body system can be written as

$$\{\sum_q -\frac{1}{2m_q}\frac{\partial^2}{\partial \vec{x}_q^2} + \sum_{p\neq q} V_{pq}\}\psi = E\psi \tag{3.5}$$

where p and q symbolize the charged particles A, B and e$^-$. The $\vec{x}_q$ are vectors pointing from the origin to particles A, B and e$^-$, respectively, in the *space-fixed frame*. ψ is the total wave function and the potential V_{pq} is the pair interaction between particles p and q. m_q are the masses for the charged particles. For a Coulombic system, the potential is expressed explicitly by

$$V = \sum_{p\neq q} V_{pq} = \frac{Z_A Z_B}{x_{AB}} + \frac{Z_B Z_e}{x_{Be}} + \frac{Z_e Z_A}{x_{eA}}$$

where Z_A, Z_B and Z_e are the magnitude of electric charges of the particles, whereas x_{AB}, x_{Be} and x_{eA} are the distances between (A+B), (B+e^-) and (e^-+A), respectively. In hyperspherical coordinate defined in eqns. (3.1) and (3.2) for a specific Jacobi coordinates set (i.e; α, β or γ-set), omitting the term of center of mass motion, the Schrödinger equation

can be written in this form

$$(-\frac{1}{2\mu}[\frac{\partial^2}{\partial^2 R}+\frac{5}{R}\frac{\partial}{\partial R}+\frac{1}{sin^2\phi cos^2\phi}\frac{\partial}{\partial\phi}(sin^2\phi cos^2\phi)$$
$$-\frac{\vec{l_1}^2(\hat{r_1})}{R^2cos^2\phi}-\frac{\vec{l_2}^2(\hat{r_2})}{R^2sin^2\phi}]+V)\psi=E\psi.$$

Here $\vec{l_1}(\hat{r_1})$ and $\vec{l_2}(\hat{r_2})$ are the angular momentum operators corresponding to vectors $\hat{\rho_1}$ and $\hat{\rho_2}$ defined in eqn. (3.1), respectively (see Fig. 3.1). Without the perturbation of any external fields, there are four good quantum numbers for a time-independent isotropic system; namely, the total energy E of the collision system, the parity $\prod$, the total angular momentum J as well as its projection on the space-fixed z-axis.

Let us introduce the rescaled wave function of the form

$$\Psi(R,\phi,\Upsilon)=\psi R^{5/2}\sin\phi\cos\phi, \tag{3.6}$$

with $\Upsilon\equiv\{\theta_1,\phi_1,\theta_2,\phi_2\}$ being the collective orientation angles of vectors $\vec{\rho_1}$ and $\vec{\rho_2}$, the time-independent Schrödinger equation can be further reduced to

$$\left(-\frac{1}{2\mu R^2}\frac{\partial^2}{\partial R^2}+\frac{\Lambda^2}{2\mu R^2}+V-\frac{1}{8\mu R^2}\right)\Psi(R,\phi,\Upsilon)=E\Psi(R,\phi,\Upsilon) \tag{3.7}$$

with the squared grand angular momentum

$$\Lambda^2=\left(-\frac{\partial^2}{\partial^2\phi}+\frac{\vec{l_1}^2}{sin^2\phi}+\frac{\vec{l_2}^2}{cos^2\phi}\right)-\frac{1}{4} \tag{3.8}$$

and

$$RV=\sqrt{\frac{\mu_1^\alpha}{\mu}}\frac{Z_AZ_B}{cos^\alpha\phi}+\sqrt{\frac{\mu_1^\beta}{\mu}}\frac{Z_BZ_e}{cos^\beta\phi}+\sqrt{\frac{\mu_1^\gamma}{\mu}}\frac{Z_eZ_A}{cos^\gamma\phi} \tag{3.9}$$

is the effective potential surface among the three interacting charged particles and is scaled with the masses of the system. The angles $\{\phi,\theta\}$ on the left-hand side can be in any one of the three Jacobi sets. Note that it is possible to treat non-Coulombic ion-atom collision by simply replacing the pair interaction with realistic model potentials. Nevertheless, it is unrealistic to accurately solve a six dimensional differential equation (3.7). Therefore in order to solve this equation, an appropriate approximation is necessary to reduce the dimensionality.

3.3 Adiabatic Hyperspherical Approximation

The idea of adiabatic separability between the hyperradius and the hyperangular variables in few-body systems was first exploited by Macek for studying the doubly excited states of He atom [6]. The gist of this approximation assumes that the hyperradius R varies slowly compared with the five angles (ϕ,Υ), such that one can treat R as an adiabatic parameter like the inter-nuclear separation in the Born-Oppenheimer approximation. The purpose of this hyperspherical method is to seek the solution in a form of adiabatic expansion

$$\Psi(R, \phi, \Upsilon) = \sum_{\mu} F_{\mu}(R)\Phi_{\mu}(R; \phi, \Upsilon) \tag{3.10}$$

where the adiabatic channel functions $\Phi_{\mu}(R; \phi, \Upsilon)$ satisfy the hyperspherical adiabatic eigenvalue equation

$$H_{ad}(R; \phi, \Upsilon)\Phi_{\mu}(R; \phi, \Upsilon) = U_{\mu}(R)\Phi_{\mu}(R; \phi, \Upsilon). \tag{3.11}$$

with $U_{\mu}(R)$ being a potential energy surface, and the adiabatic Hamiltonian $H_{ad}(R;\phi,\Upsilon)$ is defined by

$$H_{ad}(R; \phi, \Upsilon) = \frac{\Lambda^2}{R^2} + 2\mu V \tag{3.12}$$

Note that $H_{ad}(R;\phi,\Upsilon)$ is an operator in (ϕ,Υ) which parametrically depends on R. In such cases, here and further on, we use a semicolon to separate "fast" and "slow" parameters in the arguments of an operator and its eigenfunctions. For any value of R, the channel functions $\Phi_{\mu}(R; \phi, \Upsilon)$ form a complete orthonormal basis on the hypersphere,

$$\langle \Phi_{\mu}(R; \phi, \Upsilon) \mid \Phi_{\nu}(R; \phi, \Upsilon) \rangle = \delta_{\mu\nu} \tag{3.13}$$

where $\langle ..|.. \rangle$ denotes integration over (ϕ,Υ). Substituting eqn. (3.10) into eqn. (3.7) we obtain the following set of ordinary differential equations defining the radial functions $F_{\mu}(R)$:

$$\left(\frac{d^2}{dR^2} + \frac{1}{4R^2} - U_{\mu}(R) + W_{\mu\nu}(R) + 2\mu E \right) F_{\mu}(R) + \sum_{\mu \neq \nu} W_{\mu\nu}(R) F_{\nu}(R) = 0 \tag{3.14}$$

where the operator

$$W_{\mu\nu}(R) = 2P_{\mu\nu}(R)\frac{d}{dR} + Q_{\mu\nu}(R) \tag{3.15}$$

represents the non-adiabatic couplings, and where

$$P_{\mu\nu}(R) = \left\langle \Phi_\mu(R;\phi,\Upsilon) \mid \frac{\partial}{\partial R}\Phi_\nu(R;\phi,\Upsilon) \right\rangle; \tag{3.16}$$

$$Q_{\mu\nu}(R) = \left\langle \Phi_\mu(R;\phi,\Upsilon) \mid \frac{\partial^2}{\partial^2 R}\Phi_\nu(R;\phi,\Upsilon) \right\rangle \tag{3.17}$$

In summary, equations (3.10) – (3.17) complete the formulation of the adiabatic hyperspherical coordinate method. The adiabatic approximation is useful if the off-diagonal coupling terms are small. In this case, the index μ is used to label the "channels". The hyperradial function $F_\mu(R)$ gives the size of the state, but the internal motion together with the overall rotation of the whole system, is contained in the channel function. Now, we can proceed to use a two-step process to solve the Schrödinger equation. First, we solve the adiabatic eigenvalue equation (3.11). Then, we solve the 1-D radial coupled differential equation (3.14).

3.4 Channel Function and Matrix Elements

There are generally two different ways to solve the eigenvalue problem. The first approach is to expand the channel function in terms of an analytical basis set in the space-fixed frame which we shall not be using in our subsequent calculations. However, for completeness, we shall outline the basis set in the space-fixed frame. The second approach is to express Φ_μ and eqn. (3.11) in a body-fixed frame. One can replace the five angles in the hyperspherical coordinates discussed earlier by three Euler angles which describe the rotation of the system, and two other internal angles (ϕ, θ) that defined earlier which account for the internal motion of the three particles. In this way, we can simply separate out the three Euler angles and the internal relative motion.

3.4.1 Channel Function in Space-Fixed Frame (SF)

Briefly, one can seek two types of solutions in the space-fixed frame [23]: (i) hyperspherical harmonics functions

$$N_{l_1 l_2 m} sin^{l_1}\phi cos^{l_2}\phi \mathcal{P}_m^{(l_1+\frac{1}{2},l_2+\frac{1}{2})}(cos2\phi)\mathcal{Y}_{l_1 l_2}^{JM}(\hat{\rho}_1,\hat{\rho}_2) \tag{3.18}$$

and (ii) Slater-type orbital functions

$$\tilde{N}_{l_1 l_2 m} sin^{l_1}\phi cos^{l_2}\phi(\rho_1)^n exp(-\alpha\rho_1)\mathcal{Y}^{JM}_{l_1 l_2}(\hat{\rho}_1, \hat{\rho}_2) \tag{3.19}$$

where

$$\mathcal{Y}^{JM}_{l_1 l_2}(\hat{\rho}_1, \hat{\rho}_2) = \sum_{m_1, m_2} \langle l_1 m_1 l_2 m_2 | JM \rangle \, Y_{l_1 m_1}(\hat{\rho}_1) Y_{l_2 m_2}(\hat{\rho}_2)$$

is the coupled angular momentum function of the total angular momentum J and its projection on the z-axis component J_z express in any three sets of the Jacobi coordinate. The $\mathcal{P}_m^{(l_1+\frac{1}{2}, l_2+\frac{1}{2})}(cos2\phi)$ is the Jacobi polynomials. The harmonics functions on the hyperspherical surface of a six-dimensional space are simultaneous eigenfunctions of Λ^2, $\vec{l}_1^2$, $\vec{l}_2^2$, J^2 and J_z, where $\vec{J} = \vec{l}_1 + \vec{l}_2$.

The hyperspherical harmonics are useful for representing the channel functions in the small R region while the Slater-type orbitals are suitable for describing the dissociation limit. In this prescription, it is necessary to use both basis sets since using only one or the other will cause numerical convergence problems at small R and in the asymptotic region [7]. The intrinsic numerical problem associated with the use of these two linearly dependent bases is well-known when a large number of basis functions is required [8].

3.4.2 Channel Function in Body-Fixed Frame (BF)

There are many ways of choosing the quantization axis in the body-fixed frame for a three-body system. In the case of chemical physics, it is normal to choose one of the principal axes to be the quantization axis. For the three-body ion-atom collision system, the axis connecting the two heavy particles of identical charges is a good quantization. The reasons are: (i) with this quantization axis, the relative coordinates of the three particles in the α-set are easily described. (ii) the repulsive Coulombic force between the two identically charged particles tends to push one away from the other and therefore it may serve as a better quantization axis.

Fig. (3.2) portrays the schematic diagram of the (x', y', z') body-frame we have adopted. The body-frame z'-axis is along $\vec{\xi}_1^{\alpha}$. The y'-axis is defined to be along a direction perpendicular to the plane of the three particles (i.e., $\hat{t} = \frac{\vec{\xi}_1 \times \vec{\xi}_2}{|\vec{\xi}_1 \times \vec{\xi}_2|}$) and the x'-axis is

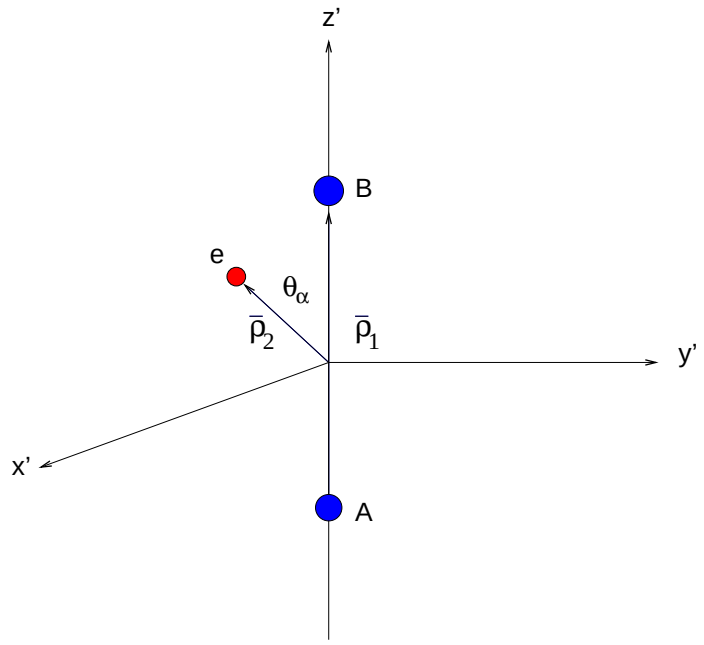

Figure 3.2: Body-fixed frame. The three particles lie on the x'-z' plane with the z'-axis along the line connecting particles A and B

given by $\hat{t} \times \hat{\xi}_1$ such that the body-frame (x', y', z') axes are the three triads ($\hat{t} \times \hat{\xi}_1$, $\hat{t}$ and $\hat{\xi}_1$) and the Euler angles of the body-frame are $\Omega = (\omega_1, \omega_2, \omega_3)$, with $\omega_2 = \theta_1$, $\omega_1 = \phi_1$, where (θ_1, ϕ_1) are spherical angles of $\hat{\xi}_1$. By expressing the angular momentum operators $\vec{l}_1^2$ and $\vec{l}_2^2$ in terms of the angular momentum operators with respect to the body-frame axes and the angle θ, one can decompose the grand angular momentum, and the explicit form of the "*squared grand angular momentum operator*" is given [1, 9, 10] by $\Lambda^2 = T_0 + T_1 + T_2 – 1/4$, where

$$T_0 = -\frac{\partial^2}{\partial\phi^2} - \frac{1}{sin^2\phi cos^2\phi sin\theta}\frac{\partial}{\partial\theta}\left(sin\theta\frac{\partial}{\partial\theta}\right) \tag{3.20}$$

$$T_1 = \frac{\hat{l}_{z'}^2}{sin^2\phi cos^2\phi sin^2\theta} - \frac{(2\hat{l}_{z'}^2 - J^2)}{cos^2\phi} \tag{3.21}$$

$$T_2 = \frac{\left(2i\hat{l}_{y'}\frac{\partial}{\partial\theta} + 2cot\theta\hat{l}_{x'}\hat{l}_{z'}\right)}{cos^2\phi} \tag{3.22}$$

and the angular momentum operators with respect to the body-frame axes are

$$\hat{l}_{x'} = -i\left(sin\omega_3\frac{\partial}{\partial\omega_2} - \frac{cos\omega_3}{sin\omega_2}\frac{\partial}{\partial\omega_1} + cot\omega_2 cos\omega_3\frac{\partial}{\partial\omega_3}\right) \tag{3.23}$$

$$\hat{l}_{y'} = -i\left(cos\omega_3\frac{\partial}{\partial\omega_2} + \frac{sin\omega_3}{sin\omega_2}\frac{\partial}{\partial\omega_1} - cot\omega_2 cos\omega_3\frac{\partial}{\partial\omega_3}\right) \tag{3.24}$$

$$\hat{l}_{z'} = -i\frac{\partial}{\partial\omega_3} \tag{3.25}$$

where (ω_1, ω_2, ω_3) are the three Euler angles of the body-frame axes with respect to the space-fixed frame [11].

It seems that the Schrödinger equation in the body-frame representation is more complex. However, the beauty of it is that, the wave function which describes the overall rotation can be easily separated out. We, therefore, seek the solution of eqn. (3.11) by expanding the channel function in the form of

$$\tilde{\Phi}(R,\phi,\theta,\Omega) = \sum_{I=0}^{J}\sum_{\mu=1}^{N}\Phi_{\mu I}(R;\phi,\theta)\tilde{D}^{J\Pi}_{IM_J}(\Omega) \tag{3.26}$$

where $I(M)$ denotes the projection of J on the body-fixed (laboratory-fixed) quantization axis and $\tilde{D}^{J\Pi}_{IM}(\Omega)$ is the normalized and symmetrized Wigner D-function associated with our choice of the body-frame[9]

$$\tilde{D}^{J\Pi}_{IM}(\Omega) = \frac{\sqrt{2J+1}}{4\pi\left[1+(\sqrt{2}-1)\delta_{I0}\right]}\left(D^J_{IM}(\Omega) + (-1)^{I+J}\Pi D^J_{-IM}(\Omega)\right)$$

which are eigenfunctions of operators J^2, J_z and $l^2_{z'}$. Π defines the parity of the system. If $(-1)^J\ \Pi = 1$, I runs from 0 to J else if $(-1)^J\Pi = -1$, I runs from 1 to J. The set of Euler angles $\Omega \equiv (\omega_1, \omega_2, \omega_3)$ defines the body-frame with respect to the laboratory-fixed frame.

3.4.3 Coupling Matrix Elements in Body-Fixed Frame

Specifically, in the body-frame representation, we expand the total wave function in terms of a product of radial function $F(R)$, adiabatic basis functions $\Phi_{\mu I}(R;\theta,\phi)$ and the normalized and symmetrized rotation functions $\tilde{D}(\Omega)$ [12]:

$$\Psi(R,\theta,\phi,\Omega) = \sum_{\mu}\sum_{I}F_{\mu I}(R)\Phi_{\mu I}(R;\phi,\theta)\tilde{D}^{J\Pi}_{IM_J}(\omega_1,\omega_2,\omega_3), \tag{3.27}$$

where μ is the channel index, J is the total angular momentum, I is the absolute value of the projection of vector $\vec{J}$ along the z'-axis and M_J is the projection of vector $\vec{J}$ along the space-fixed z-axis. By definitions of eqns. (3.21) and (3.22), the coupling matrix elements are

$$\begin{aligned}\left\langle \tilde{D}^{J\Pi}_{IM_J}|T_1|\tilde{D}^{J\Pi}_{I'M_J}\right\rangle &= \left[I^2\left(\frac{1}{\sin^2\phi\cos^2\phi\sin^2\theta}-\frac{2}{\cos^2\phi}\right)\right.\\ &\quad \left.+J(J+1)\left(\frac{1}{\cos^2\phi}\right)\right]\delta_{II'},\end{aligned} \tag{3.28}$$

$$\begin{aligned}\left\langle \tilde{D}^{J\Pi}_{IM_J}|T_2|\tilde{D}^{J\Pi}_{I'M_J}\right\rangle &= \gamma^J_{I\,I+1}h_{I\,I+1}\delta_{I'\,I+1}+\gamma^J_{I\,I-1}h_{I\,I-1}\delta_{I'\,I-1}\\ &= \bar{T}_2,\end{aligned} \tag{3.29}$$

with

$$h_{I\,I\pm1} = \frac{1}{\cos^2\phi}\left(\pm\frac{\partial}{\partial\theta}+(I\pm1)\cot\theta\right), \tag{3.30}$$

$$\gamma^J_{I\,I+1} = -[1+(\sqrt{2}-1)\delta_{I0}][(J+I+1)(J-I)]^{1/2}, \tag{3.31}$$

$$\gamma^J_{I\,I-1} = -[1+(\sqrt{2}-1)\delta_{I0}][(J-I+1)(J+I)]^{1/2}. \tag{3.32}$$

Note that $\langle||\rangle$ denotes an integration over Ω and both operators, T_0 and T_1 are diagonal with respect to the magnetic components I along the z' axis of the body-frame, whereas T_2 couples only states with adjacent I components.

In order to efficiently treat a large number of partial waves, Λ^2 is separated into two parts, each of which depends only on I and J, respectively,

$$\left\langle \tilde{D}^{J\Pi}_{IM_J}|T_1|\tilde{D}^{J\Pi}_{IM_J}\right\rangle = I^2T_{1a}+J(J+1)T_{1b}. \tag{3.33}$$

The adiabatic basis functions $\Phi_{\mu I}(R;\theta,\phi)$ are chosen to satisfy

$$\left[T_0+I^2T_{1a}+2\mu VR\right]\Phi_{\mu I}(R;\theta,\phi) = 2\mu R^2U^I_\mu(R)\Phi_{\mu I}(R;\theta,\phi). \tag{3.34}$$

The $\Phi_{\mu I}$ are obtained by solving the eigenvalue problem with a large two-dimensional (θ and ϕ) B-spline basis set [13], thus determining adiabatic potential curves $U^I_\mu(R)$ for each I and a set of orthonormal adiabatic basis functions $\Phi_{\mu I}(R;\phi,\theta)$ that depend parametrically on R. Specifically, the channel functions are expanded in terms of a direct product of fifth-order B-splines in ϕ and θ. Note that $\Phi_{\mu I}$ is not an eigenfunction of the adiabatic

Hamiltonian $H_{\rm ad}$. The eigenfunctions of the adiabatic Hamiltonian can be obtained by diagonalizing the tri-diagonal block matrix, constructed by

$$\begin{pmatrix} X^{I=0} & Y^{+} & \dots \\ Y^{-} & X^{I=1} & \dots \\ \vdots & \vdots & \ddots \end{pmatrix}, \tag{3.35}$$

where

$$X^{I}_{\mu\nu}(R) = 2\mu R^2 U^{I}_{\mu}\delta_{\mu\nu} + J(J+1)\left\langle \Phi_{\mu I}(R_i;\phi,\theta)|T_{1b}|\Phi_{\nu I}(R_i;\phi,\theta)\right\rangle, \tag{3.36}$$

$$\begin{aligned} Y^{\pm}(R) &= \left\langle \Phi_{\mu I}(R_i;\phi,\theta)|\bar{T}_2|\Phi_{\nu I\pm 1}(R_i;\phi,\theta)\right\rangle \\ &= \gamma^{J}_{II\pm 1}\left\langle \Phi_{\mu I}(R_i;\phi,\theta)|h_{II\pm 1}|\Phi_{\nu I\pm 1}(R_i;\phi,\theta)\right\rangle \end{aligned} \tag{3.37}$$

The advantage of such a partition is that these basis functions Φ need to be calculated only once for all the J's . So do the matrix elements, $\langle\Phi_{\mu I}|T_{1b}|\Phi_{\nu I}\rangle$ and $\langle\Phi_{\mu I}|h_{II\pm 1}|\Phi_{\nu I\pm 1}\rangle$, which are required in constructing matrices $\mathbf{X}$ and $\mathbf{Y}$. As a result, constructing the adiabatic Hamiltonian for a given J involves only fast algebraic operations within a given I subspace. Such an efficient approach is critical since hundreds or thousands of partial waves need to be included in order to obtain a converged cross section even for collisions at thermal energies and above.

3.5 Solution of Coupled Hyperradial Equations

The procedure of adiabatic separation of variables allows one to reduce the original multidimensional problem to a set of coupled 1-D differential equations, such as eqn. (3.14). This greatly simplifies the problems. However, in order to treat the non-adiabatic couplings one still has to solve these equations. Qualitatively, the effects of the non-adiabaticity can be studied using different analytic models [14, 15]. However, an accurate solution usually requires numerical treatments. The approach anchored on direct use of the adiabatic expansion is not the best for this purpose, since it leads to equations that are known to suffer from the following practical problems: (i) they require explicit evaluation of the non-adiabatic coupling $P_{\mu\nu}$ and $Q_{\mu\nu}$ matrices, which involves numerical differentiation of the adiabatic channel functions with respect to the adiabatic variable and the derivative

can vary rapidly near a localized avoided crossing, and (ii) their resolution requires a mesh adjusted to the variations of the coupling coefficients, which may be very dense in the vicinity of avoided crossings of adiabatic potentials, whose locations, however are not usually known in advance.

Two well-known procedures have been used to address such numerical difficulties. The first procedure is the "diabatization" of the subset of adiabatic functions, commonly employed in ion-atom and ion-molecule collision calculations within the PSS or the MO-ETF models [16, 17, 18, 19]. Before the diabatization procedure, one needs to obtain non-adiabatic coupling matrix elements accurately and this has to be done very carefully in the region of the avoided crossing. The second method, which was designed to bypass the calculation of non-adiabatic coupling matrix elements, is the so-called Diabatic-By-Sector (DBS) method. This method, which is very popular in chemical reaction calculations [20] and has been applied to study doubly excited states of H^-, Ps^- and electron/positron and hydrogen collisions [9, 10, 21, 22, 23, 24, 25], is free from these problems. However, for a fixed number of adiabatic channels, this approach contains intrinsic mathematical problem that cannot be eliminated even by making the size of the sector infinitesimally small [26]. The Slow/Smooth Variable Discretization (SVD) method introduced by Tolstikhin *et al* [27] can circumvent this drawback of the DBS method while preserving the simplicity of its implementation. The combination of the SVD method and the $\mathcal{R}$-matrix propagation scheme has been efficiently applied to study electron scattering by hydrogen atoms [28] and atom-diatom collisions [29]. We have adopted this approach and will outline the theory in the following sections.

3.5.1 The Slow/Smooth Variable Discretization (SVD) Method and $\mathcal{R}$-matrix Propagation

The SVD method hinges on the assumption of the *smoothness* of the adiabatic Hamiltonian $H_{ad}(R;\Omega)$ in the adiabatic variable R. The time-independent Schrödinger equation is solved in the discrete-variable representation (DVR) with respect to R. It is convenient to introduce a new function,

$$\Psi(R,\phi,\theta,\Omega) = \psi R^{3/2} sin\phi cos\phi \tag{3.38}$$

and to write the Schrödinger equation in the form:

$$\left(K(R) + H_{ad}(R;\Omega) - \mu R^2 E\right)\Psi(R,\phi,\theta,\Omega) = 0 \tag{3.39}$$

where

$$K(R) = -\frac{1}{2}\frac{\partial}{\partial R}R^2\frac{\partial}{\partial R} + \frac{15}{8} \tag{3.40}$$

represents the kinetic energy of the motion with respect to the hyperradius R. Equation (3.39) should be solved in the interval $R \in [0, R_o]$, where R_o is the matching radius.

We divide the whole interval into an N_{sec} number of sectors with boundaries at $\bar{R}_k$:

$$0 < \bar{R}_1 < \bar{R}_2 < \bar{R}_3 < \cdots < \bar{R}_{N_{sec}} = R_o \tag{3.41}$$

Such sectorization is not essential for the method, but it is convenient in practice, since it allows one to reduce the dimension of the matrices considered. Solutions within an interval $[a, b]$ of a sector can be formally written in terms of the Green's function defined within the interval,

$$\Psi(R,\Omega) = \int_a^b dR' \int d\Omega' \mathcal{G}(R,\Omega;R',\Omega')\mathcal{L}(R')\Psi(R',\Omega'), \tag{3.42}$$

where $\mathcal{L}$ is the Bloch operator defined as

$$\mathcal{L}(R) = R^2[\delta(R-b)\frac{\partial}{\partial R} - \delta(R-a)\frac{\partial}{\partial R}] \tag{3.43}$$

to Hermitize the kinetic energy operator for the motion in R within an interval $[a, b]$. A spectral resolution of the Green's function can be written as

$$\mathcal{G}(R,\Omega;R',\Omega') = \sum_k \frac{u_k(R,\Omega)u_k(R',\Omega')}{\mu(E_k - E)}, \tag{3.44}$$

where $u_k(R, \Omega)$ and E_k be the eigenfunctions and eigenvalues of the equation

$$\left(\tilde{K}(R) + H_{ad}(R;\theta,\phi) - \mu R^2 E_k\right)u_k(R,\theta,\phi) = 0 \tag{3.45}$$

where $\tilde{K}(R)= K(R) + \mathcal{L}(R)$ and we seek solutions of this equation in the form of the SVD expansion

$$u_k(R,\theta,\phi) = \sum_{i=1}^{M}\sum_{n}^{N} C_{in}^k \pi_i(R)\Phi_n(R_i;\theta,\phi). \tag{3.46}$$

Here $n \equiv [\mu, I]$, R_i are the DVR quadrature points in R in a specific sector and $\pi_i(R)$ is a set of DVR basis functions (see Appendix B) which are constructed from using a set

of orthonormal basis functions based on Jacobi polynomials of degrees up to M-1 within the interval $[a, b]$ and R_j's are the quadrature abscissas of the Jacobi polynomial of degree M within the interval $[a, b]$.

Substituting eqn. (3.46) into eqn. (3.45) we arrive at a SVD algebraic eigenvalue problem defining the coefficients $C^k_{j\mu}$ and the eigenvalues E_k:

$$\sum_{j=1}\sum_{m=1}\left(\tilde{K}_{ij}(R)S_{in,jm} + \mu\rho_{ij}\left[\tilde{U}_{mn}(R_j) - E_k\right]\delta_{ij}\delta_{mn}\right)C^k_{jm} = 0 \tag{3.47}$$

where

$$\tilde{K}_{ij} = \frac{1}{2}\int_a^b \frac{d\pi_i(R)}{dR}R^2\frac{d\pi_j(R)}{dR}dR + \frac{15}{8}\delta_{ij} \tag{3.48}$$

$$\rho_{ij} = \int_a^b \pi_i(R)R^2\pi_j(R)dR \tag{3.49}$$

$$\tilde{U}_{mn}(R_j) = \langle\Phi_m(R_j)|H_{ad}|\Phi_n(R_j)\rangle, \tag{3.50}$$

$$S_{in,jm} = \langle\Phi_n(R_i)|\Phi_m(R_j)\rangle. \tag{3.51}$$

The M-point Gauss quadrature is used to evaluate the integration over R in eqns. (3.47) to (3.51). Therefore, we need to solve the eigenvalue problem eqn. (3.34) only at the values of R corresponding to the quadrature abscissas of the Jacobi polynomials of degree M within each interval.

The advantage of utilizing the SVD method is that one need not explicitly calculate the non-adiabatic coupling matrix elements since these effects are implicitly embedded into the overlap matrix elements of the adiabatic channels at different hyperradii R. Although the calculation of the overlap matrix elements at different values of the hyperradii can be time-consuming, these overlapping matrix elements need to be calculated only once, since the adiabatic channels (cf. eqn. (3.34)) are independent of the total angular momentum J.

Once the basis functions u_k are obtained, the solution $\Psi(R, \Omega)$ can be readily constructed

$$\Psi(R,\Omega) = \sum_k \frac{u_k(R,\Omega)}{\mu(E_k - E)}[b^2\langle u_k|\frac{\partial\Psi}{\partial R}\rangle_{R=b} - a^2\langle u_k|\frac{\partial\Psi}{\partial R}\rangle_{R=a}]. \tag{3.52}$$

The $\mathcal{R}$ matrix with respect to the adiabatic channels is defined at boundaries of the interval as

$$\langle\Phi_n|\Psi\rangle = \sum_m \mathcal{R}_{nm}(R)\langle\Phi_m|\frac{\partial\Psi}{\partial R}\rangle. \tag{3.53}$$

The propagation formula for the $\mathcal{R}$ matrix is in the form,

$$\mathcal{R}_{nm}(b) = G^{bb}_{nm} - \sum_{l}\sum_{l'} G^{ba}_{nl}[G^{aa} + \mathcal{R}(a)]^{-1}_{ll'} G^{ab}_{l'm}, \tag{3.54}$$

where

$$G^{R_1R_2}_{nm} = R_1R_2 \sum_{k} \frac{\langle \Phi_n(R_1)|u_k(R_1)\rangle\langle u_k(R_2)|\Phi_m(R_2)\rangle}{\mu(E_k - E)}. \tag{3.55}$$

The $\mathcal{R}$ matrix is set to zero at $R = 0$. Solutions are calculated and propagated to large R in order to obtain the $\mathcal{R}$ matrix at an asymptotic hyperradius, where the hyperspherical channels converge to various atomic target states and $F_{\mu I}$ can be matched to asymptotic solutions. The advantage of the $\mathcal{R}$-matrix propagation is its stability. Unlike the wave function itself, there is no exponentially decreasing or increasing function in the propagation. Also, the basis functions used in constructing the propagators are energy independent, making it efficient to obtain the wave functions for different energies. Further details of the methods can be found in Refs. [27, 28].

3.5.2 Matching Scheme and Cross Section

Once the inner solutions are propagated to the asymptotic region of hyperradius R_o (i.e., one particle is far away from the other pair of particles), they should be matched with the asymptotic solutions to get the scattering matrix which contains the information on the short-range interaction.

Without considering the three-body breakup process, we expand the asymptotic wave function $\Psi^{as}_{\lambda}(R_o)$ of the dissociated system as

$$\begin{aligned}\Psi^{as}_{\lambda}(\rho_1, \rho_2) \quad &= \sum_{i=1}^{N} [f_i(k_{i\tau}\rho^{\tau}_2)\delta_{i\lambda} - g_i(k_{i\tau}\rho^{\tau}_2)K_{i\lambda}] \\ &\times \varphi_i(\rho^{\tau}_1)\mathcal{Y}_{l^{\tau}_1 l^{\tau}_2 JM_J}(\hat{\rho}^{\tau}_1, \hat{\rho}^{\tau}_2)/\rho^{\tau}_1\rho^{\tau}_2\end{aligned} \tag{3.56}$$

where the wave function is expressed in laboratory-fixed frames and the base functions are given in $\tau = \beta$- or γ-set coordinates. For the present Coulomb three-body system each φ_i is a hydrogenic radial wave function with angular momentum ℓ_1, and the relative angular momentum between the hydrogen-like atom and the heavy particle is ℓ_2, coupled to form a total angular momentum function $\mathcal{Y}_{l_1 l_2 JM_J}$, with total angular momentum J and its projection with respect to the laboratory-fixed quantization axis, M_J. The f and g are

the regular and irregular asymptotic functions. For the A^{Z+}+B asymptotic limit, they are Bessel functions and Neumann functions, respectively. For the A^{Z+}+$B^{Z'+}$ asymptotic limit, they are regular and irregular Coulomb functions, respectively. Note that the wave vector $\vec{k}$ depends on the Jacobi coordinates used. They are related to the kinetic energy for each channel by the relation

$$\frac{1}{2\mu_1^\alpha}k_\alpha^2 = \frac{1}{2\mu_2^\beta}k_\beta^2 = \frac{1}{2\mu_2^\gamma}k_\gamma^2 = E - U_\nu(\infty). \tag{3.57}$$

The general asymptotic solution (3.56) is matched to the inner solution obtained from the $\mathcal{R}$-matrix propagation

$$\frac{1}{R_o^{3/2}\sin\phi\cos\phi}\sum_{\sigma=1}^{N} H_{\sigma\lambda}\Psi^\sigma(R_o) = \Psi_\lambda^{as}(\rho_1,\rho_2)|_{R=R_o} \tag{3.58}$$

where the inner solution is expressed in α-set coordinates and the matching is to be carried out at $R = R_o$. Such a matching procedure has been discussed and employed in Zhou and Lin [9, 10, 21, 22] for e^++H(1s) collisions. It involves transforming the β- and γ-set wave functions into the α-set coordinates from where integration over all the angular coordinates at $R = R_o$ is carried out. In practice this requires a two-dimensional numerical integration involving (ϕ, θ) and the procedure is known as two-dimensional matching. In any event, the matching conditions can be written as

$$\mathcal{F}\mathcal{H} = R_o^{-1}[\mathcal{M} - \mathcal{N}\mathcal{K}] \tag{3.59}$$

$$\mathcal{F}'\mathcal{H} = R_o^{-1}[(\mathcal{M}' - \frac{\mathcal{N}}{R_o}) - (\mathcal{N}' - \frac{\mathcal{N}}{R_o}\mathcal{K})] \tag{3.60}$$

where $\mathcal{M}_{\mu\nu} = f_\mu\delta_{\mu\nu}$ and $\mathcal{N}_{\mu\nu} = g_\mu\delta_{\mu\nu}$ while "prime" here denotes the derivative with respect to hyperradius R. Defining the $\mathcal{R}$-matrix

$$\mathcal{R} = \mathcal{F}\mathcal{F}'^{-1}, \tag{3.61}$$

from eqns. (3.59) and (3.60), we obtain the $\mathcal{K}$-matrix

$$\mathcal{K} = [\mathcal{N} - \mathcal{R}(\mathcal{N}' - \frac{\mathcal{N}}{R_o})]^{-1}[\mathcal{M} - \mathcal{R}(\mathcal{M}' - \frac{\mathcal{M}}{R_o})] \tag{3.62}$$

From the resulting $\mathcal{K}$-matrix, the partial cross sections are obtained:

$$\sigma_{ij} = \frac{4\pi(2J+1)}{k_i^2}\left|\frac{\mathcal{K}}{1-i\mathcal{K}}\right|_{ij}^2. \tag{3.63}$$

Since the wave functions beyond R_o are represented in either the β- or γ-set Jacobi coordinates depending on the dissociation channels, there is no spurious coupling between the channels.

The calculation of the $\mathcal{K}$-matrix using the two-dimensional matching method is often used for calculations at higher precision and at low collision energies. For ion-atom collisions where the matching has to be carried out for each partial wave, it is desirable to simplify the calculation. Consider the Bessel or Coulomb functions which are written as $f(k_\tau \rho_2^\tau)$ or $g(k_\tau \rho_2^\tau)$ in eqn. (3.56); the argument has been written in terms of Jacobi coordinates. As defined earlier in this chapter, the masses of each of the three particles are m_A, m_B and 1.0, where the latter is the mass of the electron. The hyperspherical radius is related to the ρ_1 and ρ_2 for each Jacobi set τ by

$$\begin{aligned} R &= \sqrt{\frac{\mu_1^\alpha}{\mu}}\sqrt{\rho_{1\alpha}^2 + \frac{\mu_2^\alpha}{\mu_1^\alpha}\rho_{2\alpha}^2} = \sqrt{\frac{\mu_2^\beta}{\mu}}\sqrt{\rho_{2\beta}^2 + \frac{\mu_1^\beta}{\mu_2^\beta}\rho_{1\beta}^2} \\ &= \sqrt{\frac{\mu_2^\gamma}{\mu}}\sqrt{\rho_{2\gamma}^2 + \frac{\mu_1^\gamma}{\mu_2^\gamma}\rho_{1\gamma}^2}. \end{aligned} \tag{3.64}$$

At the matching radius R_o, ρ_1 is of the same order as ρ_2 for the α-set, but ρ_2 is much larger than ρ_1 for the two other sets. Since the ratios of the reduced masses within the square roots of eqn.(3.64) are all roughly equal to the ratio of the mass of the electron to the mass of the heavy particle for any set of Jacobi coordinates, at R_o we can approximate

$$R_o = \sqrt{\frac{\mu_1^\alpha}{\mu}}\rho_{1\alpha} = \sqrt{\frac{\mu_2^\beta}{\mu}}\rho_{2\beta} = \sqrt{\frac{\mu_2^\gamma}{\mu}}\rho_{2\gamma}. \tag{3.65}$$

By setting μ=μ_1^α, the argument of the Bessel and/or Coulomb function in the β-set coordinates, $k_\beta \rho_2^\beta$, from eqns. (3.57) and (3.65), is equal to $k_\alpha R_o$. The same is true for the argument in the γ-set coordinates. In other words, the argument in the Bessel and/or Coulomb functions for each channel calculated from the α-set coordinates does agree with the argument calculated in the β-set and γ-set coordinates. Since the adiabatic energies calculated in hyperspherical coordinates do approach the correct asymptotic energies in the dissociation limit, at least to the order of $1/R^2$ [6], it is possible to skip the two-dimensional matching all together, and obtain the $\mathcal{K}$-matrix directly within the α-set coordinates. This is called one-dimensional matching. We have tested our calculations using one-dimensional and two-dimensional matching methods, by changing the matching radius, and concluded that one-dimensional matching is adequate except at very low energies in general [2].

3.5.3 Numerical Procedures

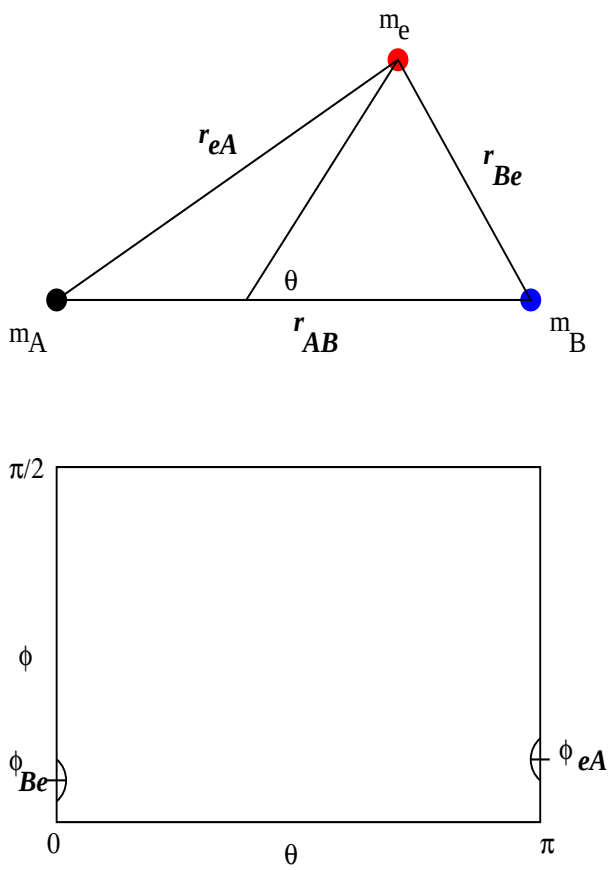

Figure 3.3: Locations of singularities in $\phi - \theta$ plane.

We have employed the two dimensional B-spline basis functions to obtain adiabatic channel functions in the adiabatic approximation. The choice of the grid distributions is customized to the nature of the channel functions which are normally concentrated in the region of small ϕ. This is clearly seen from eqn.(3.2) which shows that the range of ϕ is in the order of the square root of the mass of the electron with respect to the mass of the nuclei. Furthermore, for ion-atom collisions, if $m_A > m_B$, the attractive Coulomb singu-

larities occur at small ϕ's which are in the order of $\phi_1 = \phi_{Be} \sim 10^{-3}$ and $\phi_2 = \phi_{eA} \sim 10^{-2}$ radians, respectively. To be more specific, the singular points can be found by setting $\theta = 0 \Longrightarrow r_{Be} = 0$ and $\theta = \pi \Longrightarrow r_{eA} = 0$, which give:

$$\begin{aligned} \phi_{Be} &= \arctan\left(\frac{m_A}{m_A + m_B}\sqrt{\frac{\mu_2}{\mu 1}}\right) \\ \phi_{eA} &= \arctan\left(\frac{m_B}{m_A + m_B}\sqrt{\frac{\mu_2}{\mu 1}}\right) \end{aligned} \tag{3.66}$$

The ϕ-grids were chosen such that they are concentrated in the small-ϕ region. Specifically we distributed $\phi = [0, \pi/2]$ into four intervals, with N_1 points in [0, ϕ_1], N_2 points in [ϕ_1, $(\phi_1+\phi_2)/2$], N_3 points in $[(\phi_1 + \phi_2)/2, \phi_2]$ and N_4 points in $[\phi_2, \pi/2]$. Within each interval $[\phi_a, \phi_b]$, an exponential sequence of grid points is chosen according to

$$\phi_i = \phi_a + (\phi_b - \phi_a)\frac{e^{\gamma(i-1)} - 1}{e^{\gamma(N-1)} - 1}. \tag{3.67}$$

for $i = 1, ..., N$. In this ϕ-grid distribution, the parameters γ, N_1, N_2, N_3 and N_4 are varied for different collision systems. Only a small number of points was used for the interval $\phi = [\phi_b, \pi/2]$. Similarly, for symmetrically distributed θ-grids at θ=$\pi/2$, 60 to 70 points in the range [0, π] were used. These parameters in the grid distributions have been varied to reach at least six-digit accuracy in the eigenvalues for the R-range of interest. If necessary, different grid distributions can be employed in different ranges of R to ensure the desired accuracy.

In the SVD method, the channel functions are to be calculated at the hyperradial points dictated by the grid distributions chosen for the $\mathcal{R}$-matrix propagation. Thus, the range $[0, R_o]$ is divided into many intervals as mentioned earlier. Within each interval, the hyperradial grid points are determined by the order M of the Jacobi polynomials used in the DVR representation of the hyperradial functions. Ideally, one would like to have about 6 $\sim$ 10 points per wavelength in the hyperradial function. Such a prescription has been used in Kato and Watanabe [28] where this method was applied to the electron-atom collisions systems. A straightforward application of their procedure to ion-atom collisions is not practical. Due to the large reduced mass, the momentum as given by $\sqrt{2\mu(E - U)}$ becomes quite large even at thermal energies. Specifically for the H^+ + D(1s) system at E_{cm} = 150 eV, we would need about 5,000 points within the interval of $R = [0, 40]$, if we wish to have about 8 points per wavelength in the hyperradial function. Since the calculation of the channel function is the most time consuming part, it is clearly not

desirable. On the other hand, while the radial wave functions oscillate rapidly, all the matrix elements entering the SVD methods are slow-varying functions of the hyperradius. Thus, instead of calculating all the matrices needed in the SVD method, we obtained these matrix elements by using an interpolation procedure.

Specifically, instead of calculating the overlaps $\mathbf{S}$, $\langle\Phi_{\mu I}|h_{II\pm1}|\Phi_{\nu I\pm1}\rangle$ and $\langle\Phi_{\mu I}|T_{1b}|\Phi_{\nu I}\rangle$ matrices at all hyperradial grid points for the SVD and $\mathcal{R}$-matrix propagation, we calculated them with fewer points and then use interpolations procedure to obtain the required matrix elements for specific collision energies. In practice, we used the cubic (bicubic for 2D-interpolation of the overlaps) splines algorithm in the numerical recipes [30] to carry out the interpolation. In the present calculation we choose to interpolate only in the region where the overlaps, as functions of hyperradius, are smooth, although in principle one can interpolate near the avoided crossing region as well if more points are initially calculated in the region.

Bibliography

[1] C.D. Lin, Phys. Rep. **257**, 1 (1995)

[2] Chien-Nan Liu, Anh-Thu Le, Toru Morishita, D.B. Esry and C.D. Lin, Phys. Rev. A **67**, 052705 (2003)

[3] Anh-Thu Le, C.N. Liu and C.D. Lin, Phys. Rev. A **68**, 012705 (2003)

[4] Anh-Thu Le, M. Hesse, T. G. Lee and C.D. Lin, J. Phys. B **36**, 3281, (2003)

[5] B.H. Bransden and M.R.C McDowell, *Charge Exchange and the Theory of Ion-Atom Collision*, (Oxford: Clarendon) (1992)

[6] J.H. Macek, J. Phys. B **1**, 831, (1968)

[7] C.D. Lin and X.H. Liu, Phys. Rev. A **37**, 2749 (1988)

[8] H.R. Sadeghpour, Phys. Rev. A **43**, 5821 (1991)

[9] Yan Zhou and C.D. Lin, J. Phys. B **27**, 5065 (1994)

[10] Yan Zhou and C.D. Lin, J. Phys. B **28**, L519 (1995)

[11] L.D. Landau and E.M Lifshitz 1977 *Quantum Mechanics* 3rd Edition (Oxford: Pergamon).

[12] A. K. Bhatia and A. Temkin, Rev. Mod. Phys. **36**, 1050 (1964)

[13] C. de Boor, *A Practical Guide to Splines* (Springer, New York, 1978)

[14] H. Nakamura, Annu. Rev. Phys. Chem. **48** 293 (1997); *in Dynamics of Molecules and Chemical Reactions*, edited by R.E. Wyatt and J.Z.H Zhang (Mercel Dekker, New York, 1996), p.437

[15] H. Nakamura and C. Zhu, Comments At. Mol. Phys **32** 249 (1996)

[16] N. Shimakura and M. Kimura, Phys. Rev. A **44**, 1659 (1991)

[17] B. Zygelman, P. C. Stancil, N. J. Clarke, and D. L. Cooper, Phys. Rev. A **56**, 457 (1997)

[18] T. G. Heil, S. E. Butler and A. Dalgarno, Phys. Rev. A **23**, 1100 (1981)

[19] P. C. Stancil, B. Zygelman, N. J. Clarke, and D. L. Cooper Phys. Rev. A **55**, 1064 (1997)

[20] J.C. Light and R.B. Walker, J. Chem. Phys. **65**, 4272, (1978)

[21] Yan Zhou and C.D. Lin, Phys. Rev. Lett. **75**, 2269 (1995)

[22] Yan Zhou and C.D. Lin, J. Phys. B **28**, L519 (1995)

[23] A. Igarashi and N. Toshima, Phys. Rev. A **50**, 232 (1994)

[24] J. Tang, S. Watanabe and M. Matsuzawa, Phys. Rev. A **46**, 2437 (1992)

[25] J. C. Light, I. P. Hamilton, and J. V. Lill, J. Chem. Phys. **82**, 1400 (1985)

[26] K. Hino, A. Igarashi and J.H. Macek, Phys. Rev. A **56**, 1038 (1997)

[27] O.I. Tolstikhin, S. Watanabe and M. Matsuzawa, J. Phys. B **29**, L389 (1996)

[28] D. Kato and S. Watanabe, Phys. Rev. A **56**, 3687 (1997)

[29] O.I. Tolstikhin and H. Nakamura, J. Chem. Phys. **108**, 8899 (1998)

[30] W.H. Press, S.A. Teukolsky, W.T. Vetterling and B.P. Flannery, *Numerical Recipes in Fortran*, 2nd Edition (Cambridge University Press) (1992)

Chapter 4

Applications to Ion-Atom Collisions

In this chapter, we demonstrate the applications of the theories presented in the previous chapters. These collision-systems are selected with the aim to illustrate the close-coupling formalism can successfully describe a wide range of inelastic effects in ion-atom collisions. This chapter consists of four papers, and they are:

1. *Paper I: Evaluation of antiproton impact ionization of He atoms below 40 keV, Phys. Rev. A.*
2. *Paper II: Differential charge-transfer cross sections for* Na^+ *with Rb collisions at low energies, Phys. Rev. A.*
3. *Paper III: Helium trimer has no bound rotational excited states, J. Phys. B: At. Mol. Opt. Phys.*
4. *Paper IV: Charge transfer and excitation in slow 20 eV – 2 keV* H^+*+D(1s) collisions, submitted to J. Phys. B: At. Mol. Opt. Phys.*

4.1 Part I: Semi-Classical Approach

Paper I: Evaluation of antiproton impact ionization of He atoms below 40 keV, Phys. Rev. A.

Evaluation of antiproton-impact ionization of He atoms below 40 keV

T. G. Lee,[1] H. C. Tseng,[2] and C. D. Lin[1]
[1]*Department of Physics, Kansas State University, Manhattan, Kansas 66506-2601*
[2]*Department of Physics, Chung Yuan Christian University, Chung Li, Taiwan 32023, Republic of China*
(Received 12 October 1999; revised manuscript received 12 January 2000; published 17 May 2000)

We have performed extensive close-coupling calculations to obtain total impact ionization cross sections of He atoms by antiprotons at energies from 1 keV to 300 keV by expanding the time-dependent two-electron wave functions in terms of helium eigenstates. The stability of the calculated ionization probabilities and total ionization cross sections with respect to the choice of basis functions has been examined. Our total ionization cross sections are only slightly higher than the results from the forced-impulse approximation of Reading *et al.* [J. Phys. B **30**, L189 (1997)] but they disagree with the existing experimental data below 40 keV [Hvelplund *et al.*, J. Phys. B **27**, 925 (1994)]. We conclude that new measurements for the ionization of He by antiprotons are needed in the low-energy region.

PACS number(s): 34.50.Fa, 36.10.−k

I. INTRODUCTION

Since antiproton beams became available at CERN for atomic collision experiments in 1986, a number of measurements have been carried out at high energies (above a few hundreds keV), for example, to study the ratio of cross sections for double ionization to single ionization of atomic helium targets [1,2]. The ratios have been found to be different for proton and antiproton projectiles. Since single-ionization cross sections are expected and found to be identical for proton and antiproton impact at high energies, the measured different ratios prompt many theoretical papers to study the role of the higher-order perturbation terms and the importance of electron correlation in the double-ionization processes. At lower energies, the cross sections for single ionization by protons and by antiprotons are expected to be different. The difference is understood to be more dramatic as the collision energies are lowered [3]. For proton collisions at low energies, electron capture process is dominant and ionization is a rare event. Without the electron capture channels, ionization by antiprotons is expected to have larger cross sections, but antiproton collision experiments are much more difficult to perform because of the degrading of the beams at low energies. Nevertheless, such a pioneering experiment has been carried out by Hvelplund *et al.* [4] for antiproton energies down to about 12 keV. Their results, together with the data taken earlier at higher energies [5], are displayed in Fig. 1. Note that the two experiments agree reasonably well at energies above 50 keV.

Since the report of the experimental results, various theoretical approaches have been used to obtain the ionization cross sections for this system. Except for the so-called CDW-EIS theory [6], which is not known to be valid in the low-energy region, all the other calculations fail to agree with experimental results below 40 keV. In the theoretical calculations, however, various approximations have to be employed and one wonders if there is still something missing in the theory that is responsible for the discrepancy. In performing such calculations one may classify the approximations into three categories. First, the scattering model: is the model expected to work in the low-energy region? Second, the He wave function: are the two electrons treated on equal footing with antisymmetrized wave functions and the electron-electron interaction properly accounted for? It is not advisable to employ the independent particle approximation without checking its validity. Third, how are the ionization channels represented? Most of the existing nonperturbative methods can treat ionization in some approximations only, namely, by representing them using pseudostates. How much is the error expected in such approximations?

In this paper we have used the semiclassical impact parameter close-coupling approximation to treat the collisions of antiprotons with helium atoms by expanding the time-dependent two-electron wave function in terms of the eigenstates of helium atoms. The computer program is the general

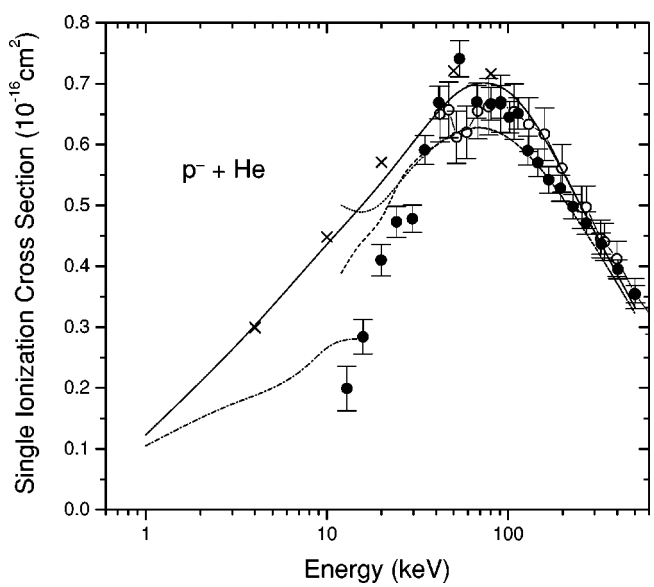

FIG. 1. Single-ionization cross sections for antiproton collisions with He. Experiments: solid circles, Hvelplund *et al.* [4]; open circles, Andersen *et al.* [5]. Theoretical results: solid line, present calculation with basis set 1; crosses: present results with basis set 2; dashed lines, multicut FIM theory [10]; dotted lines, one-cut FIM theory [10]; dash-dotted lines, multielectron hidden-crossing theory [13].

 ©2000 The American Physical Society

TABLE I. Comparison of the two sets of eigenenergies (a.u.) of He singlet states. The two sets differ primarily in the distributions of the pseudostates (for energies greater than −2.00 a.u.). Both sets of basis functions have been used in the close-coupling calculations. The experimental binding energies of He for the first few excited states are also shown.

$L=0$			$L=1$			$L=2$			$L=3$		
Set 1	Set 2	Experiment	Set 1	Set 2	Experiment	Set 1	Set 2	Experiment	Set 1	Set 2	Experiment
−2.8791	−2.8803	−2.9033	−2.1226	−2.1225	−2.1236	−2.0556	−2.0556	−2.0554	−2.0221	−2.0260	−2.0310
−2.1445	−2.1446	−2.1458	−2.0548	−2.0548	−2.0549	−2.0309	−2.0310		−2.0122	−2.0086	
−2.0608	−2.0608	−2.0160	−2.0299	−2.0303		−2.0047	−2.0114		−1.9890	−1.9984	
−2.0333	−2.0334		−2.0171	−2.0176		−1.8821	−2.0009		−1.8796	−1.9904	
−2.0209	−2.0212		−1.9861	−1.9955		−1.6749	−1.9674		−1.7803	−1.9808	
−1.9940	−2.0072		−1.9651	−1.9905		−1.3483	−1.9343		−1.2914	−1.9620	
−1.9218	−2.0029		−1.8283	−1.9879		−1.2153	−1.8751		−0.6591	−1.9192	
−1.7884	−1.9820		−1.5241	−1.9861		−0.6735	−1.8189		0.9311	−1.8801	
−1.5645	−1.9817		−1.0516	−1.9798		−0.2254	−1.6225		1.9266	1.2916	
−1.2751	−1.9291		−0.6405	−1.9714		0.5197	−0.7833				
−0.8984	−1.9273		−0.4641	−1.9162		1.0864	−0.6729				
−0.7585	−1.8956		−0.4445	−1.7475		2.8328	0.8915				
−0.5773	−1.4578		0.2480	−1.2090							
−0.0093	−0.7669		0.3348	−0.8324							
0.3044	−0.7159		0.7825	−0.4490							
0.5436	−0.5129		1.2465	0.2022							
0.6908	0.4831		1.5875	0.7121							
1.3421	0.9432		3.7802	0.9663							
			4.6755	1.9982							

two-electron two-center atomic orbital expansion code, which has been used extensively with great success in ion-atom collisions [7,8]. In applying this code to the present system, we only include the eigenstates on the helium center since there are no bound electronic states associated with the antiproton center. We used pseudostates to represent the ionization channels, and these pseudostates are centered also only on the target atom. It may be argued that it would be desirable to include some pseudostates around the antiproton to account for ''antielectron capture to the continuum.'' However, we will show that such a two-center calculation has been found not essential for the ionization of atomic hydrogen by antiprotons. Thus we expect that a similar equivalent one-center calculation be adequate for antiproton collisions with helium atoms.

In Sec. II we show calculations performed using two different basis sets and compare the total ionization cross sections obtained. The results are then compared to experimental data and with other calculations in Sec. III. By analyzing the theoretical results we believe that the discrepancy with experimental data is most likely coming from the experimental side and thus new measurements are called for when the new low-energy antiproton beams become available in the near future. Section IV gives a short summary to end this paper.

II. THEORETICAL CALCULATIONS AND BASIS SETS

We employed the semiclassical impact parameter model where the antiproton is assumed to travel on a rectilinear trajectory. Following the standard close-coupling approximation the time-dependent two-electron wave function is expanded in terms of the eigenstates of the helium atoms, the scattering amplitude to each final state is obtained by solving the resulting coupled first-order differential equations.

The complete basis set in such a calculation should consist of all the eigenstates of the He atom. They include the ground state, the singly excited states, doubly excited states, single-ionization states, ionization plus excitation states, and double-ionization states. At low energies states that have higher excitation energies are populated with much smaller probabilities, thus higher doubly excited states, excitation plus ionization states, and double-ionization states are not included in our basis set. Since the main interest is the single-ionization cross section, in the basis set we thus include the ground state, the singly excited states, and the single-ionization states that are approximated by pseudostates. Starting with primitive Slater functions for each electron with adjustable parameters, the two-electron basis functions with appropriate symmetries are constructed and used to diagonalize the two-electron Hamiltonian of the helium atom.

In Table I we show the resulting eigenenergies obtained from two different basis sets that are used in the scattering calculations. Since the total spin is considered as a good quantum number, only singlet states need to be included. For the first few bound states we also list the experimental energies for comparison [9]. Since the $L=0$ and $L=1$ states are populated mostly in the collision, efforts were made to increase the number of states in these two partial waves. For $L=2$ and $L=3$ the basis set was obtained without optimization in order to keep the total number of basis functions in

TABLE II. Comparison of the calculated total ionization probabilities from the two different basis sets used. The collisional impact parameter is fixed at $b=0.5$ a.u. The ionization probability to each partial wave L is also presented.

E (keV)	Set	$L=0$	$L=1$	$L=2$	$L=3$	Sum
4	1	0.1356	0.1149	0.0811	0.0294	0.3610
	2	0.1358	0.1396	0.0668	0.0186	0.3609
10	1	0.1518	0.1811	0.0855	0.0055	0.4238
	2	0.1603	0.1914	0.0379	0.0012	0.3908
20	1	0.1239	0.2348	0.0645	0.0079	0.4311
	2	0.1502	0.2425	0.0283	0.0021	0.4231
50	1	0.1004	0.2560	0.0497	0.0014	0.4202
	2	0.1286	0.2756	0.0195	0.0019	0.4256

the scattering calculation small. Since the binding energy of $He^+(1s)$ is -2.0 a.u., all the eigenstates with energies greater than -2.0 a.u. are pseudostates. The threshold for single ionization plus He^+ core excitation to $n=2$ is -0.5 a.u., thus the pseudostates with energies between -2.0 and -0.5 a.u. represent single-ionization channels. (Some doubly excited states exist below $E=-0.5$ a.u. They are partially excluded by choosing the orbital of one of the electrons to be close to the $1s$ of He^+.) For pseudostates with energies higher than -0.5 a.u. each pseudostate is a certain combination of single ionization, ionization plus core excitation, and double ionization. The pseudostates used were chosen not to contain such components as much as possible by forcing the inner electron orbital to represent a $He^+(1s)$ electron. This is only an approximation and it does not allow us to distinguish these channels rigorously unless careful projections are carried out. For the purpose of this work, we will present ionization cross sections as the sum of the cross sections to all pseudostates with energies higher than -2.0 a.u. This may introduce some small ambiguity in the cross sections obtained when compared to the experimental single-ionization cross sections. On the other hand, contribution of cross sections from pseudostates with energies higher than -0.5 a.u. is less than 5–10 % in the energy range considered.

A key element in determining whether the calculated total ionization cross section is stable or not is to see if the results depend on the basis set used. For this purpose we used two basis sets that have different pseudostate distributions. Another criterion is to make sure that there are more pseudostates with energies near the ionization threshold since that is the region where the ionization probability is large. The other basis set has been generated and used in the calculation but we only present complete results from these two sets since they have the better pseudostate distributions.

III. RESULTS AND DISCUSSION

In Table II we show the total ionization probabilities calculated at the fixed impact parameter $b=0.5$ a.u. at four different energies and how they are distributed among the different total orbital angular momentum states. In general the two basis sets give nearly identical partial wave contributions despite that the pseudostate distributions in each partial wave are different. Furthermore it is noticed that the total probability is even less sensitive to the two different basis sets used. The near independence of the total ionization probability with respect to the pseudostates used is essential. Thus we have confidence that the calculated cross sections are accurate to within a few percent with respect to the pseudostates used.

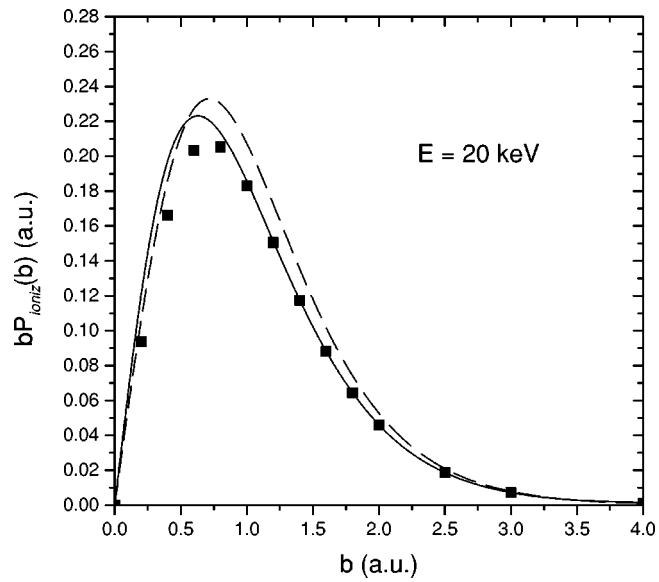

FIG. 2. Impact-parameter-weighted total ionization probability vs impact parameters for antiproton-He collisions at 20 keV. The solid line is calculated from basis set 1. Results from basis set 2 are shown as dashed lines. The squares indicated results from summing over pseudostates up to $E=0.0$ a.u. only, from basis set 1 (see text for explanation).

To assess the reliability of the calculated ionization cross sections we further show the impact-parameter-weighted total ionization probability as a function of impact parameters calculated from the two basis sets. In Fig. 2 we show the results for $E=20$ keV. Note that the difference appears to be larger at the larger impact parameters. This is traced to the fact that the higher L's are making more contributions in this energy region at larger impact parameters. In Fig. 2 we also show the weighted probabilities obtained by including pseudostates with energies from -2.0 to 0.0 a.u. only. The result would give a lower limit to the single-ionization cross section. In this approximation it is assumed that all the pseudostates with energies greater than 0.0 a.u. are double-ionization channels, which, of course, is not correct. Note that the difference is significant only at small impact parameters. This is easily understood since large energy transfer to the electron(s) occurs only in close collisions. Under this approximation, the total ionization cross section calculated is 0.538×10^{-16} cm^2, to be compared to the value 0.571×10^{-16} cm^2 obtained by summing over all the pseudostates. The difference can be used as an upper bound of the double-ionization cross sections. Since the pseudostate distributions for these higher energy states are very sparse, this estimate is probably not very accurate.

We have used the same two basis sets to calculate the

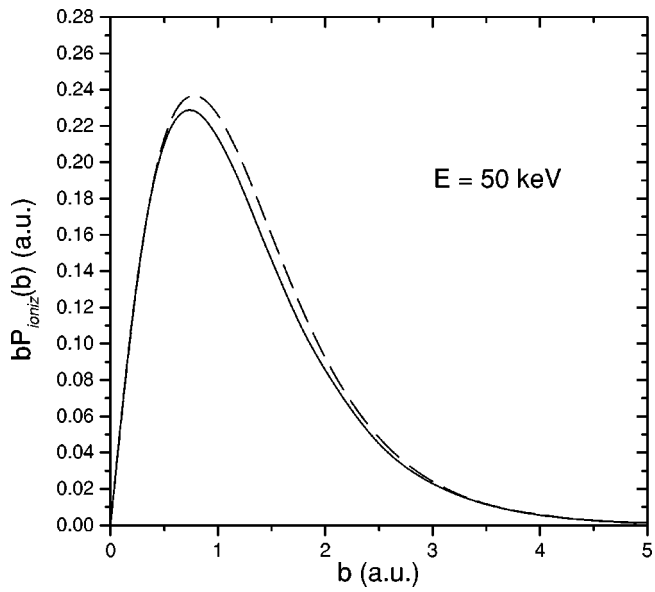

FIG. 3. Impact-parameter-weighted total ionization probability vs impact parameters for antiproton-He collisions at 50 keV. The solid line is calculated from basis set 1. Results from basis set 2 are shown as dashed lines.

ionization probabilities at $E=4$ keV and $E=50$ keV, and the resulting weighted ionization probabilities are shown in Fig. 3 and Fig. 4, respectively. Clearly we can claim that the results are relatively insensitive to the basis sets used.

We can now return to Fig. 1 to discuss the results of the present calculation in comparison with other existing calculations and experiments. For collision energies above 70 keV the experimental results of Hvelplund *et al.* [4] and of Andersen *et al.* [5] agree quite well with the results from the present calculation, which tend to agree better with the latter and the results from Reading *et al.* [10] tend to agree better with the former. However, we mention that our results in principle include some small contributions of double-ionization cross sections.

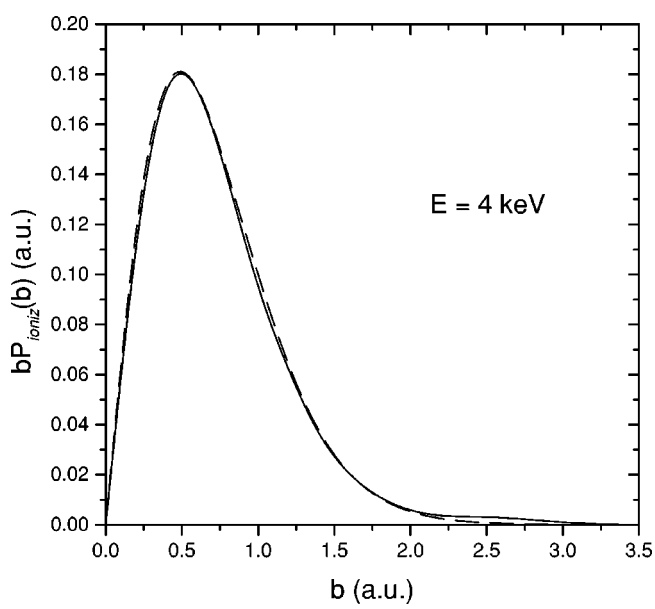

FIG. 4. Same as Fig. 3 but for $E=4$ keV.

The issue that we would like to address is the discrepancy between experiment of Hvelplund *et al.* [4] and the existing theoretical calculations at energies below 40 keV, but more notably below 20 keV. As mentioned in the Introduction, there have been many previous theoretical calculations attempting to interpret the low-energy experimental result. The only model that gives ''perfect'' agreement with the data is the CDW-EIS calculation of Fainstein *et al.* [6] (not shown). This agreement is considered to be fortuitous since the CDW-EIS model is a high-energy theory and is not known to work in the low-energy region considered here. There are other calculations [11,12] carried out within the context of the independent electron model and at higher energies; they do not address the discrepancy discussed here. Two other calculations have been made to address the ionization cross sections in this low-energy regime. One is the so-called forced-impulse approximation (FIM) of Reading *et al.* [10]. In the FIM method the two-electron wave function is propagated in time in a set of two-electron basis functions, but the electron-electron interaction is turned on at discrete time steps. In the single-cut FIM this interaction was turned on only once. In the multicut FIM the interactions were turned on up to seven times. The results from such a single-cut and multicut FIM are shown in Fig. 1. These authors showed that a single-cut FIM is not adequate, especially at lower energies, but the multicut FIM results appear to approach toward the experimental data of Hvelplund *et al.* [4], except that the experimental data show a much steeper drop with decreasing energies. Another calculation in the low-energy region is the hidden-crossing theory result of Bent *et al.* [13]. This is based on treating atomic collisions in the molecular basis but the molecular potential energy surfaces are calculated in the complex plane of the internuclear axis. Using the analytical property of the potential surface, the transition probabilities can be calculated in terms of simple contour integrals around the branch points. This method has been used extensively [14–16] to study one-electron collision systems to obtain ionization cross sections and the work of Bent *et al.* [13] is the first attempt for a two-electron system. Since the potential surface was calculated with an approximation where full configuration interaction (CI) was not included, it is not clear how to evaluate the accuracy of the reported results. Nevertheless, they are shown for comparison in Fig. 1. It must be mentioned that their results above 4 keV had been obtained by extrapolating to the region where the validity of the hidden-crossing theory is a concern.

Let us now discuss the present calculated total ionization cross sections. The results from basis set 1 are shown as a solid line, by connecting smoothly the calculated points. The actual results obtained from basis set 2 are indicated by crosses that are quite close to those from basis set 1. In comparing to the multicut FIM results of Reading *et al.*, there is a quite reasonable agreement within the energy range of 12–50 keV where the two results differ by about 10–15 %. Most importantly the energy dependence from the two calculations is essentially identical. The drop with decreasing collision energy is not as steep as indicated in the experi-

ment. We have extended the calculation down to 1 keV. For calculations at even lower energies one may need to use nonrectilinear trajectories in the semiclassical calculation. We comment that the result from the multielectron hidden-crossing theory is quite close to ours at 1 to 2 keV, though it has a different energy dependence.

Based on the results obtained from our calculation and from those of Reading *et al.*, we believe that it is appropriate to challenge the experimental ionization cross sections reported in Hvelplund *et al.* [4] at lower energies. We believe that the cross section should not drop as rapidly as reported. In view of the difficulty of performing experiments with diminishing beams at these low energies, such error in the measurement is not inconceivable. One may argue that ionization cross section is the easiest measurement that can be performed for collisions with antiprotons in any energy regime, thus the existing discrepancy certainly calls for new measurements once the new antiproton beams become available in the next year or two [17,18] before any other collision experiments are carried out.

The above conclusion is based on our estimation that the final total ionization cross sections will not be changed significantly by the approximations employed in the present calculation. In this work the electron-electron interaction is included explicitly. The main approximation would be the representation of the ionization channels with a limited number of pseudostates. We believe such an approximation would not cause large errors in the total ionization cross sections based on experience from calculations in many ion-atom collision systems. We further checked that the reported total ionization cross section is not sensitive to the pseudostates chosen. Another possible concern is the single-center basis functions used in the present calculation and the truncation of the partial waves up to $L=3$ only. Such a truncated expansion is not expected to describe fully the final state interaction between the electron and the antiproton, but such an effect will not change the total ionization cross section significantly. This speculation is drawn from the study of antiproton collisions with atomic hydrogen where many more detailed calculations have been made by various methods. To illustrate this, we present the ionization cross sections for this system from 1 to 300 keV in Fig. 5. Calculations carried out using the present single-centered expansion method are shown as a solid line, from another single-centered calculation of Hall *et al.* [19] calculations are shown as dashed lines. They are to be compared with results obtained from integrating the time-dependent Schrödinger equation on space grid points of Wells *et al.* [20] where no basis functions were employed. In our close-coupling calculations we also used up to $L=3$, and the errors is clearly within 10% of the direct numerical solution results. There are other single-centered calculations up to $L=6$ [22], but the total ionization cross sections obtained differ little from the ones we have reported here. In Fig. 5 the experimental ionization cross sections [21] have been plotted also but the data is available only at the higher energies with large errors.

As a side product, we also report the excitation cross sections to $1s2s(^1S^e)$ and $1s2p(^1P^o)$ states that are likely to be measured in future experiments. These data can be checked by other theoretical calculations as well in the future. In Fig. 6 the cross sections are plotted. The excitation cross sections calculated with basis set 2 are also shown in crosses and asterisks, for the $1s2s(^1S^e)$ and $1s2p(^1P^o)$ states, respectively. They agree well with those obtained from basis set 1. Note that these cross sections are smaller than the total ionization cross sections by a factor of 5 to 10.

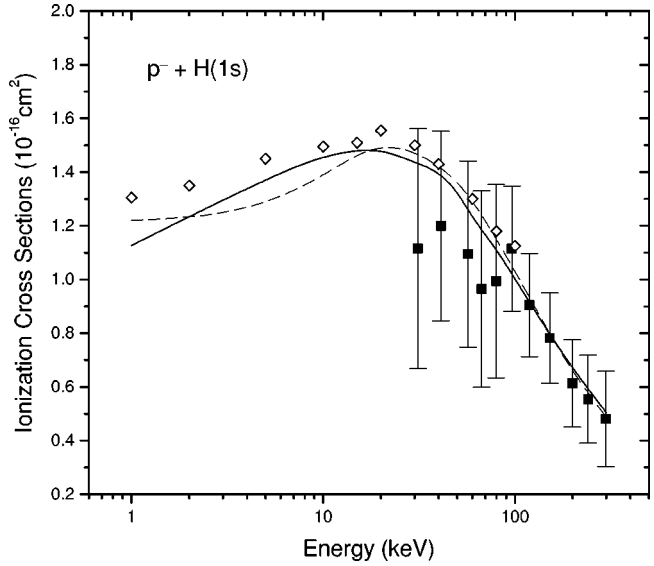

FIG. 5. Total ionization cross sections for antiprotons colliding with atomic hydrogen. Solid line: present single-center close-coupling calculation; dashed lines: single-center calculation of Hall *et al.* [19]; diamonds: direct integration of Schrödinger equation results of Wells *et al.* [20]; solid squares: the experimental results of Knudsen *et al.* [21].

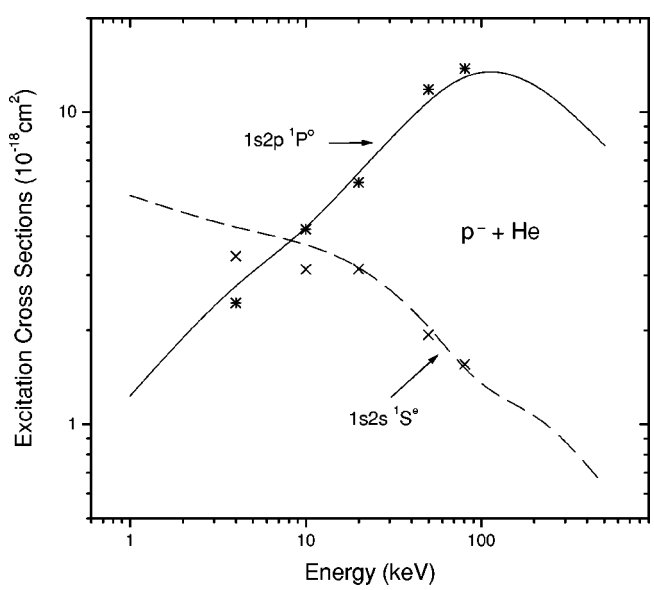

FIG. 6. Single-excitation cross sections to $1s2s$ $(^1S^e)$ and $1s2p$ $(^1P^o)$ states for antiprotons colliding with He from the present close-coupling calculations. Dashed line: $1s2s$ $(^1S^e)$ results with basis set 1; solid line: $1s2p$ $(^1P^o)$ results with basis set 1; crosses: $1s2s$ $(^1S^e)$ results with basis set 2; stars: $1s2p$ $(^1P^o)$ results with set 2.

IV. SUMMARY

In summary, we have performed a detailed calculation on the total ionization cross sections of He by antiprotons using two-electron basis functions in a close-coupling expansion method. Results from two different basis sets are shown to support the accuracy of the cross sections presented. While general agreement between theory and experiment is achieved for collision energies above 50 keV, we believe that deviations below 40 keV are likely due to the previous experimental difficulties. We have made the case to rule out that the discrepancy is due to approximations in the theoretical calculations and concluded that ionization cross sections of He by antiprotons below 40 keV should be remeasured again when the new antiproton beams become available in the next few years.

ACKNOWLEDGMENTS

This work was supported in part by the U.S. Department of Energy, Office of Science, Office of Basic Energy Sciences, Division of Chemical Sciences. H.C.T. is supported in part by the National Science Council, Taiwan.

[1] L. H. Andersen *et al.*, Phys. Rev. Lett. **57**, 2147 (1986).
[2] H. Knudsen and J. F. Reading, Phys. Rep. **212**, 203 (1992).
[3] M. Kimura and M. Inokuti, Phys. Rev. A **38**, 3801 (1988).
[4] P. Hvelplund *et al.*, J. Phys. B **27**, 925 (1994).
[5] L. H. Andersen *et al.*, Phys. Rev. A **41**, 6536 (1990).
[6] P. D. Fainstein *et al.*, J. Phys. B **21**, 2989 (1988).
[7] W. Fritsch and C. D. Lin, J. Phys. B **19**, 2683 (1988).
[8] W. Fritsch and C. D. Lin, Phys. Rep. **202**, 1 (1991).
[9] C. Moore, *Atomic Energy Levels*, Natl. Bur. Stand. (U.S.) Circ. No. 467 (U.S. GPO, Washington, D.C., 1974), Vol. I.
[10] J. F. Reading *et al.*, J. Phys. B **30**, L189 (1997).
[11] L. A. Wehrman, A. L. Ford, and J. F. Reading, J. Phys. B **29**, 5831 (1996).
[12] G. Schiwietz *et al.*, J. Phys. B **29**, 307 (1996).
[13] G. Bent, P. S. Krstic, and D. R. Schultz, J. Chem. Phys. **108**, 1459 (1998).
[14] S. Y. Ovchinnikov and E. A. Solov'ev, Comments At. Mol. Phys. **22**, 69 (1988).
[15] R. K. Janev and P. S. Krstic, Phys. Rev. A **44**, R1435 (1991).
[16] M. Pieksma and S. Y. Ovchinnikov, J. Phys. B **27**, 4573 (1994).
[17] Y. Yamazaki (private communications).
[18] H. Knudsen (private communications).
[19] K. A. Hall *et al.*, J. Phys. B **29**, 6123 (1996).
[20] J. C. Wells *et al.*, Phys. Rev. A **54**, 593 (1996).
[21] H. Knudsen *et al.*, Phys. Rev. Lett. **74**, 4627 (1995).
[22] A. Igarashi (unpublished).

4.2 Part I: Semi-Classical Approach

Paper II: Differential charge-transfer cross sections for Na^+ with Rb collisions at low energies, Phys. Rev. A.

Differential charge-transfer cross sections for Na^+ with Rb collisions at low energies

T. G. Lee,[1,*] H. Nguyen,[1] X. Flechard,[1,2] B. D. DePaola,[1] and C. D. Lin[1,*]
[1]*J. R. Macdonald Laboratory, Department of Physics, Kansas State University, Manhattan, Kansas 66506-2601*
[2]*LPC CAEN, Boulevard du Maréchal Juin, 14050 Caen Cedex, France*

(Received 1 April 2002; published 1 October 2002)

We report on a theoretical and experimental study of state-selective differential single-electron transfer cross sections between Na^+ ions and Rb($5s,5p$) atoms at collision energies of 2, 5, and 7 keV. A two-center multichannel semiclassical impact parameter close-coupling method with straight-line trajectories was used to obtain single-electron capture amplitudes. By combining with the eikonal approximation, we calculated the angular differential cross sections. These results are compared to the experimental data obtained with Rb targets cooled in a magnetic optical trap. It is shown that there is generally a good agreement between the present calculations and the experiments. In spite of the higher resolution offered from the cold target, the rapid oscillations in the differential cross sections are not resolved by the experiments.

DOI: 10.1103/PhysRevA.66.042701 PACS number(s): 34.10.+x, 34.70.+e, 34.50.Pi

I. INTRODUCTION

When an ion collides with an atom, processes such as excitation, charge exchange, and ionization can occur. For slow ion-atom collisions, a charge-transfer reaction is the dominant process. There is a considerable amount of experimental measurements and theoretical calculations on electron-transfer cross sections in collisions between singly charged ions with neutral atoms. In particular, collisions between singly charged alkali ions and neutral alkali atoms have been studied since the 1960s. However, most of these studies were carried out in a higher-energy region and the final states of the charge-transfer products were not determined.

Collisions between protons as well as alkali ions with Na targets have been investigated extensively by Andersen and co-workers in the 1990s [1] (*reference within*). The differential charge-transfer cross sections have been measured [2–7] and compared to close-coupling calculations based on the two-center atomic orbitals or on molecular orbitals [8–12]. Since the differential cross section is sharply forward peaked, the theoretical results had to be folded with experimental angular resolutions and some detailed structure was lost. In this paper, we report on the results from theoretical calculations and the comparison with experimental results obtained from the so-called magneto-optical trap and target recoil momentum spectrometer (MOTRIMS) apparatus at Kansas State University. The setup allows the determination of state-selective charge-transfer cross sections, as well as the differential cross section to each state. Specifically, we focus on the collisions of Na^+ ions with Rb, either initially in the $5s_{1/2}$ ground state or initially in the excited $5p_{3/2}$ states. Collision energies are 2, 5, and 7 keV in the laboratory frame. We will concentrate on the differential cross sections for capture to the dominant final states.

The rest of the paper is organized as follows. In Sec. II, the essentials of the MOTRIMS experiment are briefly discussed. The semiclassical close-coupling method and the parameters for modeling the collision as a one-electron system are described in Sec. III. The results of the calculated differential cross sections and the comparison with experimental data are given in Sec. IV. It is shown that the current experimental angular resolutions are still incapable of testing the oscillations predicted in the theory. A short summary is given in Sec. V. Atomic units are used throughout unless indicated otherwise.

II. EXPERIMENT

A simplified schematic of the experimental setup is shown in Fig. 1. Details of the apparatus will be presented elsewhere. Briefly, the setup consists of a magneto-optical trap (MOT) and a target recoil momentum spectrometer (TRIMS). The MOT consists of a system of diode lasers and accompanying optics, and a pair of anti-Helmholtz coils that are used to set up a magnetic-field gradient of approximately 5 G/cm. The spectrometer consists of a series of metal plates, appropriately biased to create two constant electric-field regions, followed by a field-free drift region, followed by a two-dimensional position-sensitive detector (PSD). Not shown in Fig. 1 is the vacuum chamber shared by the MOT and TRIMS. Because of the combination of the MOT and TRIMS techniques, this approach has been dubbed MOTRIMS [13].

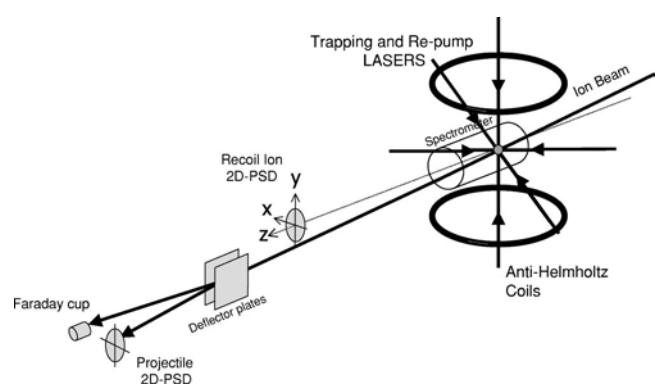

FIG. 1. Simplified schematic diagram of the experimental setup.

*Corresponding author. Email address: ltg@phys.ksu.edu/cdlin@phys.ksu.edu

 ©2002 The American Physical Society

The target temperature is typically 250 μK, as determined by the ''release-and-recapture'' method. Using a measurement technique to be described below, the total target density was determined to be approximately 1×10^{10} cm^{-3}. Background pressure in the collision chamber is typically 4×10^{-9} Torr.

Excellent reviews on TRIMS exist in the literature [14–16]. Briefly, target ions created in a collision are extracted by the two sequential electric fields, and are allowed to drift in the field-free region before striking the PSD. The spectrometer geometry and electric fields are arranged so as to minimize spread in ion time of flight (TOF) and position on the PSD due to initial position. Thus, through the TOF and final position, one may deduce the recoil ion momentum vector at the time of the collision. A key concept of the TRIMS method is that one may relate the components of the recoil ion momentum to the projectile scattering angle and the collision Q value. For single-electron capture,

$$\theta_p=\frac{p_\perp}{m_p v_p} \tag{1}$$

and

$$Q=p_\parallel v_p+\frac{1}{2}v_p^2, \tag{2}$$

where θ_p is the projectile scattering angle, $p_\perp$ and $p_\parallel$ are, respectively, the recoil momenta perpendicular and parallel to the projectile axis, v_p is the projectile velocity, m_p is the projectile mass, and Q, the collision Q value, is defined by

$$Q=E_{initial}^{binding}-E_{final}^{binding}. \tag{3}$$

In general, the TOF resolution is better than the PSD resolution. Therefore, in order to optimize the resolution in Q value, the recoil spectrometer is oriented with its extraction fields nearly parallel to the projectile axis. Thus, $p_\parallel$, and therefore the Q value, is determined by time of flight.

In general, the momentum ''kick'' given to the recoil ion is comparable to the thermal momentum spread of a room-temperature atom. Thus, for the TRIMS technique to give useful momentum information, it is necessary to cool the target. Generally this is done through the precooling and supersonic expansion of the target. Here, however, the MOT provided a target that is roughly three orders of magnitude colder than available through supersonic expansion. In this system, then, the resolution is not limited by target temperature, but by other properties of the apparatus: The $p_\parallel$ is currently limited to 0.03 a.u. by the energy spread in the projectile ion beam [17]; while $p_\perp$ is limited to 0.086 a.u. by the PSD.

In this work we report on charge transfer from both the ground and first excited states of Rb. Though the trapping and cooling process leaves some fraction of the Rb in the $5p_{3/2}$ state, it is critical to determine what this fraction is. To do this we employ a different method, described in more detail elsewhere [18], which relies on both the extremely low target temperature and the tremendous Q-value resolution inherent in the MOTRIMS technique. Briefly, the trapping laser beams are chopped with a 75% duty cycle at 50 kHz. ''Laser-on'' and ''laser-off'' Q-value spectra are then compared. Because the atoms do not move an appreciable distance during a single on-off period, the change in Rb($5s$) population is exactly equal and opposite to the change in the Rb($5p$) population. One can easily show that this allows the determination of both the ratio of the $5s$ and $5p$ populations and the ratio of capture cross sections from these states. Once the excited-state fraction has been thus measured, an accurate measurement of the target fluorescence and spatial dimension is sufficient to determine the target density. Typically, excited-state fractions of 22% were obtained. Because the day-to-day excited-state fraction could vary [19], they were measured *in situ* for each cross-section measurement presented here.

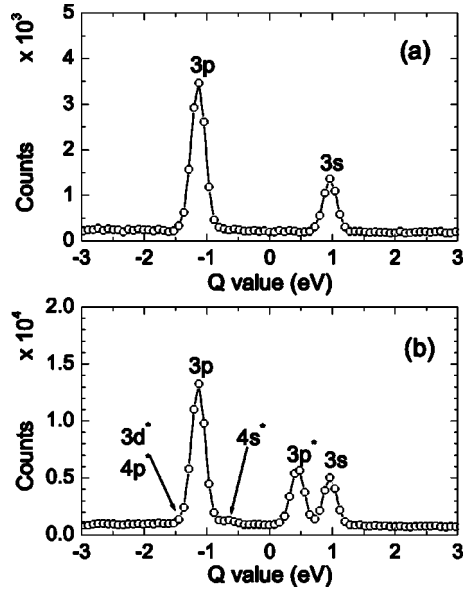

FIG. 2. Relative capture cross section versus Q value for a collision energy of 7 keV. In (a), the trapping lasers are blocked, while in (b) they are unblocked. The different channels are labeled by the final state in sodium. Asterisks indicate channels in which capture is from Rb($5p$).

Figure 2 shows an example of experimental charge-transfer cross section versus Q value, for a collision energy of 7 keV. The individual capture channels are clearly resolved. Figure 2(a) was taken when the lasers were blocked, while Fig. 2(b) was taken with the lasers unblocked. Thus, the former represents capture from the ground state only, while the latter represents capture from both ground and excited states. In comparing these two plots, the additional channels opened up through capture from Rb($5p$) are readily visible. With knowledge of the excited-state fraction, these two curves yield relative cross sections for capture, from a pure ground state and a pure excited state, into all the various final states.

In order to obtain cross-section differential in capture channel, a software gate is set on a single peak in the Q-value plot, and the corresponding PSD data are recorded. The result is integrated about the axis parallel to the beam

TABLE I. Bound-state energies of Na obtained from the model potential and the comparison with experimental data [23]. Even-tempered basis functions are used to diagonalize the atomic Hamiltonian. Energies are in atomic units.

State	Theory	Experiment
3*s*	−0.18852	−0.18886
4*s*	−0.07185	−0.07158
5*s*	−0.03748	−0.03758
6*s*	−0.01849	−0.02313
7*s*	0.09104	−0.01566
8*s*	0.53203	−0.01131
9*s*	2.41623	−0.00854
3*p*	−0.11145	−0.11154
4*p*	−0.05098	−0.05094
5*p*	−0.02902	−0.02920
6*p*	−0.00719	−0.01892
7*p*	0.10224	−0.01325
8*p*	0.70719	−0.00980
9*p*	2.19506	
3*d*	−0.05563	−0.05594
4*d*	−0.03126	−0.03144
5*d*	−0.01984	−0.02011
6*d*	0.00892	

direction; the radial position on the detector is then related to scattering cross section via Eq. (1).

III. THEORETICAL METHOD

The semiclassical close-coupling theory of atomic collisions has been described by Fritsch and Lin [20] and by Bransden and McDowell [21]. For the scattering calculation we used the same form of theory as Kuang and Lin [22]. Briefly, the time-dependent wave function is expanded in terms of bound atomic orbitals plus continuum states on each center, each with appropriate plane-wave translational factors. The atomic orbitals are expressed in terms of even-tempered basis functions

$$\phi_{nlm}=\sum_k C_{nk}N_l(\xi_k)e^{-\xi_k r}\tilde{Y}_{lm}(r), \tag{4}$$

where $\tilde{Y}_{lm}(r)$ consists of a spherical harmonic multiplied by r^l; $N_l(\xi_k)$ is a normalization constant, and the orbital exponents ξ_k are taken to form a geometric sequence

$$\xi_k=\alpha\beta^k \quad (k=1,2,\ldots,N). \tag{5}$$

Two parameters α and β can be determined by energy minimization. For low-energy alkali ion-atom collision, only the outer electron is active in the charge-transfer process. The Rb and Na are each treated as a one-electron system with the core being frozen. The active electron in each atom is governed by a model potential:

$$V_{Na}(r)=-\frac{1}{r}[1+(10+17.9635r)e^{-3.5927r}], \tag{6}$$

TABLE II. Same as in Table I, except for atomic Rb.

State	Theory	Experiment
5*s*	−0.15071	−0.15351
6*s*	−0.06215	−0.06177
7*s*	−0.03320	−0.03362
8*s*	−0.01959	−0.02116
9*s*	−0.01227	−0.01454
10*s*	−0.00828	−0.01061
11*s*	−0.00530	−0.00808
12*s*	−0.00306	
13*s*	−0.00162	
14*s*	0.30795	
15*s*	1.81277	
5*p*	−0.10272	−0.09541
6*p*	−0.04800	−0.04520
7*p*	−0.02770	−0.02657
8*p*	−0.01713	−0.01752
9*p*	−0.01024	−0.01242
10*p*	−0.00579	
11*p*	−0.00305	
12*p*	0.04485	
13*p*	0.66372	
5*d*	−0.03360	−0.03640
6*d*	−0.02111	−0.02279

$$V_{Rb}(r)=-\frac{1}{r}[1+(36-1.975r)e^{-2.34113r}]. \tag{7}$$

The parameters in these model potentials are chosen such that the experimental binding energies of the first few states of interest are well reproduced. In fitting the potential parameters, the wave functions are calculated numerically. Once the potential is chosen, we then make sure that the atomic orbitals are adequately represented by combinations of even-tempered functions, with properly adjusted α and β parameters.

In the present close-coupling calculations with atomic orbitals on the two collision centers, we have a set of 33 atomic states with $l\leqslant 2$ in the Na center. Similarly, a set of 35 atomic states with $l\leqslant 2$ is used for the Rb target. In order to assure the size of the basis set used is adequate for converged results, we have checked the state-selective capture probabilities with a larger basis set (i.e., $l\leqslant 3$) for a few impact parameters and found that the difference between the two sets calculation is about 1–3 %, and thus this will not significantly alter the results of our calculations.

Tables I and II show the energies of the bound and pseudocontinuum states of Na and Rb, respectively, used in the close-coupling calculation. For the bound states, the binding energies obtained from the model potentials are also compared to the experimental values [23]. The pseudostates are used in the basis set to help describing the distortion of the electronic orbitals at smaller internuclear separations. For the three collision energies dealt with here, the charge-

transfer amplitudes oscillate rapidly with impact parameters. To ensure good convergence in the differential and total charge-transfer cross sections, we calculated up to 203 impact parameters. For each impact parameter, the coupled equations from the close-coupling approximation are integrated from $\nu t = -200$ to $+250$ a.u. We consider collisions with Rb initially in the ground state, as well as in the $5p$ state.

To obtain the differential cross sections, we employ the eikonal approximation [21]. The angle-differential cross section (DCS) for an inelastic transition from an initial state i to a final state f can be written as the absolute square of a scattering amplitude A_{fi} at a given angle θ,

$$\frac{d\sigma_{fi}}{d\theta} = 2\pi \sin\theta |A_{fi}|^2, \tag{8}$$

where the scattering amplitudes A_{fi} are determined in turn from the impact-parameter-dependent transition amplitudes, and are given by

$$A_{fi}(\theta) = \gamma \int_0^{+\infty} bF(b)dbJ_{|m_f - m_i|}\left(2b\mu\nu \sin\frac{\theta}{2}\right). \tag{9}$$

Here

$$F(b) = C_{fi}(b, +\infty)e^{2(i/\nu)Z_T Z_P \ln b}, \tag{10}$$

with $\gamma = \mu\nu(-i)^{|m_f - m_i|+1}$, μ the reduced mass, ν the relative collision velocity, and m_f (m_i) the magnetic quantum number of the final (initial) state. The function J denotes a Bessel function of the first kind and C_{fi} is the semiclassical transition amplitude, evaluated for a given impact parameter b. The additional phase $e^{2(i/\nu)Z_T Z_P \ln b}$ is the eikonal phase due to the Coulomb repulsion between the two nuclei and Z_T (Z_P) is the effective charge of the target (projectile) that defines the Coulomb trajectory of the two colliding nuclei. Since charge-transfer occurs far outside the core of both atomic ions, an effective charge of 1 was used for each.

The numerical evaluation of the diffraction integral (9) should be done carefully since it involves rapidly oscillating integrands. We divide the range of impact parameters into small sectors, and within each sector the integrand is expressed as $F(b)\exp(i\omega \ln b)$. The evaluation of the integral over the sector is done by substituting $x = \ln b$ and rewriting the integral to be in the form of

$$\int_{x_n}^{x_{n+1}} (ax^2 + bx + c)\exp(iwx)dx, \tag{11}$$

where we have fitted the function $F(b)$ within the sector by a quadratic function. The integration over this sector can then be performed analytically. For a converged result, it is essential to ensure that within each sector the function $F(b)$ is well behaved with respect to $x = \ln b$. The accuracy of this algorithm can be checked by varying the size of the sectors or by using another algorithm, such as the Simpson rule. We further check that the total cross sections obtained by integrating DCS over scattering angles and by integrating electron-capture probabilities over impact parameters are identical.

IV. RESULTS AND DISCUSSION

In this section, we present the calculated differential cross sections for various final states and compare these to the experimental measurements by folding the calculated cross sections with the experimental angular resolution. We also provide impact-parameter weighted probabilities and the unconvoluted DCS to show that the current experimental resolution is insufficient to confirm the predicted oscillatory structures. Both scattering angles and differential cross sections are referenced to the laboratory frame.

A. $Na^+ + Rb(5s)$

For collision energies of 2, 5, and 7 keV, the two dominant charge-transfer channels in $Na^+ + Rb(5s)$ collisions are into $Na(3s)$ and $Na(3p)$ states. The total charge-transfer cross section for each state was obtained from

$$\sigma_{nl} = 2\pi \sum_m \int_0^{+\infty} bdb|C_{fi}(b, +\infty)|^2. \tag{12}$$

From Table III, we see that in this energy range, capture to $3p$ dominates over $3s$. All the other channels are much weaker and are not observed in the experiment except at the highest collision energy where capture to $Na(3d)$ represents only a few percent of the total measured cross section. The fact that these are the two dominant channels can be understood from the degree of inelasticity for each transition. In Fig. 3, the energy levels of the collision system are shown. For $Rb(5s) \rightarrow Na(3s)$, the transition is exoergic process with a Q value of $+0.0354$ a.u., whereas for $Rb(5s) \rightarrow Na(3p)$, the process is endoergic, with $Q = -0.0419$ a.u. From the asymptotic energy levels, it would appear that the dominant transition would be to the $Na(3s)$ state, which not what is observed either experimentally or from the theoretical calculations.

A proper framework to understand the calculated results is best if based on the molecular potential curves. In the atomic orbitals close coupling (AOCC) approach, such curves are not calculated. Based on the model potentials (6) and (7), we have calculated the adiabatic potential curves of $NaRb^+$, and the results are shown in Fig. 4. These curves are very similar

TABLE III. Theoretical integral cross sections (10^{-16} cm^2) for charge transfer from ground-state $Rb(5s)$ to final states. The third line shows the comparison between theory and experiment of the capture cross-section ratio $Na(3s)/Na(3p)$.

Final state	$E = 2$ keV	$E = 5$ keV	$E = 7$ keV
$Na(3s)$	1.06	6.02	8.41
$Na(3p)$	19.16	20.59	22.35
Theory	0.055	0.292	0.376
MOTRIMS	0.020 ± 0.005	0.250 ± 0.032	0.271 ± 0.015

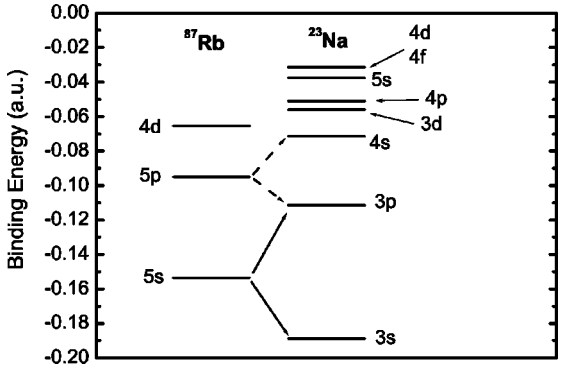

FIG. 3. Energy levels of ^{87}Rb and ^{23}Na atoms.

to those calculated by Melius and Goddard [8] for the $Li^+ + Na$ system. From these curves, it is clear that transition to Na($3s$) from Rb($5s$) is dictated by the radial coupling between the two Σ states, which show an avoided crossing near $R=13$ a.u. For the transition to Na($3p$), there are two possibilities. A radial coupling between two Σ curves would populate the $3p_0$ final state, while a rotational coupling between Σ and Π states would populate the $3p_1$ final state. For the latter, the two curves cross near $R=6$ a.u., and this crossing is an efficient mechanism for populating the Na($3p$) state at low energies. In fact, the calculated electron-capture probability [see Fig. 7(b)] for the $3p_1$ substate does indeed peak near 6.0 a.u.

We now examine the differential cross sections for these two dominant channels; see Fig. 5. In order to compare with the MOTRIMS measurements, we performed a Gaussian convolution on the theoretical results with an angular resolution of 73.64, 87.2, and 138.0 μrad for 7, 5 and 2 keV, respectively. The experimental results are normalized to the theoretical predictions at the peak for easy comparison.

From Fig. 5(b), it is clear that there is an excellent agreement between theory and experiment for the dominant Rb($5s$)$\rightarrow$Na($3p$) channel. For the weaker Na($3s$) channel, the agreement is quite good at 7 keV, but significant deviations can be seen at 2 keV. At this energy, the total cross section to $3s$ is only about 5% of the capture to $3p$. The smaller cross section is reflected in the larger errors in the theoretical DCS, and the increased experimental uncertainty that is dominated by counting statistics.

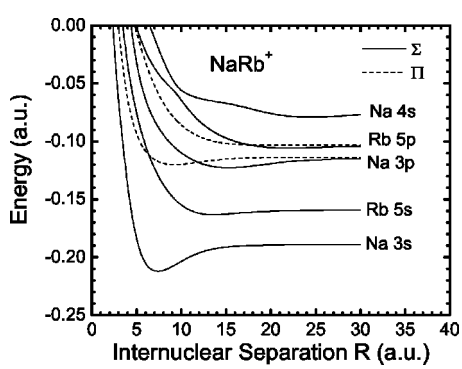

FIG. 4. Adiabatic potential curves for the $NaRb^+$ molecule.

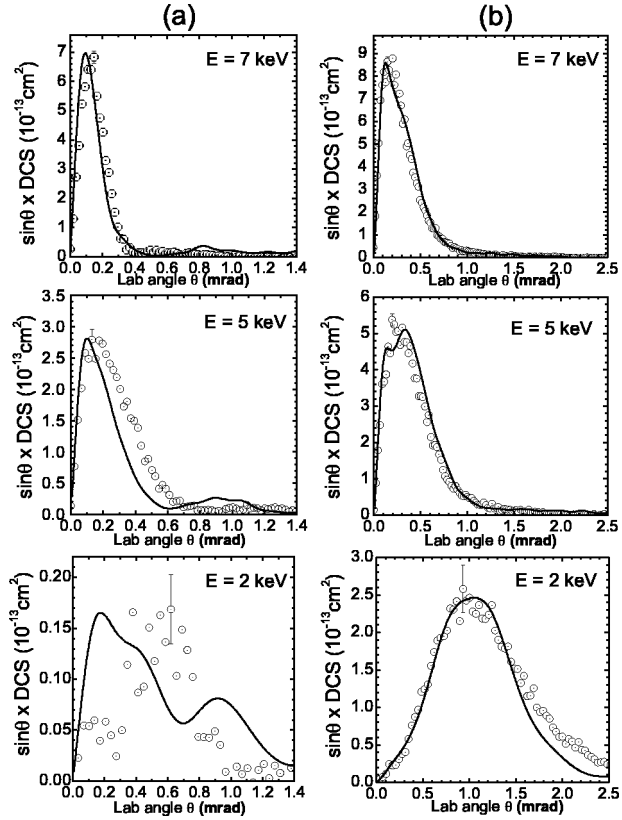

FIG. 5. (a) $\sin\theta\times$DCS as functions of laboratory scattering angle θ for Rb($5s$)-Na($3s$) at impact energies from 7 to 2 keV. The $\odot$ represents the MOTRIMS data and solid line denotes theoretical calculations folded with experimental angular resolution. The experimental results have been normalized to the theoretical data. (b) is the same as (a), except for Rb($5s$)$\rightarrow$Na($3p$) channel. Note the difference in the angular scale.

Another observation is that the DCS for capture to $3s$ is peaked at smaller angles, reflecting the fact that capture occurs at larger impact parameters. In contrast, capture to $3p$ occurs at larger scattering angles, reflecting the efficient rotational coupling at internuclear distance at about 6 a.u.

The DCS in Fig. 5 for different energies can be put on the same graph if we plot the DCS against $E\theta$. This is done in Fig. 6(a) for the experimental data for capture to the dominant $3p$ channel. In Fig. 6(b), the same data from the theoretical calculations without convolution are presented. It is clearly seen that the predicted DCS show many oscillations with respect to the scattering angle. Such oscillations are expected for collisions at low energies. Unfortunately, limitations in the angular resolution of the current MOTRIMS apparatus make the observation of such oscillations impossible.

In Fig. 7, we illustrate the interplay between the calculated impact-parameter-dependent electron-capture probabilities and the differential cross sections for the Rb($5s$)-Na($3p$) transition. We also show the dependence on the magnetic quantum number. The dominant contribution

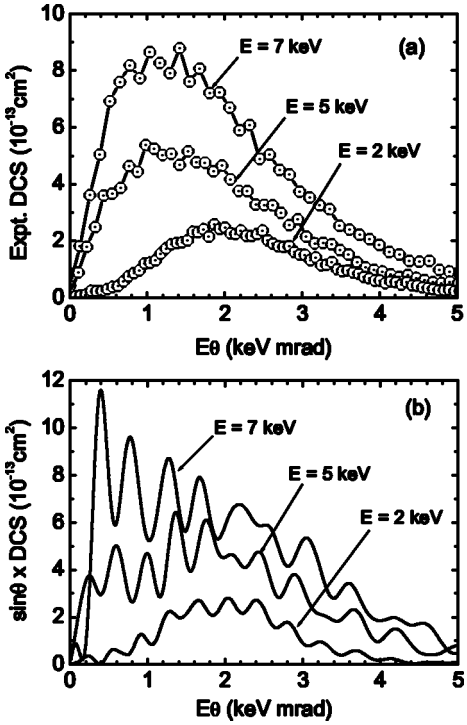

FIG. 6. (a) Experimental DCS as functions of scaled laboratory scattering angle $E\theta$ for Rb($5s$)-Na($3p$) at impact energies from 7 to 2 keV. Experimental data are normalized to the TCAOCC calculations. (b) is the same as (a) except that these are the results from TCAOCC calculations.

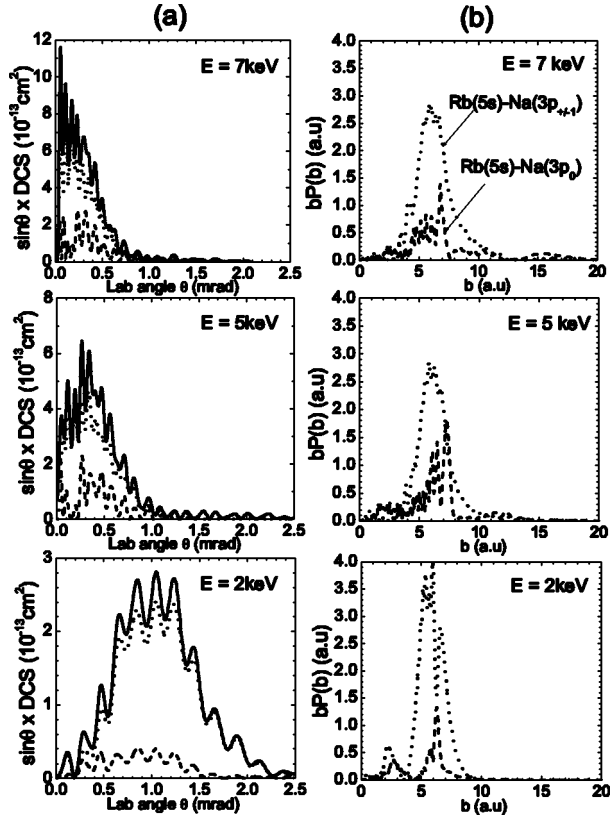

FIG. 7. (a) Theoretical sin θ-weighted DCS as functions of scattering angle θ of charge transfer for Rb($5s$)$\rightarrow$Na($3p$) for impact energies of 7–2 keV. The dotted line and dashed line denotes capture to Na($3p_{\pm 1}$) and Na($3p_0$), respectively. The solid line represents the total DCS. (b) The corresponding impact-parameter b-weighted probabilities as functions of b.

from the rotational coupling near $R=6$ a.u. is quite clear from the impact-parameter-dependent probabilities, but not as clear from the differential cross sections.

B. Na^++Rb($5p$)

For collisions of Na^+ with the excited Rb($5p$) states at energies of 2, 5, and 7 keV, the dominant processes are electron capture to the $3p$ and $4s$ states. This can be anticipated from the energy-level diagram, Fig. 3, as well as from the potential curves in Fig. 4. The calculated total cross sections are listed in Table IV. In these calculations, the initial $5p$ state is assumed to be randomly oriented, and the magnetic substates are distributed statistically, since the lasers are incident from three orthogonal directions. The total cross section for the dominant $3p$ channel is very large, reflecting electron capture occurring at large impact parameters. For the weaker channel, i.e., electron capture to the $4s$ state, the calculated total cross section has a minimum at 5 keV. In Table IV, we also present the cross-section ratio for $4s$ with respect to $3p$, and compare the results with the experimental measurement. The agreement is quite good except at 5 keV, where the calculated result is outside the measured uncertainty.

First we anticipate the mechanism for the capture of a Rb($5p$) electron to Na($3p$) and Na($4s$) in terms of the potential curves of Fig. 4. Radial coupling will take an initial Rb($5p_0$) to Na($3p_0$), and the rotational coupling will take it to Na($3p_1$). The rotational coupling is weak since there is no curve crossing. Thus the radial coupling, which has a slightly avoided crossing at large R near 22 a.u., is expected to be the dominant one. Similarly, if the initial state is Rb($5p_1$), the radial coupling will take it to Na($3p_1$), and the rotational coupling will take it to Na($3p_0$). Again, the radial coupling is expected to dominate, and there is a weak avoided crossing between the two Π curves at R near 15 a.u. We thus expect transition to Na($3p$) to be quite large and to occur at large impact parameters. For transition to Na($4s$), the energy gap at large R is more, thus transitions at larger impact parameters would be smaller, especially when the collision energy is decreased. At the lower energies, the avoided crossing

TABLE IV. Theoretical integral cross sections (10^{-16} cm^2) for charge transfer from Rb($5p$) to final states. The third line shows the comparison between theory and experiment of the capture cross-section ratio Na($4s$)/Na($3p$)

Final state	$E=2$ keV	$E=5$ keV	$E=7$ keV
Na($4s$)	10.39	5.03	8.92
Na($3p$)	94.20	132.82	129.10
Theory	0.110	0.038	0.069
MOTRIMS	0.128 ± 0.053	0.072 ± 0.009	0.080 ± 0.011

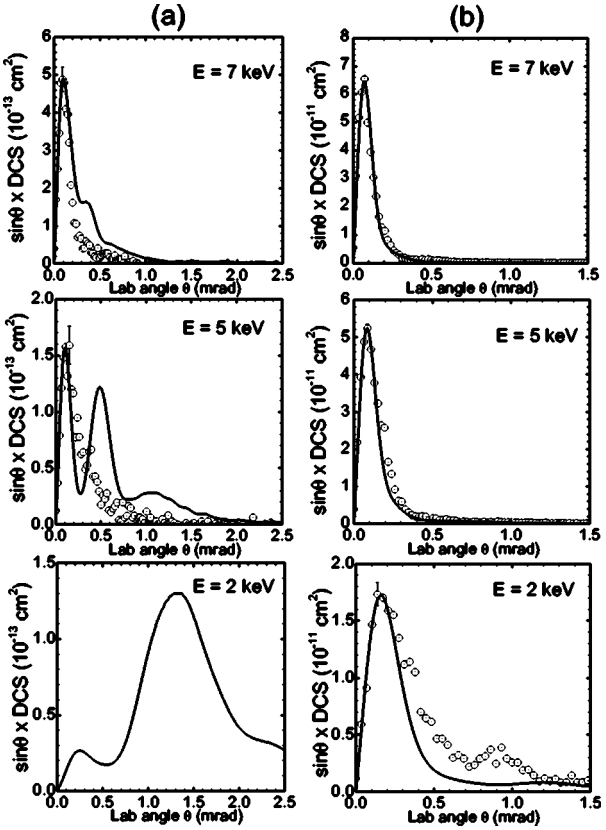

FIG. 8. (a) Same as Fig. 5 but for charge-transfer from Rb($5p$) to Na($4s$). Solid line denotes the TCAOCC and ⊙ represents the experimental data. (b) is the same as (a), except for Rb($5p$) →Na($3p$) channel.

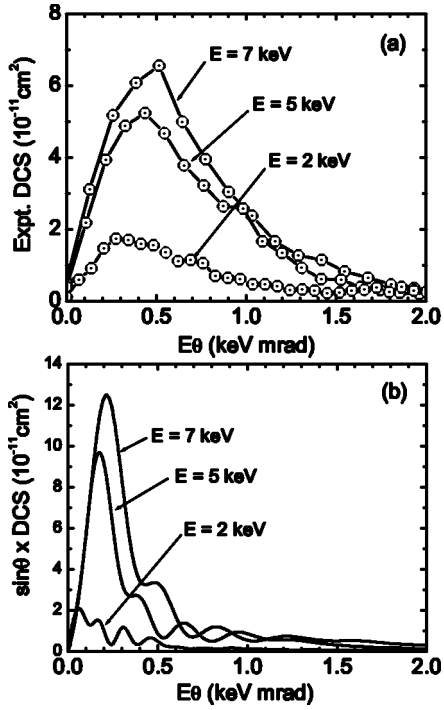

FIG. 9. Same as Fig. 6 but for charge transfer from Rb($5p$) to Rb($3p$).

between the two Σ curves at R near 9 a.u. should be more efficient in populating the Na($4s$) state. In the following, we show that this qualitative interpretation is consistent with the calculated electron-capture probabilities.

In Fig. 8, the theoretical differential cross sections, after they have been convoluted with the experimental resolution, are compared to the measured cross sections. For Rb($5p$) →Na($3p$), the theoretical DCS agrees perfectly with the experimental measurement at 7 keV. At 5 keV, there is only a minor discrepancy. At 2 keV, the experimental DCS at larger angles is greater than what theory predicts. For the weak channel [i.e., Rb($5p$)→Na($4s$)], the overall agreement is less satisfactory. At 7 keV, the agreement at small angles is quite good, but the theory shows a shoulder at the higher energies. At 5 keV, the agreement between theory and experiment is only fair, and it appears that the shoulder at 7 keV becomes a pronounced peak at 5 keV. At 2 keV, the experimental signal is too weak to extract useful information, but the shoulder from theory at 7 keV appears to the major peak. We interpret this structure as being due to the avoided crossing of the two Σ curves. At 7 keV, the transition is dominated by the coupling at large R, thus the DCS is rather forward peaked. As the energy is decreased, the system evolves more adiabatically and probabilities for transitions at large R decrease. At 2 keV, transitions at large R become insignificant, and the major mechanism for transition occurs at the avoided crossing near $R=9$ a.u. The calculated electron-capture probabilities to Na($4s$) (not shown) indeed demonstrate this behavior, which can also be seen from the theoretical differential cross sections in Fig. 8(a). The mechanism also explains the minimum of the total cross section to Na($4s$) at 5 keV. Above this energy, transitions occur mostly at large impact parameters. Below this energy, the Landau-Zener-type transition near $R=9$ a.u. becomes more efficient such that the cross section increases with decreasing collision velocity. This interpretation is consistent with the calculated total cross sections and the differential cross sections.

In Fig. 9 we compare the DCS versus $E\theta$ for the three collision energies for the Rb($5p$)-Na($4p$) transition. On the top frame the experimental results are shown. On the bottom frame, the theoretical results without the convolution with angular resolution are shown. Apparently, the calculated angular distributions are peaked much more in the forward angles than the experimental measurements. Until the experimental angular resolution is improved to the point of being able to resolve the predicted rapid oscillations in DCS, the predicted propensity for forward peaking cannot be stringently tested.

V. SUMMARY

In summary, we have used the combination of two-center atomic-orbital close-coupling method and eikonal approximation to perform a detailed calculation on the charge-transfer differential cross section of Na^+-Rb collision at im-

pact energies of 2, 5, and 7 keV. We have shown that the theoretical results agree extremely well with experiments for the dominant charge-transfer channels. However, for the weak channels, the agreement is less satisfactory. This discrepancy may indicate a sign of failure both in theory and experiment, in obtaining accurate results for the weak channels. We have also shown that the present MOTRIMS results are still unable to test the oscillatory structures predicted for the DCS, in particular, for transitions from excited initial states. However, an improvement of the experimental resolution is in progress, and it is hoped that a more precise measurement will display these oscillations.

ACKNOWLEDGMENTS

This work was supported by the Chemical Sciences, Geosciences and Biosciences Division, Office of Basic Energy Sciences, Office of Science, the U.S. Department of Energy. T.G.L. wishes to thank Dr. Brett Esry for providing the code to calculate the MO potential curves.

[1] D. Dowek, I. Reiser, S. Grego, N. Andersen, A. Dubois, J.C. Houver, S.E. Nielsen, C. Richter, J. Salgado, A. Svensson, and J.W. Thomsen, J. Phys. B **35**, 705 (2002).
[2] J. Perel, R.H. Vernon, and H.L. Daley, Phys. Rev. **138**, A937 (1965).
[3] V. Aquilanti and G. Bellu, J. Chem. Phys. **61**, 1618 (1974).
[4] F. von Busch, J. Hormes, and H. Liesen, Chem. Phys. Lett. **34**, 244 (1975).
[5] R.W.V. Resandt, C. de Vreugd, R. Champion, and J. Los, Chem. Phys. **29**, 151 (1978).
[6] T. Okamoto, Y. Sato, N. Shimakura, and H. Inouye, J. Phys. B **14**, 2379 (1981).
[7] M. van der Poel, C.V. Nielsen, M.A. Gearba, and N. Andersen, Phys. Rev. Lett. **87**, 123201 (2001).
[8] C.F. Melius and W.A. Goddard, Jr., Phys. Rev. A **10**, 1541 (1974).
[9] A. Dubious, S.E. Nielsen, and J.P. Hansen, J. Phys. B **26**, 705 (1993).
[10] S. Nielsen, J.P. Hansen, and A. Dubious, J. Phys. B **28**, 5295 (1993).
[11] M. Machholm, E. Lewartowski, and C. Courbin, J. Phys. B **27**, 4681 (1994).
[12] M. Machholm and C. Courbin, J. Phys. B **29**, 1079 (1996).
[13] X. Flechard, H. Nguyen, E. Wells, I. Ben-Itzhak, and B.D. DePaola, Phys. Rev. Lett. **87**, 123203 (2001).
[14] J. Ullrich, R. Moshammer, R. Dörner, O. Jagutzki, V. Mergel, H. Schmidt-Böcking, and L. Spielberger, J. Phys. B **30**, 2917 (1997).
[15] R. Dörner, V. Mergel, O. Jagutzki, L. Spielberger, J. Ullrich, R. Moshammer, and H. Schmidt-Böcking, Phys. Rep. **330**, 95 (2000).
[16] R. Moshammer, M. Unverzagt, W. Schmitt, J. Ullrich, and H. Schmidt-Böcking, Nucl. Instrum. Methods Phys. Res. B **108**, 425 (1996).
[17] An ion-beam energy spread of 1 eV out of 6 keV is sufficient to limit the *Q*-value resolution to the observed value.
[18] X. Flechard, H. Nguyen, S.R. Lundeen, M. Stauffer, H.A. Camp, C.W. Fehrenbach, and B.D. DePaola, Phys. Rev. Lett. (to be published).
[19] The excited-state fraction in a MOT has until now, not been easy to characterize. It is known, however, to depend on the detuning and power of the trapping laser, as well as on the alignment of the six laser beams comprising the MOT. Clear characterization of the excited-state fraction in a MOT will be the subject of future work.
[20] W. Fritsch and C.D. Lin, Phys. Rep. **202**, 1 (1991).
[21] B.H. Bransden and M.R.C. McDowell, *Charge Exchange and Theory of Ion-Atom Collisions*, The International Series of Monographs on Physics Vol. 82 (Clarendon, Oxford, 1992).
[22] Jiyun Kuang and C.D. Lin, J. Phys. B **29**, 1207 (1996).
[23] C.E. Moore, *Atomic Energy Levels* (National Bureau of Standards, Washington, D.C., 1971), Vols. I and II.

4.3 Part II: Quantum Mechanical Approach

Paper III: Helium trimer has no bound rotational excited states, J. Phys. B: At. Mol. Opt. Phys.

J. Phys. B: At. Mol. Opt. Phys. **34** (2001) L203–L210 www.iop.org/Journals/jb PII: S0953-4075(01)19609-4

LETTER TO THE EDITOR

The helium trimer has no bound rotational excited states

T G Lee, B D Esry, Bing-Cong Gou[1] and C D Lin

Department of Physics, Cardwell Hall, Kansas State University, Manhattan, KS 66506, USA

Received 29 November 2000, in final form 14 February 2001

Abstract
We have searched for bound states of helium trimers with nonzero angular momenta. Including only pair interactions between helium atoms, we solved the Schrödinger equation in hyperspherical coordinates in the adiabatic approximation. From the resulting potential curves—which are mostly repulsive for nonzero angular momenta—we conclude that there are no bound rotational excited states in any of the isotopes of the helium trimer. The symmetry properties of the trimer wavefunctions in the body-fixed frame are also analysed.

In recent years the properties of very weakly bound small ^{4}He clusters have been examined in a variety of studies, both theoretical [1–6] and experimental [7–10]. To set the energy scale for these systems, the ^{4}He dimer is bound by only about 1.3 mK. For the $^4He_3$ trimer, extensive calculations [1] have shown that there are two bound states with binding energies of about 105 and 0.808 mK. The excited state has been shown [1, 3] to have properties characteristic of an Efimov state where the binding energy is exponentially small and the size is exponentially large with respect to a two-body potential parameter such as the scattering length. Practically all the calculations that have been carried out for helium trimers have dealt with states of zero total angular momentum, $J = 0$. Since there are two bound states for $J = 0$, it has been speculated [6] that there may exist bound states for nonzero angular momenta and that these states may exhibit properties of Efimov states as well. In fact, based on the rigid-rotor model, an estimate of the rotational energy using parameters from the $^4He_3$ ground state suggests that a state with one unit of angular momentum is close to being bound. Such a simple estimate, however, can be grossly in error since quantum statistics are not accounted for in such a perturbative estimate. The behaviour of few-body quantum systems is actually severely constrained by the symmetries imposed by quantum statistics [11].

In this letter we report the results of a search for the bound states of helium trimers with nonzero angular momenta. Both $^4He_3$ and $^4He_2{}^3$He are examined to investigate the effect of quantum statistics on the calculated energies. We conclude that in both systems there are no

[1] Permanent address: Department of Applied Physics, Beijing Institute of Technology, Beijing 100081, People's Republic of China.

bound states for nonzero angular momenta. Thus, the only bound states for $^4He_3$ are the two $J = 0$ states, and the only bound state for $^4He_2{}^3He$ is the $J = 0$ ground state.

The calculations were performed using hyperspherical coordinates. Let $\vec{\rho}_1$ be the vector connecting particle 1 to 2, and $\vec{\rho}_2$ the vector from the centre of mass of 1 and 2 to particle 3. For $^4He_2{}^3He$, the two identical particles are designated as 1 and 2. The mass-weighted hyperspherical coordinates are defined by

$$\mu R^2 = \mu_1 \rho_1^2 + \mu_2 \rho_2^2$$
$$\tan\phi = \sqrt{\frac{\mu_2}{\mu_1}}\frac{\rho_2}{\rho_1}.$$

We further define the angle between $\vec{\rho}_1$ and $\vec{\rho}_2$ to be θ. In the equation above, μ_1 is the reduced mass of particles 1 and 2, and μ_2 is the reduced mass of particles (1 + 2) and 3. In this letter we choose the scaling factor $\mu = \sqrt{\mu_1\mu_2}$; the mass of ^{4}He is 7296.2994 au, and the mass of ^{3}He is 5497.8852 au. Atomic units are used unless otherwise specified.

We solve the Schrödinger equation in the adiabatic representation

$$\psi(R, \phi, \theta, \omega) = \sum_\nu F_\nu(R)\Phi_\nu(R; \phi, \theta, \omega),$$

where ω is the set of Euler angles that defines the body frame with respect to the laboratory-fixed frame. We choose the body-frame z'-axis to be along $\vec{\rho}_1$, and the y'-axis to be perpendicular to the plane of the three particles. The x'-axis lies in the plane such that (x', y', z') forms an orthogonal set of axes. In the adiabatic approach, R is treated as a fixed parameter, and the adiabatic potential curves are obtained by solving

$$\left(\frac{\Lambda^2 - \frac{1}{4}}{2\mu R^2} + V\right)\Phi_\nu(R; \phi, \theta, \omega) = U_\nu(R)\Phi_\nu(R; \phi, \theta, \omega). \tag{1}$$

The explicit form of the grand angular momentum operator Λ^2 is given elsewhere [12], and $V = V_{12} + V_{23} + V_{31}$ where V_{ij} is the pair interaction between particles i and j, taken from Aziz and Slaman [13] (in their paper, this potential is designated LM2M2 with add-on). For a state with angular momentum J and parity π, we expand the channel function as

$$\Phi_\nu^{JM\pi}(R; \phi, \theta, \omega) = \sum_I \bar{D}_{IM}^{J\pi}(\omega)\psi_{I\nu}(R; \theta, \phi)$$

where $I(M)$ is the projection of J on the body-fixed (laboratory-fixed) quantization axis and $\bar{D}_{IM}^{J\pi}(\omega)$ is the symmetrized D-function. In the following we will call $\psi_{I\nu}(R; \theta, \phi)$ the Ith rotational component wavefunction. This expansion allows equation (1) to be reduced to a set of coupled equations in the two variables (ϕ, θ), which we solve using the B-spline method.

In figure 1 we show the potential curves for $^4He_3$ obtained for $(J^\pi) = (0^+, 1^+, 1^-, 2^+, 2^-, 3^+, 3^-)$. For 0^+, the potential curve is identical to the one obtained by Esry *et al* [1]. By solving the hyper-radial equation with this potential (but including the diagonal correction term $-\frac{1}{2\mu}\langle\Phi_\nu(R)|\mathrm{d}^2/\mathrm{d}R^2|\Phi_\nu(R)\rangle$), two 0^+ bound states were obtained by Esry *et al* [1] at -105 and -0.808 mK with respect to the dimer threshold, in general agreement with other calculations. From figure 1 we note that the potential curves for other values of J^π are all repulsive. Such repulsive curves do not support any bound states. Based upon these curves, we can conclude that there are no bound states for $^4He_3$ trimers with nonzero angular momentum. Although the calculations were carried out using the pair interaction of Aziz and Slaman [13], the adiabatic hyperspherical potential curves are changed only slightly when other helium pair interactions are used, as demonstrated by Esry *et al* [1] for $J = 0$. Thus, the conclusion that no bound states exist for nonzero angular momenta is not expected to change for calculations using other accurate helium interaction potentials. It should be noted that the pair potential

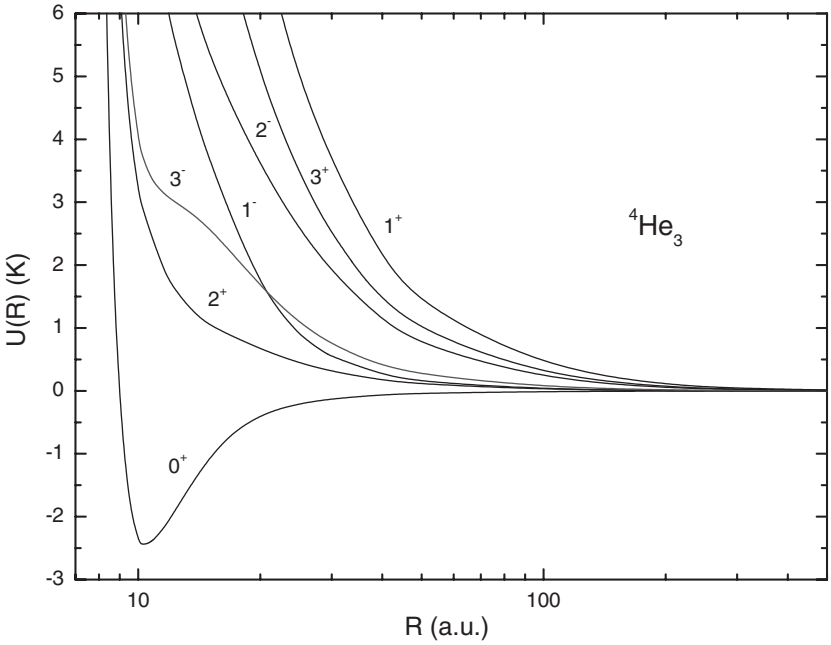

Figure 1. Lowest adiabatic hyperspherical potential curves for $^4He_3$, for each J^π symmetry indicated.

does not include the retardation effect. This effect, however, is estimated [6] to *decrease* the binding and hence does not change our conclusion.

Bound states for $^4He_3$ have been sought by Bruch [6] for the 1^- and 2^+ symmetries. He used totally symmetric variational trial functions for each symmetry and obtained upper bounds that lie above the $^4He_2$ threshold. Since the variational wavefunction used was limited, he concluded that rotational states, if they exist, would have binding energies of less than 1 mK. We note that he found the energy ordering of the 1^- and 2^+ states to be opposite to that shown in figure 1, possibly also due to the limitations of the trial wavefunctions. The 1^- symmetry has also been studied by Nielsen [15] using the coordinate space Faddeev approach coupled with an adiabatic hyperspherical approximation. For 1^-, he also found a completely repulsive potential for $^4He_3$. Based on our adiabatic potential curves for several symmetries, our conclusion is more definite. The curves in figure 1 have no attractive wells and so do not support any bound states for $J \neq 0$.

In figure 2 we show the potential curves for $^4He_2{}^3He$. It is interesting to note that the order of the J^π curves differs from that shown in figure 1 for $^4He_3$: in particular, the 1^- curve is the second lowest state for $^4He_2{}^3He$. This is the result of quantum statistics: the wavefunction for $^4He_3$ must be symmetric under exchange of any pair of particles; for $^4He_2{}^3He$, the wavefunction needs to be symmetric only under the exchange of the two ^4He atoms. We explore the consequences of the different permutational symmetry requirements further below.

In the present calculation, the permutational symmetry is not imposed directly in the numerical solution of equation (1) primarily because it is not a simple matter to impose this symmetry *a priori* in the Delves coordinates. Such a procedure is more easily carried out in Smith–Whitten-type coordinates [14]. Instead, the permutation symmetry is identified in the calculated solutions. To illustrate this point, figure 3 shows the potential curves calculated for

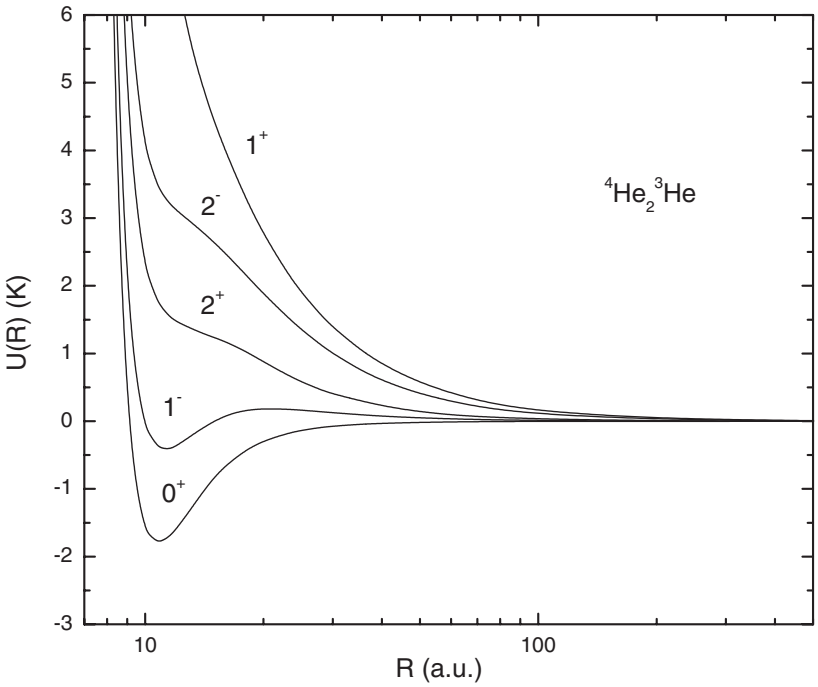

Figure 2. Lowest adiabatic hyperspherical potential curves for $^4He_2{}^3He$, for each J^π symmetry indicated.

1^- without imposing the fact that $^4He_3$ is a bosonic system. The eigensolutions consist of wavefunctions that are totally symmetric, totally antisymmetric, and also of mixed symmetry. The symmetric solution is, of course, the physical one for the three-boson $^4He_3$. The other three are relevant for atoms with nonzero spins. The mixed-symmetry states have to be coupled to spin functions to yield total wavefunctions of the appropriate symmetry. The mixed-symmetry states can be easily identified since their energies are doubly degenerate. Among the four curves in figure 3, the mixed-symmetry curves are indicated by dotted lines. The totally symmetric curve is denoted by a solid curve, and the totally antisymmetric curve is denoted by a dashed curve. We note that the von Neumann–Wigner non-crossing rule from molecular structure applies here so that curves of different symmetry can cross.

We can most easily differentiate the totally symmetric state from the totally antisymmetric state by examining the wavefunction with respect to the interchange of particles 1 and 2. Under this interchange, the components of the channel function should simply be symmetric or antisymmetric about $\theta = \pi/2$. With our choice of quantization axis, an interchange of particles 1 and 2 gives a phase $P(-1)^{J-I}$ from the $\bar{D}$ function [16], where P is the reflection symmetry with respect to the plane of the three particles; $P = +1$ if $\pi = (-1)^J$ and $P = -1$ if $\pi = -(-1)^J$. Since the total wavefunction must be symmetric with respect to the exchange of particles 1 and 2, the symmetry condition for each I-component, $\psi_{I\nu}(R; \theta, \phi)$, is also given by $P(-1)^{J-I}$. For 1^- states, for example, the $I = 0(1)$ component must be antisymmetric (symmetric) with respect to $\theta = \pi/2$. This procedure is sufficient to allow us to identify the curve with the correct symmetry. In figure 3 the correct curve for the bosonic $^4He_3$ is drawn as a solid line. It is *not* the lowest curve. (The higher-lying curves of figure 3 were not analysed since they are irrelevant for the present purpose.)

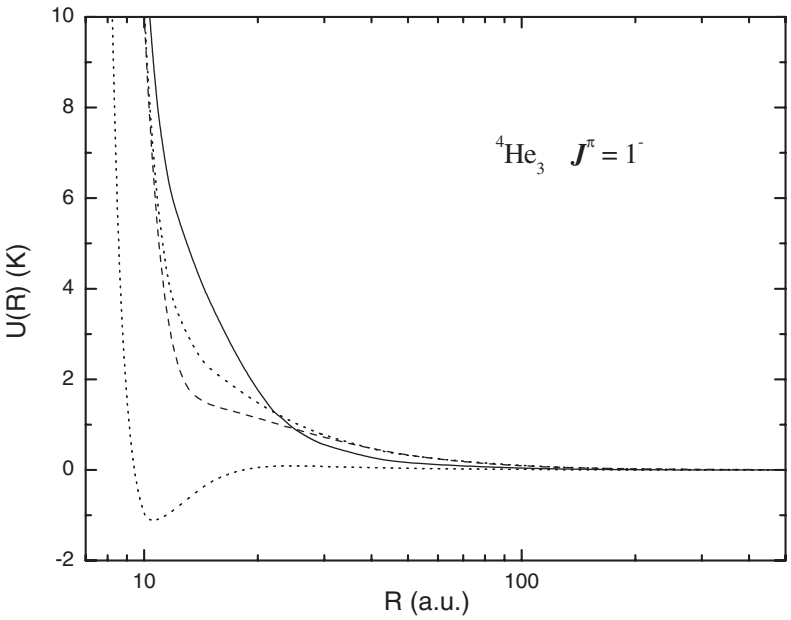

Figure 3. Hyperspherical potential curves for ^{4}He$_3$ without imposing any permutational symmetry. The curve with the correct boson statistics is indicated by the solid curve. The totally antisymmetric solution is shown with a dashed curve, and the mixed-symmetry solutions are shown with dotted curves. Only the curves shown were analysed.

For ^{4}He$_2{}^3$He, the curves are quite close to the curves in figure 3 for which the symmetry condition is not imposed. However, each pair of degenerate curves now splits into two distinct curves. The correct curve for ^{4}He$_2{}^3$He is the lowest one for which the wavefunction is symmetric under the exchange of particles 1 and 2. The procedure described in the last paragraph can be used to identify this curve. In this case, the correct curve is the lowest curve. Consideration of quantum statistics thus explains why the 1^- curve for ^{4}He$_2{}^3$He, shown in figure 2, is much lower than the 1^- curve in ^{4}He$_3$, shown in figure 1. Note that the 1^- curve for ^{4}He$_2{}^3$He has a small well. Direct solution of the hyper-radial equation for this potential shows that this well is too shallow to support a bound state since the energy thus obtained is a rigorous lower bound to the exact ground state energy [17]. Further, our calculations show that the dimer potential must be made more than 20% deeper before this well will support a bound state. Neither of the major inaccuracies in the interaction potential used—neglect of three-body effects and inexact two-body potentials—can account for a change of this magnitude. These inaccuracies are expected to be on the order of one per cent or less [18, 19].

It is interesting to ask why the ^{4}He$_3$ potential curves for different values of J^π appear in the order shown in figure 1. We emphasize that this is the result of quantum statistics. The effect of boson statistics from exchanging particles 1 and 2 on the rotational component wavefunction $\psi_{I\nu}(R;\theta,\phi)$ has been addressed in the last two paragraphs, but the effects of interchanging 1 and 3 or 2 and 3 have not yet been addressed. In fact, the body-frame quantization axis chosen in our calculation is not the most convenient for addressing the symmetry of three identical particles. A better quantization axis turns out to be one perpendicular to the plane of the three particles. Using this quantization axis, Bao *et al* [11] analysed the symmetry properties of each rotational component wavefunction. They showed that quantum symmetry often imposes nodal surfaces on the rotational component wavefunctions. Since each nodal surface implies

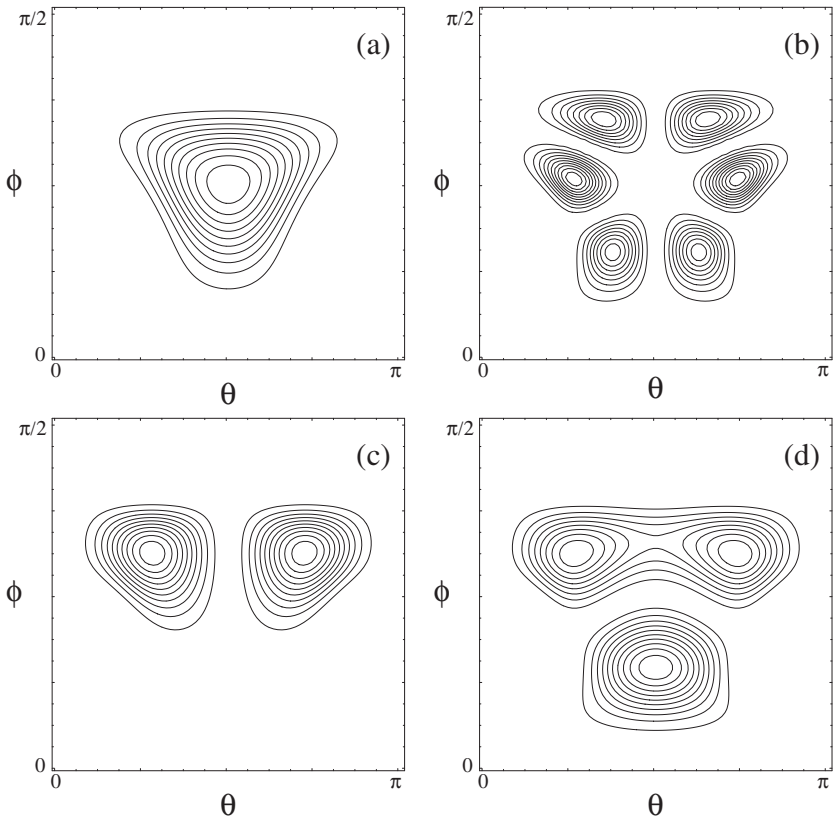

Figure 4. Contour plots of the square of selected rotational component wavefunctions including the volume element $\sin\theta$. At $R = 10.2$ au, (*a*) $I = 0$ for 0^+, and at $R = 12$ au, (*b*) $I = 1$ for 1^+, (*c*) $I = 1$ for 2^+ and (*d*) $I = 1$ for 1^-.

a higher kinetic energy, the low-lying states are occupied by those states that have the fewest nodal lines. Even with our choice of body-frame quantization axis, we can still see this effect in the rotational component wavefunctions, implying that the choice of quantization axis is not essential. The weights of each body-frame component would certainly change, but the number of nodal surfaces would remain the same.

In figure 4 we show some examples of the square of the rotational component wavefunction on the (ϕ, θ) plane calculated at the R values indicated. In figure 4(*a*) for $J = 0$, the density has no nodal lines and peaks at the equilateral triangle geometry near $\theta = \pi/2$ and $\phi = 0.734$. Figure 4(*b*) for 1^+ ($I = 1$—the $I = 0$ component is identically zero since $P = -1$) shows that this state has three nodal lines in agreement with the analysis of Bao *et al* [11]. Because there are three nodal lines, the potential curve for 1^+ is very repulsive, as seen in figure 1. In the two cases above, each wavefunction has only one rotational component, and thus the contour plots also represent the density distributions of the three particles.

We next consider 2^+ and 1^-, which have three and two rotational components, respectively. For 2^+, the $I = 2$ component is nodeless like the 0^+ state in figure 4(*a*). The $I = 1$ component has a node, as shown in figure 4(*c*). The $I = 0$ component also has no node but is distributed differently, with the maximum away from the equilateral triangle configuration. The weights for the three components are given in table 1, showing the predominance of the $I = 0$ and 2

Table 1. Weights of the I-components of $^4He_3$. The $J = 0$ weight is calculated at $R = 10.2$ au while the rest are calculated at $R = 12$ au.

J^π	$I = 0$	$I = 1$	$I = 2$	$I = 3$
0^+	1.0			
1^+		1.0		
1^-	0.302	0.698		
2^+	0.478	0.159	0.363	
2^-		0.730	0.270	
3^+		0.309	0.503	0.188
3^-	0.228	0.646	0.073	0.053

components for 2^+. For 1^-, the $I = 0$ component is similar to figure 4(c) with a nodal line at $\theta = \pi/2$. The $I = 1$ component is shown in figure 4(d). It has a nodal line at a nearly constant ϕ. The fact that there are rotational components that have no nodal lines for 2^+ means that the 2^+ curve is lower in energy. For 1^-, both components have one nodal line, and thus its potential curve is higher.

Similar analysis shows that the $I = 1$ and 3 components of 3^- have no nodes, while the $I = 0$ and 2 components each have a nodal line along $\theta = \pi/2$, and the weight is largest for the $I = 1$ component (see table 1). For 2^-, the $I = 1$ component is similar to figure 4(d), and the $I = 2$ component is similar to figure 4(c). Both components have one node, and thus the potential curve is higher. For 3^+, all three rotational component wavefunctions have one nodal line, and the 3^+ curve is very repulsive.

The origin of the nodal line at $\theta = \pi/2$ in figures 4(b) and (c) and the two additional nodal lines in figure 4(b) emerges more clearly as permutational symmetry requirements when the analysis of Bao *et al* [11] is adopted. Since these nodal lines are the consequence of quantum statistics, their locations are independent of the hyper-radius R. Therefore, this analysis shows that quantum statistics imposes severe constraints on the rotational component wavefunctions that are reflected in the ordering of the potential curves. A similar analysis has been used to investigate the relative positions of the energy levels of triply excited states of atoms [20].

In summary, we have calculated the adiabatic hyperspherical potential curves for the nonzero angular momentum states for $^4He_3$ and $^4He_2{}^3He$. From the repulsive nature of these curves, we conclude that there are no $J \neq 0$ bound states for either system, ruling out the possibility of finding any bound states for nonzero angular momenta in $^4He_3$. The adiabatic hyperspherical approximation is a powerful method for searching for the existence of diffuse bound states since the binding energy need not be directly calculated. Rather, their existence can often be inferred directly from the calculated potential curves. For $^4He_3$, for example, the curves have no attractive well for $J > 0$, while for $^4He_2{}^3He$ a direct solution of the hyper-radial equation for 1^- shows that there are no bound states.

This work is supported in part by the Division of Chemical Sciences, Office of Basic Energy Sciences, Office of Science, US Department of Energy. The authors acknowledge useful conversations with E Nielsen in the early stages of this work, and CDL acknowledges helpful correspondence with Dr C G Bao.

References

[1] Esry B D, Lin C D and Greene C H 1996 *Phys. Rev.* A **54** 394
[2] Blume D and Greene C H 2000 *J. Chem. Phys.* **112** 8052
[3] Nielsen E, Fedorov D V and Jensen A S 1998 *J. Phys. B: At. Mol. Opt. Phys.* **31** 4085

[4] Lewerenz M 1997 *J. Chem. Phys.* **106** 4596
[5] González-Lezana T, Rubayo-Soneira J, Miret-Artés S, Gianturco F A, Delgado-Barrio G and Villarreal P 1999 *Phys. Rev. Lett.* **82** 1648
González-Lezana T, Rubayo-Soneira J, Miret-Artés S, Gianturco F A, Delgado-Barrio G and Villarreal P 1999 *J. Chem. Phys.* **110** 9000
[6] Bruch L W 1999 *J. Chem. Phys.* **110** 2410
[7] Luo F, McBane G C, Kim G, Giese C F and Gentry W R 1993 *J. Chem. Phys.* **98** 3564
[8] Schöllkopf W and Toennies J P 1994 *Science* **226** 1345
[9] Schöllkopf W and Toennies J P 1996 *J. Chem. Phys.* **104** 1155
[10] Luo F, Giese C F and Gentry W R 1996 *J. Chem. Phys.* **104** 1151
[11] Bao C G, Xie W F and Ruan W Y 1997 *Few-Body Syst.* **22** 135
[12] Zhou Y and Lin C D 1994 *J. Phys. B: At. Mol. Opt. Phys.* **27** 5065
[13] Aziz R A and Slaman M J 1991 *J. Chem. Phys.* **94** 8047
[14] Whitten R C and Smith F T 1968 *J. Math. Phys.* **9** 1103
[15] Nielsen E 1999 *PhD Thesis* Aarhus University
[16] Bhatia A K and Temkin A 1964 *Rev. Mod. Phys.* **36** 1050
[17] Sucre M G, Goychman F and Lefebvre R 1970 *Phys. Rev.* A **2** 1738
[18] Roeggen I and Almlöf J 1995 *J. Chem. Phys.* **102** 7095
[19] Aziz R A, Janzen A R and Moldover M R 1995 *Phys. Rev. Lett.* **74** 1586
[20] Morishita T and Lin C D 1998 *Phys. Rev.* A **57** 4268

4.4 Part II: Quantum Mechanical Approach

Paper IV: Charge transfer and excitation in slow 20 eV – 2 keV H^++D(1s) collisions, submitted to J. Phys. B: At. Mol. Opt. Phys.

Charge transfer and excitation in slow 20 eV – 2 keV H^+ + D(1s) collisions

T G Lee‡, Anh-Thu Le and C D Lin

Department of Physics, Cardwell Hall, Kansas State University, Manhattan, KS 66506, USA

Abstract. We used the recently developed hyperspherical close-coupling method to study H^+ + D(1s) collisions at H^+ impact energies between 20 eV and 2 keV. We showed that cross sections for excitation and charge transfer to the 2p states are essentially identical over the whole energy range and stay relatively independent of energy from 2 keV down to about 150 eV. Below 150 eV the cross sections drop precipitously with decreasing energy. Electron capture to H(1s) cross section in this energy region has also been calculated.

Submitted to: *J. Phys. B: At. Mol. Phys.*

PACS numbers: 34.70.+e, 34.10.+x, 31.15.Ja

‡ E-mail me at: ltg@phys.ksu.edu

1. Introduction

Slow ion-atom collisions have been a subject of great interest for decades. The most elementary collision system H^++H has attracted a great deal of interest both by theorists and by experimentalists. Due to the difficulty of manipulating a low energy ion beam, most of the experimental data have been taken at energies above about 1 keV. These experimental results, for energies between say, about 10 keV and 500 keV, are relatively well described by the different theoretical approaches developed in the last few decades [1, 2]. Between 1 keV and 10 keV, the major remaining issue, both in theory and experiment, is the total and differential impact ionization cross sections, see recent works in [3, 4, 5, 6, 7]. Ionization is a weak process below 10 keV and the cross section is small compared to the resonant charge transfer process. It is also small compared to excitation and charge transfer to the $n = 2$ states.

The focus of the present work is the collision of H^++D(1s) from 2 keV down to about 20 eV . (The collision energy used in this paper refers to the H^+ impact energy in the laboratory frame, with the target initially at rest.) Here, not only are there few experiments available, the number of theoretical studies is also quite limited. In this energy regime, the dominant process is charge transfer to H(1s) which is well understood since it differs little from the resonant charge transfer in H^++H collisions. (Charge transfer for the latter process below 2 eV has been examined previously in papers [8, 9]). The next dominant process is the excitation and charge transfer to $n = 2$ states. Existing calculations and experiments in the 2–10 keV region indicate that excitation and capture to the 2s state are much smaller and the cross section drops rapidly with the decreasing collision energy, see McLaughlin *et al* [10] for summary of earlier references. On the other hand, excitation and charge transfer cross sections to 2p are larger and remain nearly constant in this energy range. One of the major motivations of the present theoretical study is the question if the 2p cross section will begin to decrease at a certain energy and if so, at what energy.

Despite the great progress made in ion-atom collision theory in the past few decades, most of the effort has been focused in the higher energy region where the motion of the heavy particles can be treated classically. Using the impact parameter approach the time-dependent electronic wave function can be expanded in terms of either atomic orbitals or in terms of molecular orbitals (MO). The latter is called perturbed stationary states (PSS) approximation and has been first proposed by Massey and Smith [11] in 1933. If the impact velocity is small in comparison with the typical speed of the electron then the PSS model is preferred. However, in PSS the molecular basis functions do not satisfy the correct asymptotic boundary condition and the calculated results are not Galilean invariant. To overcome this difficulty, various forms of electron translational factors or switching functions have been introduced [12, 13, 14, 15]. These functions have also been extended to collisions at lower energies where semiclassical treatment fails and quantum description of the motion of the heavy particles is needed. Similar switching functions or the more advanced reaction coordinates have been introduced in

the quantum theory [16, 17, 18, 19]. Calculations based on such models are not founded on first principles since the switching functions or reaction coordinates have to be chosen in an *ad hoc* manner.

In view of these deficiencies, we have recently developed the hyperspherical close-coupling (HSCC) method to study low-energy ion-atom collisions [20]. There is no *ad hoc* parameter in the theory and the accuracy of the method can be checked in principle by increasing the number of channels included in the close-coupling calculations. The HSCC method has been applied to a few ion-atom collision processes so far [20, 21, 22]. In this work we present HSCC results for H^++D(1s) collisions from 20 eV to 2 keV. In this energy region, the results are expected to be identical to H^++H(1s) collisions. This paper is organized as follows. In Section 2, we review briefly the hyperspherical close-coupling method for ion-atom collisions. Results for H^++D(1s) reaction are presented in Section 3. Summary and conclusions are given in Section 4. Atomic units are used unless otherwise indicated.

2. Hyperspherical close coupling theory

The details of the HSCC theory are given in Liu *et al* [20]. In the center-of-mass frame we solved the time-independent Schrödinger equation for the three-body HD^+ system in the mass-weighted hyperspherical coordinates. Let $\vec{\rho}_1$ be the first Jacobi vector from D^+ to H^+, with reduced mass μ_1; $\vec{\rho}_2$ be the second Jacobi vector from the center of mass of D^+ and H^+ to the electron, with reduced mass μ_2. The hyperradius R and hyperangle ϕ are defined as

$$R = \sqrt{\frac{\mu_1}{\mu}\rho_1^2 + \frac{\mu_2}{\mu}\rho_2^2}, \tag{1}$$

$$\tan\phi = \sqrt{\frac{\mu_2}{\mu_1}}\frac{\rho_2}{\rho_1}, \tag{2}$$

where μ is arbitrary. We further define angle θ as the angle between the two Jacobi vectors. If we choose μ to be equal to μ_1, then the hyperradius R is very close to the internuclear separation. By introducing the rescaled wave function

$$\Psi(R,\Omega,\hat{\omega}) = \psi(R,\Omega,\hat{\omega})R^{3/2}\sin\phi\cos\phi, \tag{3}$$

we solve the Schrödinger equation in the form

$$\left(-\frac{1}{2}\frac{\partial}{\partial R}R^2\frac{\partial}{\partial R} + \frac{15}{8} + H_{ad}(R,\Omega,\hat{\omega}) - \mu R^2 E\right)\Psi(R,\Omega,\hat{\omega}) = 0, \tag{4}$$

with $\Omega \equiv \{\phi,\theta\}$ and $\hat{\omega}$ denotes the three Euler angles of the body-fixed frame axes with respect to the space-fixed frame. The H_{ad} is the adiabatic Hamiltonian with the hyperradius fixed. To solve equation (4), we expand the rescaled wave function as

$$\Psi(R,\Omega,\hat{\omega}) = \sum_{\nu}\sum_{I} F_{\nu I}(R)\Phi_{\nu I}(R;\Omega)\tilde{D}^J_{IM_J}(\hat{\omega}), \tag{5}$$

where ν is the channel index, J is the total angular momentum, I is the absolute value of the projection of $\vec{J}$ along the body-fixed z' axis, taken to be the axis between the two heavy particles, M_J is the projection along the space-fixed z axis. In this equation, $\tilde{D}$ is the normalized and symmetrized rotation function. The body-frame adiabatic basis functions $\Phi_{\mu I}(R;\Omega)$ are solutions of a two-dimensional partial differential equation in Ω which are solved in terms of B-spline functions. The resulting coupled hyperradial equations are solved using the R-matrix propagation method. Within each sector, the smooth variable discretization technique was used. We comment that the expansion (5) is very similar to the PSS expansion except that we use hyperradius as the adiabatic parameter, instead of internuclear separation as in the PSS theory.

In Fig. 1 we show the adiabatic hyperspherical potential curves for HD^+ that converge to the $n = 1$ and $n = 2$ states of H and D. These eight adiabatic channels were used in the HSCC calculation, even though we will show that in the energy region of interest, calculations based only on four channels will be adequate. Within the accuracy shown in Fig. 1, these potential curves are essentially identical to the Born-Oppenheimer potential curves. In actuality, the two lowest curves are separated by about 3.7 meV, which is the energy difference between H(1s) and D(1s), since the HSCC method does account for the mass effect, in contrast to the PSS method. Similarly, the excited state curves converge to H or D $n = 2$ states as well.

The basic collision dynamics for the present system is well-known. The two lowest curves have an avoided crossing near R$\simeq$12 a.u. [8], which is responsible for the charge transfer from D(1s) to H(1s). The upper curve of the pair, to be called 2pσ, in analogy to the H_2^+ potential, is known to rotationally coupled to the 2pπ curve (the lowest $I = 1$ curve in Fig. 1) at small distances. This rotational coupling is responsible for populating the 2p state in H^++H collisions — a fact well understood already from the semiclassical theory for collisions above 1–2 keV.

3. Results and discussions

From the present HSCC calculations using the eight channels shown in Fig. 1, we obtained electron capture to H(2p) and excitation to D(2p) cross sections. The results are shown in Fig. 2 as solid lines. Since the major mechanism for populating these states is the rotational coupling, a four-state calculation including only the two lowest $I = 0$ and two lowest $I = 1$ states would give essentially the same results, as shown by crosses in Fig. 2. We also comment that the 2p states thus populated are almost pure 2pπ states where the quantization axis is the incident beam direction. This is already the case for collision energy at about 2 keV, see Table I of Fritsch and Lin [23].

Fig. 2 shows the results that we were looking for. The 2p excitation or capture cross sections stay relatively constant till about 150 eV. From there they drop rapidly as the collision energy is reduced.

In Fig. 2 we also show other theoretical results and the unpublished experimental data from Barnett [24] at energies down to 500 eV. These experimental data show

relatively large difference between excitation and capture to the 2p states. Based on the molecular orbital concept, and supported by the present HSCC calculation, there is no reason to expect these two cross sections to differ in this energy region. It is noted that the cross sections for these two processes are known to be essentially the same in the 1-5 keV region [2]. Similarly, it is difficult to interpret the theoretical results from the 3-center atomic orbital close coupling (3CAOCC) calculations by McLaughlin *et al* [10] which show that the two cross sections differ markedly below 1 keV. Note that a similar earlier 3-center calculation by Winter and Lin [25] showed that the two cross sections are identical at 1.56 keV and at 3 keV to within a few percents. The recent semiclassical time-dependent density functional theory (TDDFT) result of Tong *et al* [26] did show that the two cross sections are very close to each other down to collision energy of 1 keV. Their method used straight line trajectory and may begin to incur errors at the lowest energy point shown.

To understand the rapid drop of excitation and charge transfer cross sections to 2p states at low energies, as shown in Fig. 2, we display the 2pσ and 2pπ potential curves in more details in Fig. 3 in the small R region since the rotational coupling between these two curves is responsible for the transitions. The positions of the classical turning point for the 2pπ curve for collision energy at 60, 45 and 30 eV are shown. In the inset the energy gap between the 2pσ and 2pπ curves at the position of the classical turning point for the 2pπ curve as functions of impact energy is shown. This energy gap increases rapidly at lower impact energy, making transitions from 2pσ to 2pπ via rotational coupling less and less efficient. At impact energy of 100 eV and higher, the energy gap is practically zero and the rotational coupling is efficient. The classical turning points in this figure were calculated for zero total angular momentum. For higher total angular momenta, the turning points will be shifted to larger R, which leads to larger energy gaps. Thus the rapid drop of 2p excitation and charger transfer cross sections at lower energies can be understood based on the adiabatic hyperspherical (or even Born-Oppenheimer) potential curves.

In the present calculations, we also obtained electron capture cross section to H(1s). In Fig. 4 we compared the HSCC result with the early calculation by Dalgarno and Yadav [27], the recent (TDDFT) result of Tong *et al* [26] and the recommended data from Oak Ridge National Laboratory (ORNL). We present partial-wave cross sections in terms of the impact parameter dependence probabilities according to the relation

$$\sigma_J = \frac{2\pi b P(b)}{k}, \tag{6}$$

with $J = kb$, where k is the momentum. The results for capture and excitation to 2p states as well as capture to H(1s) are shown in Fig. 5 and Fig. 6, respectively.

In Fig. 5, for high impact energies (*i.e.,* 0.5 and 1 keV), the probabilities of capture to H(2p) and excitation to D(2p) differ by ∼3%. As the collision energy is decreased, the two probabilities are practically lying on top of each other. Their general features do not differ much from those in the few keV energy region [23, 25]. Namely, the probabilities for the excitation to D(2p) and charge transfer to H(2p) are *bell-shape* functions of

impact parameters. In contrast, the H(1s) capture probability oscillates rapidly, and more so as the collision energy is decreased. We remark that the nonzero minima in the oscillatory electron capture probability in Fig. 6 for small impact parameters are the consequence of rotational coupling.

4. Summary

In summary, we have employed the recently developed hyperspherical close coupling method to obtain excitation and charge transfer cross sections to 2p states in H^++D (applicable to H^++H also) collisions at energies from 20 eV to 2 keV. The two cross sections are shown to be essentially identical and remain nearly energy-independent from 2 keV down to about 150 eV. Below that energy, the cross sections drop precipitously. The drop has been attributed to the increasingly larger energy gap between the 2pσ and 2pπ curves in the classically allowed region, thus making the rotational coupling inefficient in populating the 2p state.

5. Acknowledgement

TGL would like to acknowledge the discussions with Dr. M. Hesse. This work was supported in part by the Chemical Sciences, Geosciences and Biosciences Division, Office of Basic Energy Sciences, Office of Science, U. S. Department of Energy.

References

[1] Bransden B H and McDowell M R C 1992 *Charge Exchange and Theory of Ion-Atom Collisions* (Clarendon, Oxford)
[2] Fritsch W and Lin C D 1991 *Phys. Rep.* **202** 1
[3] Sidky E, Illescas C and Lin C D 2000 *Phys. Rev. Lett.* **85** 1634
[4] Schultz D R, Reinhold C O, Krstic P S and Strayer M R 2002 *Phys. Rev.* A **65** 052722
[5] Macek J H and Ovchinnikov S Y 1998 *Phys. Rev. Lett.* **80** 2298
[6] Shah M B, Geddes J, McLaughlin B M and Gilbody H B 1998 *J. Phys. B: At. Mol. Opt. Phys.* **31** L757
[7] Pieksma M, Ovchinnikov S Y, Van Eck J, Westerveld W and Niehaus A 1994 *Phys. Rev. Lett.* **73** 46
[8] Igarashi A and Lin C D 1999 *Phys. Rev. Lett.* **83** 4041
[9] Esry B D and Sadeghpour H R 1999 *Phys. Rev.* A **60** 3604
[10] McLaughlin B M, Winter T G and McCann J F 1997 *J. Phys. B: At. Mol. Opt. Phys.* **30** 1043
[11] Massey H S and Smith R A 1933 *Proc. R. Soc.* A **142** 142
[12] Delos J B 1981 *Rev. Mod. Phys.* **53** 287
[13] Thorson W R, Kimura M, Choi J H and Knudson S K 1981 *Phys. Rev.* A **24** 1768
[14] Scheiderman S B and Russek A 1969 *Phys. Rev.* **181** 311
[15] Vaanben J and Taulbjerg K 1981 *J. Phys. B: At. Mol. Opt. Phys.* **14** 1815
[16] Errea L F, Harel C, Jouin H, Mendez L, Pons B and Riera A 1998 *J. Phys. B: At. Mol. Opt. Phys.* **31** 3527
[17] Croft H and Dickinson A S 1996 *J. Phys. B: At. Mol. Opt. Phys.* **29** 57
[18] Gargaud M, McCarroll R and Valiron P 1987 *J. Phys. B: At. Mol. Opt. Phys.* **20** 1555
[19] Shimakura N and Kimura M 1991 *Phys. Rev.* A **44** 1659

[20] Liu C N, Le A T, Morishita T, Esry B D and Lin C D 2003 *Phys. Rev.* A **67** 052705
[21] Le A T, Liu C N and Lin C D 2003 *Phys. Rev.* A **68** 012705
[22] Le A T, Hesse M, Lee T G and Lin C D 2003 *J. Phys. B: At. Mol. Opt. Phys.* **36** 3281
[23] Fritsch W and Lin C D 1982 *Phys. Rev.* A **26** 762
[24] Barnett C F 1990 *Oak Ridge National Laboratory Report* No. 6086, unpublished
[25] Winter T G and Lin C D 1984 *Phys. Rev.* A **29** 567
[26] Tong X M, Kato D, Watanabe T and Ohtani S 2001 *Phys. Rev.* A **62** 052701
[27] Dalgarno A and Yadav H N 1953 *Proc. R. Soc. London* A **66** 173
[28] Newman J H, Colgan J D, Ziegler D L, Nitz D E, Rundel R D, Smith K A and Stebbings R F 1982 *Phys. Rev.* A **25** 2976

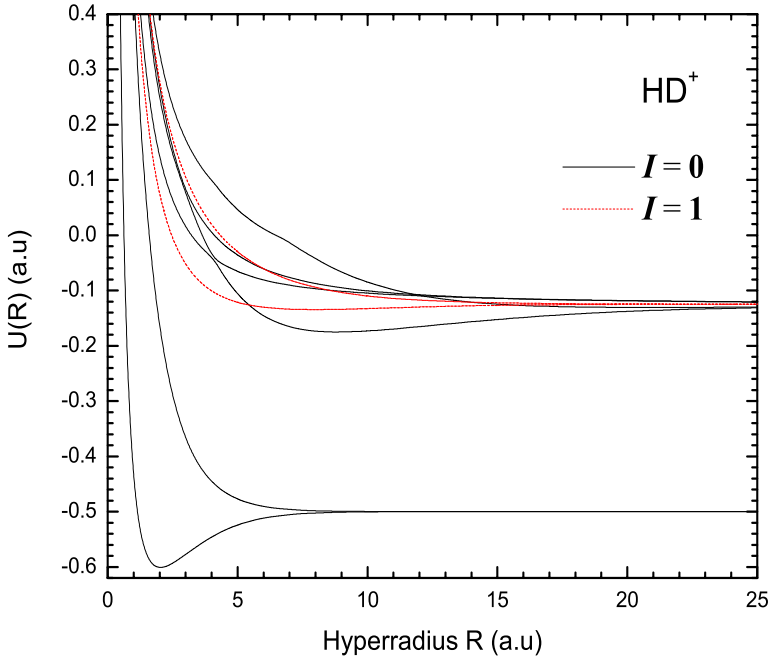

Figure 1. Adiabatic hyperspherical potential curves for HD^+. The figure shows six $I = 0$ channels in solid line, two $I = 1$ channels in broken line.

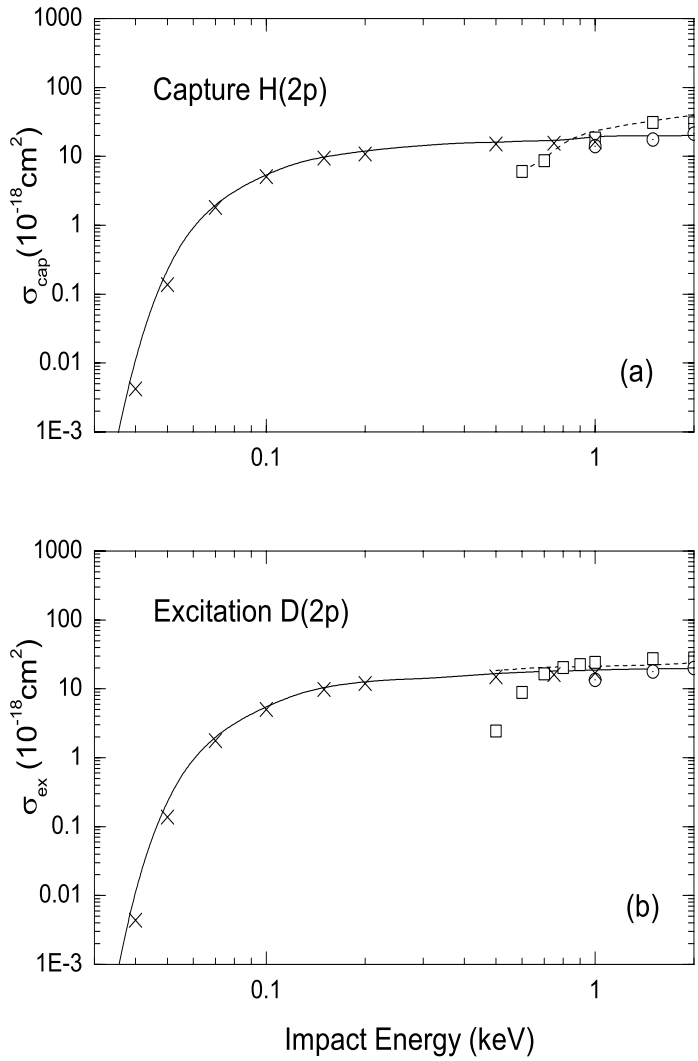

Figure 2. Comparison of the HSCC calculations with available experimental and semiclassical results for H^+ + D(1s) collisions. (a) Electron capture to H(2p) level: ——, HSCC (8 channels); ×, HSCC (4 channels); - - - - , 3CAOCC; ⊙, TDDFT; □, ORNL (Barnett 1990). (b) Same as (a) but for excitation to D(2p) level.

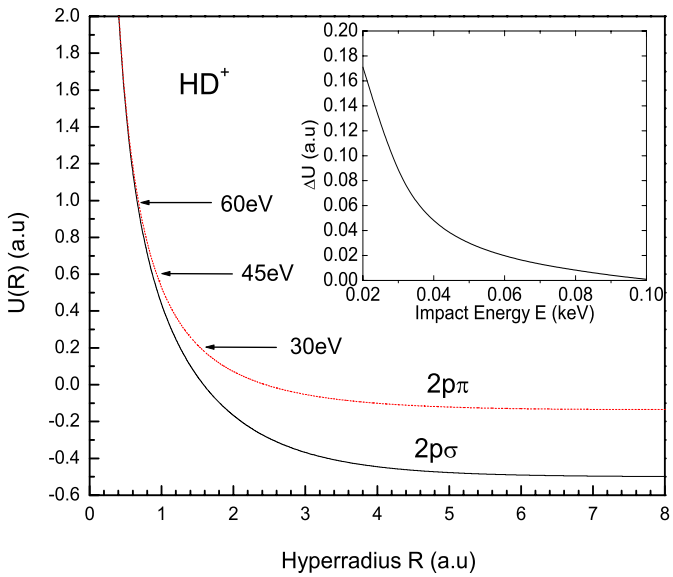

Figure 3. Adiabatic hyperspherical potential curves for 2pσ and 2pπ states. Arrow indicates the position of the classical turning point of the 2pπ curve at the given proton impact energy. Inset shows the energy difference between these two curves at the classical turning point as a function of proton impact energy.

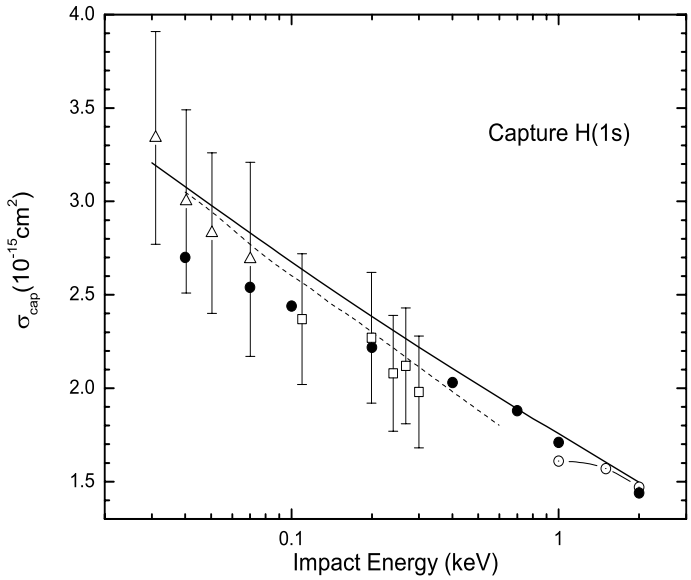

Figure 4. Comparison of the capture cross sections of H(1s) from HSCC with the existing experimental and theoretical results. ——, HSCC; - - - -, Dalgarno and Yadav (1953) [27]; ⊙, TDDFT [26]; •, ORNL (Barnett 1990); △, H^++D(1s) [28]; □, H^++H(1s) [28].

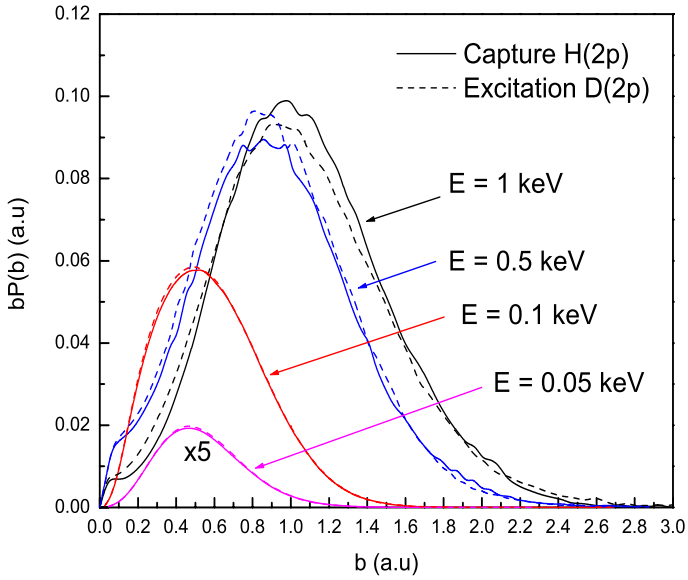

Figure 5. Impact parameter-weighted probabilities as functions of impact parameter b for collision energies of E = 0.05 to 1 keV.

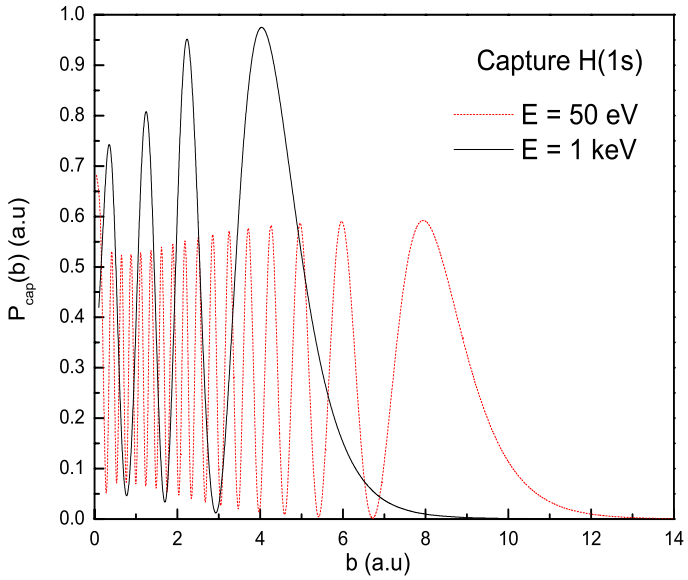

Figure 6. Electron capture probabilities as functions of impact parameter b for collision energies E = 50 eV and 1.0 keV.

Chapter 5

Summary and Concluding Remarks

In this dissertation we have studied various inelastic ion-atom collision processes at low to high energies within the framework of close-coupling formalism. Two theoretical methods have been employed in the present work, namely (i) the semi-classical approach, and (ii) the quantum-mechanical approach.

Detail studies of many different collision systems were carried out using the semi-classical close-coupling approximation. However, only the collision systems of $\bar{p}$ + He($1s^2$) and Na^+ + Rb(5s,5p) are highlighted here. For the $\bar{p}$ + He($1s^2$) collision system, an extensive two-electron two-center atomic orbital close-coupling (TCAOCC2e) calculation was performed to study the single ionization cross sections of atomic He. The stability of the ionization probability and cross sections were examined. The results from two different basis sets were shown to support the accuracy of the cross sections presented. While general agreement between theory and experiment is achieved for collision energies above 50 keV, we believe that the deviations below 40 keV are likely due to experimental difficulties. The discrepancy due to approximations in theoretical calculations was ruled out, and the conclusion is that the ionization cross sections of He by anti-protons impact below 40 keV should be remeasured.

With the combination of the Eikonal approximation, the semiclassical one-electron two-center atomic orbital close-coupling (TCAOCC1e) was utilized to study the state-selective

differential charge transfer cross sections for Na^+ + Rb(5s,5p) for impact energies at E = 2, 5, and 7 keV. The results are compared to the recent measurements obtained with Rb targets cooled in a magnetic optical trap recoil ion momentum spectroscopy (MOTRIMS). We have shown that the theoretical results agreed extremely well with the experiments for dominant charge transfer channels. However, for weak channels, the agreement is less satisfactory. This discrepancy may indicate a sign of failure both in the theory and experiment to obtain the accurate results for weak channels. Despite the fine resolution offered by MOTRIMS, the present MOTRIMS results are still unable to test the oscillatory structures predicted for differential cross sections, in particular, for transitions from excited initial states.

Turning to the quantum mechanical approach, the adiabatic hyperspherical method has been applied to obtain the hyperspherical potential curves for non-zero angular momenta states for $^4He_3$ and $^4He_2{}^3He$. The conclusion drawn from the repulsive nature of these curves is that there are no $J \neq 0$ bound states for either systems, ruling out the possibility of finding any bound rotational states for $^4He_3$. The symmetry properties of the trimer wave functions in the body-frame were also analyzed.

Later, a conjoint technique of hyperspherical coordinate, Smooth Variable Discretization (SVD) method and $\mathcal{R}$-matrix propagation scheme was used to study the charge transfer and excitation processes in slow 20 eV – 2 keV H^+ + D(1s) collisions. This quantum mechanical approach is free from ambiguities associated with the conventional Born-Oppenheimer (BO) method. The cross sections for excitation and charge transfer to 2p states were shown to be essentially identical over the whole energy range and stay relatively independent of energy from 2 keV down to 150 eV. Below 150 keV, the cross sections decrease precipitously with decreasing energy. With the aid of adiabatic hyperspherical potential curves, the rapid drop of cross sections was attributed to the increasingly larger gap between the 2pσ and 2pπ curves in the classically allowed region, and hence making the rotational coupling inefficient in populating the 2p state.

Appendix A

Independent Electron Model

Depending on the process that we are interested in, the two electrons can be treated either equivalently or non-equivalently. Suppose the two electrons are treated in a different way, then we have the probability for the first electron,

$$P_{el}^{(1)}(b) + P_{ex}^{(1)}(b) + P_{cap}^{(1)}(b) + P_{ion}^{(1)}(b) = 1 \tag{A.1}$$

and for the second electron,

$$P_{el}^{(2)}(b) + P_{ex}^{(2)}(b) + P_{cap}^{(2)}(b) + P_{ion}^{(2)}(b) = 1. \tag{A.2}$$

For the one-electron process, the expression

$$\{P_{el}^{(1)}(b) + P_{ex}^{(1)}(b) + P_{cap}^{(1)}(b) + P_{ion}^{(1)}(b)\}^2 = 1 \tag{A.3}$$

allows us to identify the probabilities for the single electron capture, excitation, or ionization as

$$\mathcal{P}_{cap}(b) = 2P_{el}^{(1)}(b)P_{cap}^{(1)}(b), \tag{A.4}$$

$$\mathcal{P}_{ex}(b) = 2P_{el}^{(1)}(b)P_{ex}^{(1)}(b), \tag{A.5}$$

$$\mathcal{P}_{ion}(b) = 2P_{el}^{(1)}(b)P_{ion}^{(1)}(b), \tag{A.6}$$

respectively.

Similarly, but for the two-electron process, the expression

$$\{P_{el}^{(1)}(b) + P_{ex}^{(1)}(b) + P_{cap}^{(1)}(b) + P_{ion}^{(1)}(b)\}\{P_{el}^{(2)}(b) + P_{ex}^{(2)}(b) + P_{cap}^{(2)}(b) + P_{ion}^{(2)}(b)\} = 1 \tag{A.7}$$

allows us to identify the probabilities of double capture, excitation, or ionization as

$$\mathcal{P}_{DC}(b) = 2P_{cap}^{(1)}(b)P_{cap}^{(2)}(b), \tag{A.8}$$

$$\mathcal{P}_{DE}(b) = 2P_{ex}^{(1)}(b)P_{ex}^{(2)}(b), \tag{A.9}$$

$$\mathcal{P}_{DI}(b) = 2P_{ion}^{(2)}(b)P_{ion}^{(2)}(b), \tag{A.10}$$

respectively. However, the expression for the probabilities of simultaneous processes like transfer ionization (TI), ionization excitation (IE) and transfer excitation (TE) becomes more complex

$$\mathcal{P}_{TI}(b) = P_{cap}^{(1)}(b)P_{ion}^{(2)}(b) + P_{cap}^{(2)}(b)P_{ion}^{(1)}(b), \tag{A.11}$$

$$\mathcal{P}_{IE}(b) = P_{ion}^{(1)}(b)P_{ex}^{(2)}(b) + P_{ion}^{(2)}(b)P_{ex}^{(1)}(b), \tag{A.12}$$

$$\mathcal{P}_{TE}(b) = P_{cap}^{(1)}(b)P_{ex}^{(2)}(b) + P_{cap}^{(2)}(b)P_{ex}^{(1)}(b), \tag{A.13}$$

respectively.

The corresponding cross section σ_X for either one-electron or two-electron X processes can be evaluated easily through

$$\sigma_X = 2\pi \int \mathcal{P}_X(b) b db \tag{A.14}$$

Note that it is possible to generalize the formula to account for many electron processes.

Appendix B

DVR Basis and Matrices

Consider a finite orthonormal set of functions

$$\phi_n(R),\ \{n = 1, ..., N\},$$
$$\int_a^b \phi_n(R)\phi_m(R)dR = \delta_{nm} \tag{B.1}$$

defined by

$$\phi_n(R) = \sqrt{\frac{w(R)}{h_{n-1}}} f_{n-1}(R), \tag{B.2}$$

where $f_n(R)$ are polynomials of degree n orthogonal on the interval $t \in [a, b]$ with some non-negative weight $w(R)$, and h_n are the normalization constants. The interval $[a,b]$ and the weight $w(R)$ define uniquely an N-point Gaussian quadrature:

$$\int_a^b F(R)w(R)dR \approx \sum_{i=1}^{N} \omega_i F(R_i) \tag{B.3}$$

where R_i and ω_i are the quadrature points and weights, respectively. Eqn. (B.3) holds approximately for all $F(R)$ such that the integral in the RHS exists; it becomes exact for $F(R)$ polynomial of degree $2n - 1$ or less. Following the above prescription, let us introduce the DVR basis:

$$\pi_i(R),\ \{i = 1, ..., N\},$$
$$\int_a^b \pi_i(R)\pi_j(R)dR = \delta_{ij} \tag{B.4}$$

and define the orthogonal transformation

$$\phi_n(R) = \sum_{i=1}^{N} T_{ni}\pi_i(R),\ \pi_i(R) = \sum_{n=1}^{N} T_{ni}\phi_n(R) \tag{B.5}$$

where

$$T_{ni} = (T^{-1})_{in} = \kappa_i\phi_n(R_i);\ \kappa_i = \sqrt{\frac{\omega_i}{w(R_i)}} \tag{B.6}$$

and the orthogonality of T follows from the Christoffel-Darboux identity[1]. The DVR basis functions (B.4) have the important property

$$\pi_i(R_j) = \kappa_i^{-1}\delta_{ij} \tag{B.7}$$

which appears as a *point-wise* basis conjugate to the *polynomial-wise* basis (B.2). Let $\phi_n(R)$ and $\pi_i(R)$ be the Legendre polynomial and DVR bases, respectively. It can be shown that

$$\frac{d\phi_n(R)}{dR} = \sum_m a_{nm}\phi_m(R), \tag{B.8}$$

where

$$a_{nm} = \begin{cases} \sqrt{(2n-1)(2m-1)}, & \text{if } m = n-1, n-3, ..., \geq 1, \\ 0, & \text{otherwise.} \end{cases}$$

Consider the matrix

$$F_{ij} = \int_{-1}^{1} \frac{d\pi_i(R)}{dR} F(R) \frac{d\pi_j(R)}{dR} dR \tag{B.9}$$

Using Eqn.(B.8) and quadrature (B.3), we obtain

$$F_{ij} = \sum_{k=1}^{N} b_{ik}F(R_k)b_{jk} \tag{B.10}$$

where

$$b_{ik} = \sum_{n,m=1}^{N} T_{ni}a_{nm}T_{mk} \tag{B.11}$$

[1] A.S. Dickinson and P.R. Certain, J. Chem. Phys. **49**, 4209 (1968)

Appendix C

TCAOCC Program

This appendix provides instruction on how to use the two-center atomic orbital close-coupling (TCAOCC) code. The numerical integration of the time-dependent close-coupling equation relies on three external standard numerical packages known as Eispack.f, Inverse.f and Rksuite.f, respectively. The meaning of the variables used as well as the internal subroutines required in the computer code are well documented in the beginning of the fortran program. However, for our convenience and since the meanings of the variables are more important than the subroutines themselves, we shall list only the explanation of the variables in section C.1. In addition, we also provide the sample input and output files for Li^+ + He collisions in the following two sections. To produce an executable file of the TCAOCC code, we need to compile the three external numerical packages first and then link to the main source code of TCAOCC. For example:

```
fort -extend_source -o tcaocc.x tcaocc.f Eispack.o Inverse.o
Rksuite.o
```

Since the code uses the Gauss-Legendre integration scheme, one required the Gauss-Legendre points name under Legendre.dat. The whole TCAOCC package, including the input and output, can be obtained from the author or Prof. C. D. Lin.

C.1 Explanation of variables

```
*   maxorbtlA:          maximum number of orbitals on center A
*   maxorbtlB:          maximum number of orbitals on center B
*   maxorbtlAB:         maxorbtlA+maxorbtlB
*   maxangl:            maximum # of angular momenta allowed
*   maxb:               maximum # of impact parameters
*   maxk:               labeling of l,m
*                           k=l*(l+1)/2 + m + 1
*   maxR:               maximum number of R sectors
*   maxt:               maximum number in t mesh and R mesh as well
*   fact(n):            factorial n!
*   bmesh:              impact parameter mesh
*   Rmesh:              internuclear separation mesh
*   tmesh0:             time mesh for interpolation
*   tmesh1:             time mesh
*                             tmesh1(Nnegtv+i+1)=-tmesh1(Nnegtv-i+1)
*   Rsection:           sector in R
*   vtstepR:            the v*t step size within each R sector
*   v:                  velocity of projectile
*   vtmin:              the starting v*t
*   vtmax:              the ending v*t
*   vtmid:              the ending v*t for two-center matrix elements
*   Nchannel:           total number of basis functions on both centers
*   NR:                 number of R sectors
*   NNR:                not used
*   Nb:                 number of b mesh
*   Nt0:                # of positive or negative t mesh for interpolation
*   NNt:                total number of time mesh
*   Nnegtv:             number of time mesh at negative time
*   Npostv:             number of time mesh at positive time
*   Norder:             number of points in cubic spline interpolation
*
```

```
*   ngaussx:            number of points in Gauss-Legendre quadrature
*   xgauss:             abscissas in Gauss-Legendre quadrature
*   xweight:            weight in Gauss-Legendre quadrature
*
*   cm:                 normalization factor of phi-part wavefunction
*   Pnorm:              normalization factor of Plm, normalized to unity
*   npowerA,npowerB:    the power of r in the Slater orbitals
*   expontA,expontB:    the exponential of the Slater orbitals
*   lAorbtl,lBorbtl:    angular momentum of the Slater orbitals, individual
*   mAorbtl,mBorbtl:    magnetic quantum number of the Slater orbitals
*   nAorbtl,nBorbtl:    sub-sequence number of orbital within an l,m pair
*   anormlA,anormlB:    normalization factor of each radial orbital
*   lAchannl,lBchannl: angular momentum of the Slater orbitals, grouped
*   numbAchl,numbBchl: number of radial orbitals within a fixed l
*   numbAsts,numbBsts: number of states within a fixed l
*   energyA,energyB:    energy of the state
*   stateA,stateB:      the coeficient of atomic states
*   lAstate,lBstate:    the l quantum number of each state
*   mAstate,mBstate:    the m quantum number of each state
*   indexA,indexB:      index number of an orbital
*   jndexA,jndexB:      index number of a state
*   idxmaxA,idxmaxB:    number of orbitals in all on each center
*   jdxmaxA,jdxmaxB:    number of states in all on each center
*   lAmax,lBmax:        number of angular momenta in orbitals
*   lmaxAB:             the largest angular momentum used
*
*   za0,za1,za2,za3:    parameters for model potential on center A
*   zb0,zb1,zb2,zb3:    parameters for model potential on center B
*
*   lmcheck:            constant to guarantee        m <= l
*   Eaastore,Ebbstore: stored E functions
*   GmatrixAA:          Hamiltonian matrix
*   GmatrixAB:          Hamiltonian matrix
```

```
*   GmatrixBA:          Hamiltonian matrix
*   GmatrixBB:          Hamiltonian matrix
*   SmatrixAB:          overlap matrix
*   SGmatrix:           the derivative matrix
```

C.2 Input

```
E(keV/amu)    vTmin      vTmax     vTmid < max(vTmax, |vTmin|)
  25         -100        150        60
Initial # of states on center A
0
n    l     m      amplitude
Initial # of states on center B
1
n    l     m      amplitude
1    0     0      (1.0,0.0)
Legendre File (format:path/file) ../data/Legendre.dat
# Legendre Points  (6-20, 24, 28, 32, 36, 40, 44, 48, 80, ..., 200)
10
# R sections
10
R sectors
0     0.5    2     4     8    40    70    100   300   2000
step size
0.01  0.05  0.1   0.2   0.4   1.0   3.0   5.0   10.0   20.0
# impact parameters
3
b
1.0  2.5  4.0
Option flags (1=on)
#1  #2  #3  #4  #5  #6  #7  #8  #9  #10 #11
1   0   0   0   0   0   1   1   0    0   0
```

```
 (1) Print Eigenfunction          (7)  Calculate Cross Section
 (2) Print GAA and GBB            (8)  Flush buffer frequently
 (3) Print SAB, GAB and GBA       (9)  Odd states
 (4) Print MatrixElement          (10) Energies only
 (5) Print DerivativeMatrix       (11) Check parameters only
 (6) Unitary Check

Orbitals  [-Z0 + (Z1 + Z2*r) exp(-Z3*r)]/r
    Potential on center A (Li)    Z0     Z1     Z2      Z3
                                   1     -2    -2.92    2.92
    Potential on center B (He)    Z0     Z1     Z2      Z3
                                   1     -1   -0.65354  2.69697
    The maximum number of l on center       A and B
                                             3     3
      Center A              l        #     s
                            0        5
         n first            n last
         1                  2
         alfa      beta
         0.025     1.342
      Center A              l        #     p
                            1        4
         n first            n last
         2                  3
         alfa      beta
         0.080     1.610
      Center A              l        #     d
                            2        1
         n first            n last
         3                  3
         alfa      beta
         0.200     1.665
      Center B              l        #     s
```

```
                        0        5
   n first              n last
   1                    4
   alfa      beta
   0.090     1.910
Center B                l        #     p
                        1        4
   n first              n last
   2                    4
   alfa      beta
   0.150     1.910
Center B                l        #     d
                        2        2
   n first              n last
   3                    4
   alfa      beta
   0.200     1.666
```

.

C.3 Output

Below shows a very simplified output from the TCAOCC code. There are 4 numeric columns per atomic state column. The very first column lists the impact parameters, the second column lists the real part of the amplitudes and the third column lists their imaginary part. The last column lists the probabilities. The figure in the bracket (....) is the cross section. The 1s0(A) indicates the atomic state in center A and has a binding energy of –0.20176 a.u. From the output, immediately following the first atomic state column, there are another two identical adjacent columns but with different atomic state indicators. Using this order, one can easily identify the electron transition processes to any *nlm* states. Since this code is a two-center code, the output of center B is right after center A.

```
Amplitudes and Probabilities
```

```
        No of states on this center:  9
 b      #  1
        1s0(A)    -0.20176

 1.000    0.082713  0.154788   0.03080
 2.500    0.031782 -0.088853   0.00890
 4.000   -0.014169 -0.016215   0.00046
                          (   0.82304)
```

C.4 Differential cross section (dcs.f) and input parameters

The dcs.f code is used to calculate the differential cross section as a function of scattering angles θ. Here we shall give the explanations of the input parameters required to execute the dcs.f code.

```
* zA,zB:          Charges on center A and B
* amassA,amassB: Masses on center A and B in Atomic Weight Unit
* Z0:             The maximum distant of z=vt
* v:              Velocity of the projectile in a.u.
* iprocess:       For excitation:= 0; for Capture:= 1
* Ntheta:         #. of points in scattering-angle theta grid
* delthata:       Step-size of the scattering-angle theta grid
* norder:         Order of interpolation (NEED NOT CHANGE)
* Nbin:           #. of points in impact parameter from TCAOCC
* Nbmesh:         #. of points in impact parameter for interpolation
* mf:             Order of Bessel function J_mf(x)
```

Sample of the input file: dcs.inp

```
 1.  1.  23.  87.   zA,zB,amassA,amassB (Na+ Rb: B: proj. A:targ)
 250. 0.110  1      Z0,v,iprocess(=0: excit; =1: capture)
 40   5d-5  4 5 10  Ntheta,deltheta,norder,Nbin, Nbmesh
 0                  mf
 0.05     0.304114        0.050016        0.09499
```

```
0.1      -0.000990       -0.200970        0.04039
0.15     -0.067664        0.224409        0.05494
0.2       0.245309        0.206718        0.10291
0.25      0.336630       -0.255538        0.17862
```

Above shows the input of the dcs.f. After the 4th row, there are 4 columns. The 1st one lists the impact parameters from TCAOCC. The second column lists the real and the imaginary parts of the transition amplitudes and the last column lists their corresponding probabilities. Note that the last column is not used in the calculation but merely for checking purposes. The output is self-explanatory and therefore we shall not reiterate for this manner.

Appendix D

HSCC Program

All the key equations of the hyperspherical close-coupling (HSCC) formalism are presented in Chapter 4. Here we shall only provide the know-how of using the HSCC package. This package has been divided into 6 subprograms and can be obtained from the author or Prof. C. D. Lin. However, before executing each program, it is important to know how to prepare the input parameters for each code. The following are the necessary steps to use the HSCC codes.

D.1 Code-names and explanation of input variables

1. mydvr.f :– This code generates the DVR radial-mesh and the input (mydvr.inp) is shown below. The output is written into a file called RGrid.dat. In this input, we only vary NSECT, NEACH and RSECT.

   - NSECT: Number of sectors
   - NEACH: Number of points in each sector
   - RSECT: Step-size of each sector.

```
&INPUT
 NCNFG=4,
 NDVR=200,
 KEYIR=1,
```

```
 NSECT=9,NEACH=23,
 RSECT = 0.0 5.0 10.0 15.0 20.0 25.0 30.0 35.0 40.0
 KEYOVLP=1,
 KEYSDN=0,
&END
```

2. AdiPot.f :– Adiabatic code to generate potential curves + matrix elements need for scattering codes. Need to change the directories of the write out in the source code. e.g.,/tmp/ltg/..... The parameters in the input file AdiPot.inp are self explanatory and therefore we shall not repeat here.

3. myinterR.f :– Interpolate the eigen-energies and matrix elements parameters needed to change in myinterR.f are

   (a) NSECTORP:= Number of the "actual" required sectors for calculation.

   (b) ix := Number of sub-sector in each sector when there is no interpolation.

   (c) Directories for read in and write out.

   (d) ChannelsInc:= Number of desired channels. Note that the myinterR.inp is the same as AdiPot.inp except that ChannelsInc is varied for the desired number of channels to be included in the calculation.

   (e) Require the data of rint.dat for the interpolation. rint.dat contains the "actual" radial-mesh points in which we want to interpolate and these points are generated from mydvr.f.

   $*$This code automatically reads rint.dat, rint.dat contains the R-mesh which we want to interpolate. The interpolate points must be smaller or = to the radial points in AdiPot.inp.

4. mystg2.f :– Radial Equation Solver. The number of channels in mystg2.inp must be the same as in myinterR.inp. Check destinations of the input and output files. Below shows the input file called mystg2.inp

```
NCH is number of channels Don't change KEYamp
 &INPUT
  NCH=5,
 &END
```

5. mystg3.f :– R-Matrix Propagator $***$ CHECK the destinations of the input and output files. This code reads in the mystg3.inp which contains

```
Note: energy not multiplied by mu
Don't change KEYFR
NMP: integration mesh point over the matching
surface, FOR 2D MATCHING (?)
Rcur: matching radius
NADIA: NO. OF CHANNELS
EMIN: total min. energy in atomic unit
NE: number of energy points
&INPUT
  NADIA=5,
  Rcur=30.d0,
  amu=1466.9795d0,
  EMIN=21.5495854d0,EMAX=100.0d0, NE=0
  NS=8,
  KEYFR=1,
&END
```

   The parameters needing to change are

   (a) NADIA = Number of ChannelsInc :- No. of Channels include in calculation.

   (b) Rcur = matching radius

   (c) amu = reduced mass

   (d) EMIN and EMAX = Total energy = (k.e + threshold) e.g.: (0.1-0.4998...) a.u. = -0.3998....

6. myKmat.f :– 1D matching and calculate cross section for each partial waves. Need to Change myKmat.inp

Additional programs required to calculate all partial waves cross sections are

- Jall.bat :– batch run steps (3) to (5). Do all J-dependent cross sections.

- XsecJall.bat:- Collect all the J-dependent cross sections and put into file called 'cs.dat'
- SumCapXsec.f:– Sum all the J-dependent cross sections to get the final total cross section.